



Comparison of nonlinear frequency division multiplexing and OFDM for optical fiber transmissions

Wasyhun Asefa Gemechu

► To cite this version:

Wasyhun Asefa Gemechu. Comparison of nonlinear frequency division multiplexing and OFDM for optical fiber transmissions. Networking and Internet Architecture [cs.NI]. Université Paris Saclay (COMUE); Università degli studi (Brescia, Italie), 2019. English. <NNT : 2019SACLT021>. <tel-02263831>

HAL Id: tel-02263831

<https://pastel.hal.science/tel-02263831v1>

Submitted on 5 Aug 2019

HAL is a multi-disciplinary open access archive for the deposit and dissemination of scientific research documents, whether they are published or not. The documents may come from teaching and research institutions in France or abroad, or from public or private research centers.

L'archive ouverte pluridisciplinaire **HAL**, est destinée au dépôt et à la diffusion de documents scientifiques de niveau recherche, publiés ou non, émanant des établissements d'enseignement et de recherche français ou étrangers, des laboratoires publics ou privés.



HAL Authorization

Comparison of Nonlinear Frequency Division Multiplexing and OFDM for optical fiber transmissions

Cotutelle de thèse de doctorat de l'Université Paris-Saclay
préparée à Télécom ParisTech (France)

et

Università degli Studi di Brescia (Italie)

École doctorale n°580 sciences et technologies de l'information et de
la communication (STIC)

Spécialité de doctorat: Communications et Electronique (France)

École doctorale n°05 sistemi di elaborazione delle informazioni
Spécialité de doctorat: Ingegneria dell'Informazione (Italie)

Thèse présentée et soutenue à Brescia (Italie), le 1 avril 2019, par

Wasyhun Asefa Gemechu

Composition du Jury :

Antonio MECOZZI	Président
Professeur, Università degli Studi dell'Aquila	
Christophe PEUCHERET	Rapporteur
Professeur, ENSSAT – Université de Rennes I	
Marco SECONDINI	Rapporteur
Associate Professeur, Scuola Superiore SANT'ANNA	
Sergei TURITSYN	Examineur
Professeur, Aston University	
Yann FRIGNAC	Examineur
Professeur, Telecom Sud Paris	
Fabrizio FREZZA	Examineur
Professeur, Università degli Studi di Roma, La Sapienza	
Stefan WABNITZ	Directeur de thèse
Professeur, Università degli Studi di Brescia	
Yves JAOUEN	Directeur de thèse
Professeur, Telecom ParisTech	
Costantino DE ANGELIS	Co-Directeur de thèse
Professeur, Università degli Studi di Brescia	
Mansoor YOUSEFI	Co-Directeur de thèse
Professeur associé, Telecom ParisTech	
Erwan PINCEMIN	Invité
ingénieur de recherche, Orange Labs	



Acknowledgments

This research project would not have been possible without the support of many people. First of all, I express my deep gratitude to my supervisor, Prof. Stefan Wabnitz, for many things. To name a few, for giving me the opportunity to pursue this Ph.D. with a very exciting topic, for encouraging me with his positive feedback all the time, for dragging me forward slowly but surely from bottom to world of curiosity, and for sharing his immense knowledge, experiences and awesome stories. When I became stuck in my research, discussion with him or the summer school programs he allowed me to participate has opened new horizons to my understanding of nonlinear optics. He is a very kind and sympathetic supervisor who has understanding of my personal shortcomings as well. It is said that good people are those who help others when asked, and the best of the people are those who help before being asked. Professor Stefan Wabnitz (the chairman) definitely falls into the latter categories. I cannot imagine being blessed to have him as mentor and guiding northern star.

Next, I would like to give my sincere thanks to Prof. Yves Jaouën, with whom I had the best opportunity to work and learn during the half of my Ph.D. He is an outstanding expert in experimental areas and discussion with him always makes you stay in the laboratory trying everything. For example, he taught me how to carefully setup optical experiments, and help me to optimize numerical methods in optical communication systems. Moreover, his close inspection of experimental results, assistance in administrative procedures and very open friendly personality with great sense of humor makes him one of the great people.

I thank also Dr. Mengdi Song for teaching me the DSP of OFDM communication system and everything I know about the optical communication experimental setups. Coming from zero-experimental background, I had taken extended time, energy and knowledge from her which I am very grateful for it. Besides these, she is a very kind supervisor and amazing friend.

I would like to thank Prof. Costantino De Angelis for his great support

during the research period and for being my beloved professor during my stay in university of Brescia. He is a kind of scientist makes everything fun and easy while presenting them and personally I admire him for his friendly approach and sense of humor. I want also to thank my co-authors for fruitful discussion, Nicolas Brochier and Erwan Pincemin of Orange Labs for letting me borrow the TW-SRS fiber, and all the Ph.D jurors and reviewers for their time and participation. Moreover, I thanks Prof. Jose Alvarez-Chavez, Prof. Daniele Modotto, Dr. Katarzyna krupa, Dr. Tobias Hans Evert, and Dr. Martino Bernard for their insight and discussion on nonlinear optics.

Finally I would like to thank all my amazing "pomodoro" friends, Dr. Justine Saint-Aubert, Dr. Alix Pérusseau-Lambert, Ing. Bastien Duong, Dr. Edison Gerena, Ing. Bekir Öztürk, Ing. Merve Yurtsever, Ing. Ygal Caen, Ing. Ilona Gatto, Dr. Wei Wei, Dr. Heming Huang, Dr. Jianan Duan and my family, for making my life amazing, for being there in every step of journey and for making history together.

Contents

List of Symbols	17
1 State of the Art of Optical Communication Systems	27
1.1 Fiber optic networks	28
1.1.1 Traffic evolution of optical networks	29
1.2 The Optical Fiber Channel	30
1.3 Fiber impairments	32
1.3.1 Fiber loss	33
1.3.2 Chromatic dispersion	34
1.3.3 Polarization mode dispersion	36
1.3.4 Kerr nonlinearity	36
1.3.5 Optical amplification and noise	39
1.4 Scalar nonlinear Schrödinger equation	42
1.5 Coupled nonlinear Schrödinger equation	44
1.6 Capacity of optical fiber channels	45
1.6.1 Fiber capacity increment	46
1.6.2 The nonlinear Shannon limit	48
1.7 Fiber nonlinearity mitigation	49
1.7.1 Digital back-propagation	50
1.7.2 VSTF based nonlinear equalizer	51
1.8 Summary	53
2 Optical Transmission Systems based on the Nonlinear Fourier Transform	55
2.1 Introduction	55
2.2 Principle of the nonlinear Fourier transform	57
2.3 Theory of the nonlinear Fourier transform	59
2.4 Numerical method for computing the NFT	64
2.4.1 Numerical Forward NFT using the AL-discretization method	65
2.4.2 Numerical Inverse NFT using the LP method	66

2.5	Nonlinear Frequency Division Multiplexed Systems	73
2.6	NFT of polarization division multiplexed signal	76
2.7	Summary	79
3	Experimental demonstration of a NFDM based optical transmission system	81
3.1	Introduction	81
3.2	Brief review of the coherent optical OFDM transmissions . . .	84
3.3	Experimental generation, transmission and detection of NFDM signal	85
3.3.1	NFDM signal generation	85
3.3.2	Optical modulator	86
3.3.3	Amplified Optical fiber transmission link	88
3.3.4	Coherent receiver	88
3.3.5	NFDM signal detection	90
3.4	NFDM digital transmitter design	90
3.4.1	Modulation and symbol mapping	90
3.4.2	Baseband signal generation	91
3.4.3	Guard interval insertion	91
3.4.4	Forward mapping	92
3.4.5	Signal denormalization	93
3.5	NFDM digital receiver design	94
3.5.1	Time synchronization	94
3.5.2	Carrier frequency offset compensation	95
3.5.3	Signal normalization	96
3.5.4	NFT computation and channel inversion	96
3.5.5	Spectral demapping and guard interval removal	97
3.5.6	Residual channel equalization	97
3.5.7	Laser phase noise compensation	98
3.5.8	Data decoding and performance measurement	99
3.6	Experimental Validation	100
3.6.1	Experimental demonstration of a single-polarization NFDM transmission	101
3.6.2	Experimental demonstration of a dual-polarization NFDM transmission	106
3.6.3	NFDM comparison in the normal and anomalous dispersion regime	112
3.7	Conclusions	114

4	Practical challenges in NFDM implementation	117
4.1	Simulation setup	118
4.1.1	Physical constraints	121
4.1.2	NFDM signal dimensioning	121
4.2	Intrinsic physical challenges	122
4.2.1	Noisy channel	122
4.2.2	Gaussian pulse propagation in a noisy fiber channel	123
4.2.3	Transmission of a 16QAM NFDM signal	124
4.2.4	Lossy channel	129
4.3	Optical challenges	132
4.3.1	Frequency Offset and Laser Phase Noise	132
4.3.2	Transmission analysis of laser phase noise penalty	132
4.4	DSP implementation and transmission device issues	135
4.4.1	Guard interval and spectral efficiency	135
4.4.2	Oversampling and numerical accuracy	138
4.5	Transmitter and receiver limitations	139
4.5.1	TX and RX limitation in B2B performance	142
4.5.2	TX and RX limitation in transmission performance	142
4.6	Summary	144
5	Conclusions and Future Work	147
5.1	Conclusion	147
5.2	Future Work	149
5.3	INTRODUCTION	164
5.4	PRINCIPE DUNE TRANSMISSION NFT	165
5.5	TRANSMISSION DUN SIGNAL NFDM MULTI- PLEXE EN POLARISATION	165

Contents

List of Figures

1	Evolution of commercial optical transmission system since mid 1980s and forcast for coming 20 years (after [45])	21
1.1	Optical network hierarchy; Long-haul core network, metro/regional and "last-mile" access network.	28
1.2	Global IP data traffic forecast, in number of exabytes per month for the period of 2016-2021, as reported in the Cisco Visual Networking Index [32].	30
1.3	(a) Data centers global IP traffic growth. (b) projected data traffic distribution by destination in 2021. Source: Cisco Global Cloud Index, 2016-2021 [32].	30
1.4	Illustration of an electric field distribution or mode solution of a single mode fibers along the cross-section.	32
1.5	Attenuation curve of conventional G-652 fibers.	34
1.6	Dispersion curves of various single-mode fibers [37].	35
1.7	Schematic representation of lumped amplification using EDFAs.	40
1.8	Illustration of pulse broadening effect due to GVD (a), and (b) SPM-induced spectral broadening of a Gaussian pulse. . .	43
1.9	Physical available degree-of-freedom for modulation and multiplexing of optical signal [45].	47
1.10	Estimated of achievable data-rates versus input power of a nonlinear fiber channel [47].	49
1.11	Illustration of forward propagation in real fiber governed by NLSE and digital backward propagation (DBP) through virtual fiber using the inverse NLSE.	51
1.12	(a)Block diagram of IVSTF-NLEs equalizer; and (b) Q-factor vs. input power performance improvement obtained for 400 Gb/s without/with IVSTF-NLEs and DBP-SSFM _{1,2,8,64} in SSMF (after [59]).	52

List of Figures

2.1	Schematic representation of solving the IVP of PDEs in (a), direct and inverse Fourier transform;(b), direct and inverse NFT.	59
2.2	nonlinear spectrum of a potential function with vanishing boundary condition.	61
2.3	Scattering problem associated with the continuous spectrum.	62
2.4	Illustration of the NFT of a simple un-modulated rectangular pulse. The absolute value of the continuous spectrum of a rectangular pulse $q(t) = A * rect(t)$, (a), evolves from a simple sinc-type for (b) $A=1$, to more complicated shapes for (c) $A=4$, and (d) $A=6$	67
2.5	DBP of NFT	69
2.6	The numerical accuracy of the NFT-INFT algorithm as function of the number of samples for a different signal types.	70
2.7	Flow chart of NFT algorithm implementation (after [75]).	71
2.8	Flow chart of INFT algorithm implementation (after [75]).	72
2.9	lin of NFT	74
2.10	The architecture of NFDM transmission system (a) and (b) the corresponding DSP.	75
2.11	The numerical accuracy of a dual-polarization NFT-INFT pair for a dual polarization signal which given by a shifted Gaussian shaped initial spectrum $\hat{\mathbf{q}} = [\hat{q}_x, \hat{q}_y]$ and $NFT(INFT(\hat{\mathbf{q}}))$ at high power. For a fixed sample size, the accuracy of algorithm decreases at large amplitudes (after [83]).	78
3.1	Illustration of NFDM optical transmissions. (a) A Q-factor as function of the launch power when modulating the continuous spectrum [105]; (b) BER performance as a function of OSNR for discrete spectrum modulation in a dual-polarization configuration [84].	83
3.2	Principle of OFDM and its spectrum. (a) Theoretical overlapping and orthogonal subcarriers, (b) experimental Nyquist bandwidth of OFDM.	85
3.3	The experimental setup block diagram and the associated offline DSP chain at the TX and RX.	86
3.4	Structure of (a) a Mach-Zehnder-Modulator (MZM), (b) an IQ-modulator made of two MZMs and a $\pi/2$ phase shifter.	88
3.5	Polarization diversity intradyne receiver.	89
3.6	Signal broadening due to dispersion in NFDM transmission over 1600 km fiber link.	92
3.7	Comparison of NFDM signal with different input power levels.	94

3.8	2D symbol matrix structure of NFDM/OFDM in frequency (subcarriers) and time (symbol).	102
3.9	A typical sample of (a) NFDM, and (b) OFDM temporal domain waveforms.	103
3.10	Pre-distortion of the NFDM signal (b) in order to compensate for non-uniform amplitude response of transmitter (a).	103
3.11	The received spectra of OFDM and NFDM after post-correction (a-b). Compared to NFDM, the OFDM spectrum shows significant distortions from four wave mixing (FWM).	105
3.12	Q-factors as a function of burst power for single polarization NFDM and OFDM transmissions.	105
3.13	A relative error between the input and output in the non-linear spectral amplitude $\widehat{q}(\lambda, \cdot)$ in (a) simulation, and (b) experiment for 16GHz NFDM transmissions.	106
3.14	The Received constellations at $P = -3$ dBm for 16GHz (a) NFDM and (b) OFDM.	106
3.15	Data structure of real part of 16QAM PDM-NFDM/OFDM.	107
3.16	Experimental setup, PDM-NFDM data stream structure and offline Tx/Rx DSP	108
3.17	Examples of PDM-NFDM time domain symbols.	110
3.18	Received constellations at $P = -3$ dBm for PDM-NFDM after a transmission and in a back-to-back configuration.	110
3.19	NFDM and OFDM results in SP- and PDM-NFDM.	111
3.20	Q penalty induced by DGD.	112
3.21	The PDM-NFDM experiment in the normal and anomalous dispersion regime using either the TW-SRS or the SSMF fiber, respectively.	113
4.1	Simulation setup.	119
4.2	The numerical study schematic diagram of an noiseless and noisy evolution of the continuous spectrum over fiber channel.	123
4.3	The ideal and noise loaded nonlinear spectrum of a Gaussian input with launch power $P_0 = -8, -5, \& -2$ dBm. The amount of noise in the nonlinear spectral domain is proportional to the initial spectral amplitude.	124
4.4	NMSE between different nonlinear spectral amplitude $\widehat{q}(\lambda)$ with an input power of $P_0 = -8, -5, \& -2$ dB as a function of the OSNR with $B_{opt}=0.1$ nm.	125

4.5	Illustration of the NFDM transmission performance in a noisy and noise free transmissions. The input and output continuous spectral amplitude $\widehat{q}(\cdot, \lambda)$ is shown here in the case of: (a) a noise free, and (b) a noisy optical link,	126
4.6	Constellation of NFDM transmission (a) without ASE noise, (b) with ASE noise.	126
4.7	Q-factor performance as a function of input launch power for NFDM transmission system with and without ASE noise. . .	128
4.8	Numerical simulation model of a periodically amplified lossy channel and an ideal lossless channel.	130
4.9	The NFT continuous spectrum of a lossless and lossy transmission where the later approximated by the LPA method. .	131
4.10	Q-factor performance vs an input power for a lossless and a lossy noise-free fiber transmission over 1680km.	131
4.11	Q-factor performance of NFDM transmission over $L = 840$ km and $L = 1680$ km using laser line width of $\Delta\nu = 100$ kHz and $\Delta\nu = 0$ kHz.	133
4.12	A B2B Q-factor penalties as functions of a laser linewidth for a burst launch input power of 1, -1 and -3 dBm over a 1680 km link.	134
4.13	Q-factor performance versus transmission distance (no ASE noise is considered).	135
4.14	Simulation result of a B2B Q-factor performance as a function of NGI for NFDM transmissions with input power of -4 dBm and -1 dBm.	137
4.15	Q-factor vs burst input power for NFDM transmissions with different NGIs in a noise-free (solid lines) and noisy (dashed lines) fiber transmissions.	137
4.16	Illustration of B2B performance of the oversampling factor. .	139
4.17	Q-factor performance as function of input launch power for the oversampling factor of 4 and 8.	139
4.18	Experimentally measured DAC frequency/Phase response for the (a) I- and (b) Q-channels.	140
4.19	Signal spectra of the NFDM signal, (a) before and (b) after the amplitude pre-emphasis equalizer compensating for the transmitter electronics induced amplitude distortion.	141
4.20	ENoB vs OSNR	142
4.21	Q-factor performance as a function of the burst input power after 1680km. The DAC resolutions are 3,5,6 and 7 bits, ASE noise was added.	143

5.1	Comparaison d'une transmission NFDM et linéaire.	166
5.2	Dispositif expérimental. Insert: structure de la trame NFDM/OFDM multiplexée en polarisation, Etapes du traite- ment signal Tx/Rx (en blanc: OFDM, couleur: étapes spéci- fiques NFDM)	167
5.3	Performances obtenues: (a) résultats NFDML et OFDM en mono- et double polarisation, (b) Constellation s NFDM à -3dBm, (c) Sensibilité à la DGD.	167

List of Figures

List of Tables

1.1	Optical network hierarchy by transmission reach.	29
1.2	Different optical communication wavelength bands.	40
1.3	Typical parameters of different fiber types at $\lambda = 1.55 \mu\text{m}$. . .	44
2.1	Parameters in NFT/INFT algorithms.	72
3.1	Experimental demonstration of a continuous and discrete spectrum based optical NFDM transmission systems.(* Dual- polarization NFDM transmission systems.)	82
4.1	NFDM parameters.	120
4.2	TW-SRS parameters.	121
4.3	System parameters.	121

*

List of Acronyms

ADC	analog-to-digital converter
ASE	amplified spontaneous emission
AKNS	Ablowitz-Kaup-Newell-Segur
AOM	acousto-optical modulator
AWG	arbitrary waveform generator
AWGN	additive white Gaussian noise
B2B	back-to-back
BER	bit error rate
CD	chromatic dispersion
CNLSE	coupled nonlinear Schrödinger equation
CO-OFDM	..	coherent optical orthogonal frequency division multiplexing
DAC	digital-to-analog converter
DBP	digital back-propagation
DCF	dispersion compensation fiber
DGD	differential group delay
DP-NFDM	..	dual-polarization nonlinear frequency division multiplexing
DPO	digital phosphor oscilloscope
DSP	digital signal processing
DST	direct scattering transform
ECL	external cavity laser
EDC	electrical dispersion compensation
EDFA	erbium-doped fiber amplifier
ENoB	effective number of bits
EVM	error vector magnitude
FFT	fast Fourier transform
FWHM	full-width half-maximum
FWM	four-wave mixing
GLM	Gelfand-Levitan-Marchenko
GVD	group velocity dispersion

I	in-phase
ICI	inter-carrier interference
IFFT	inverse fast Fourier transform
IM/DD	intensity modulation/direction detection
INFT	inverse nonlinear Fourier transform
IP	Internet Protocol
ISI	inter-symbol interference
IST	inverse scattering transform
IVP	initial value problem
LO	local oscillator
LPA	lossless path-averaged
MIMO	multiple-input multiple-output
MS	Manakov system
MZM	Mach-Zehnder modulator
MZSP	Manakov-Zakharov-Shabat spectral problem
NFDM	nonlinear frequency division multiplexing
NFT	nonlinear Fourier transform
NIS	nonlinear inverse synthesis
NLSE	nonlinear Schrödinger equation
NMSE	normalized mean squared error
NZDSF	non-zero dispersion-shifted fiber
OBPF	optical band pass filter
OFDM	orthogonal frequency-division multiplexing
OPC	optical phase conjugation
OSNR	optical signal-to-noise ratio
PAPR	peak-to-average power ratio
PBS	polarization beam splitter
PC	polarization controller
PDE	partial differential equation
PDL	polarization-dependent loss
PMD	polarization mode dispersion

List of Acronyms

PRBS	pseudo-random bit sequence
P/S	parallel-to-serial
Q	quadrature
QAM	quadrature amplitude modulation
QPSK	quadrature phase-shift keying
RH	Riemann Hilbert
SE	spectral efficiency
SDM	space-division multiplexing
SMF	single-mode fiber
SNR	signal-to-noise ratio
S/P	serial-to-parallel
SPM	self-phase modulation
SP-NFDM	...	single polarization nonlinear frequency division multiplexing
SSFM	split-step Fourier method
VSNE	Volterra series nonlinear equalizer
WDM	wavelength-division multiplexing
XPM	cross-phase modulation
ZSP	Zakharov-Shabat spectral problem

Symbols

Vectors and matrices are denoted by bold letters (e.g., \mathbf{A}), whereas scalars are denoted by italic letters (e.g., A). The real and imaginary parts of a complex variable A are denoted as $\Re(A)$ and $\Im(A)$, respectively. The set of real and complex numbers are denoted by \mathbb{R} and \mathbb{C} , respectively.

List of Symbols

$a(\lambda)$	nonlinear scattering coefficient
$A(z, t)$	complex field envelope in time domain
A_{eff}	effective core area
$A_{x/y}$	optical field triplet in the x/y polarizations
$\mathbf{A} = [A_x, A_y]$	Jones vector
$b(\lambda)$	nonlinear scattering coefficient
B	bandwidth
D	dispersion parameter
D_p	PMD parameter
\hat{D}	NLSE linear operator
E	electrical field vector
f_s	sampling frequency
$\mathcal{F}\{\cdot\}$	Fourier transform operator
$\mathcal{F}^{-1}\{\cdot\}$	inverse Fourier transform operator
G	optical amplifier gain
$I_{x/y}$	in-phase signal component in the x/y polarization
L	fiber length
\mathbf{L}	Lax operator
L_D	dispersion length
L_{eff}	effective length
L_{NL}	nonlinear length
L_s	fiber span length
\mathbf{M}	Lax space-evolution matrix
N_s	number of fiber spans
\hat{N}	NLSE nonlinear operator
\mathbf{P}	Lax time-evolution matrix
P_0	input peak optical power
P_{ASE}	ASE noise power
$q(\tau, z)$	normalized complex envelope of the electric field
$\hat{q}(\lambda)$	continuous spectrum amplitude
$\tilde{q}(\lambda)$	discrete spectrum amplitude

List of Symbols

$Q(\omega)$	FT of complex field value
R_b	bit-rate
R_s	symbol-rate
t	continuous time (retarded time-frame)
T_s	symbol period
T_0	normalization period
v	solution of the ZSP
v_g	group velocity
V_π	Mach-Zehnder modulator half-wave voltage
z	normalized space coordinate
α	attenuation coefficient
β_2	group velocity dispersion coefficient
γ	nonlinear coefficient
Δf	frequency spacing
τ	normalized time
λ	wavelength
λ_0	central wavelength
ϕ_{NL}	nonlinear phase rotation
ω	baseband angular frequency
$\lambda \in \mathbb{R}$	nonlinear frequency
$\lambda_i \in \mathbb{C}^+$	discrete eigenvalues

General Introduction

IN today's world, reliable and high-speed transmission of information over long reach is vital. Optical fibers play a significant role in information transmissions and will continue to take the center stage in the foreseeable future [1]. The earliest attempts at optical communication date back to 1792, when French scientist Claude Chappe came up with the idea of the optical telegraph and developed a coding scheme to encode information alphabets [3]. In the 1840s, two physicists, Jean-Daniel Collodon from Switzerland and Jacques Babinet from France demonstrated that light could be directed along water jets for night-time fountain displays. Over the next 20 years, physicists and engineers put more effort to transmit light in bent glass rods and enhance the capacity of electrical telecommunication systems.

The first breakthrough came with the invention of the laser and its demonstration in 1960 by Maiman [4], which allowed to generate coherent light beams. Even though optical fibers were available during the 1960s, they were used for medical imaging rather than for optical communications [13]. Initially, the fiber attenuation introduced by Kao and Hockham in 1966 was extremely high (1000 dB/km) [6], while the atmospheric loss was few dB/km. Fiber loss was diminished drastically to 20 dB/km by Corning Glass Works in 1970 [7]. Two years later, the same group produced a germanium core-doped fiber with a loss of only 4 dB/km, which further reduced to 0.2 dB/km at a wavelength near $1.55\text{ }\mu\text{m}$ by a T. Miya group from Japan [8]. The simultaneous availability of a low-loss fiber and compact Gallium Arsenide (GaAs) semiconductor laser, led to the first-generation optical transmission system using a graded-index multimode (MMF) fiber by AT&T at a bit rate of 54 Mbps near 850 nm band up to 23 km [9]. The transmission distance was mainly limited by modal dispersion in MMFs, and the distance between repeaters reached 10 km. In 1981, single mode fiber (SMF) was developed for long distance transmission, however, the fiber loss was not changed as the fundamental limit for loss is set by Rayleigh scattering. Due to the availability of SMFs and the InGaAsP semiconductor laser, the second-generation optical transmission system was deployed in the infrared region

near $1.3\ \mu\text{m}$ where the fiber loss was typically $0.5\ \text{dB/km}$. Transmission at a bit rate of $154\ \text{Mbps}$ over a repeater spacing of $\sim 50\ \text{km}$ was demonstrated in 1983 [10]. The first commercial opto-electronically regenerated wavelength-division multiplexing (WDM) system using two wavelength channels, each with $1.7\ \text{Gbps}$ bit rate, was introduced in 1989. The late 1980s also saw the deployment of the first transoceanic long-haul transmission fibers, across the Atlantic and Pacific ocean, carrying $280\ \text{Mbps}$ on each of three fiber pairs [11] – [12].

The third-generation optical transmission systems has migrated to $1.55\ \mu\text{m}$ where the fiber transmission loss is minimum, i.e. the attenuation value is $\leq 0.2\ \text{dB/km}$. However, their introduction was delayed by a relatively high dispersion value of SMF in this spectral region. In 1990, thanks to the combination of dispersion shifted fiber (DSF) with lasers oscillating in a single longitudinal mode, a transmission system operating at data rate of $2.5\ \text{Gbps}$ with signal regeneration distance of $\sim 70\ \text{km}$ became commercially available, and their bit-rate soon increased to $10\ \text{Gbps}$ to meet capacity demand [1], [13].

Until the early 1990s, direct detection was the state of the art, where information bits were transmitted by directly modulating the intensity of the laser source. The capacity increment was facilitated by improving the quality of the optical fiber and the transmitter-receiver electronics, while the repeater spacing was limited by the fiber loss. However, the invention of Erbium-doped fiber amplifier (EDFA), enabling periodic optical amplification for compensating fiber losses, has increased the repeater spacing to $\sim 100\ \text{km}$ and made the need for optical-electro-optical (OEO) conversion obsolete [1], [14], [15]. As bit-rate increased to $10\ \text{Gbps}$, group velocity dispersion (GVD) or chromatic dispersion (CD) become a challenge. To solve the dispersion issue, a dispersion shifted fiber (DSF) was introduced, which has negligible dispersion at $1.55\ \mu\text{m}$. Further mitigation of amplified spontaneous emission (ASE) using a forward error correction (FEC) codes, enabled the enhancement of optical signal-to-noise ratio (OSNR) for single-channel optical transmissions. Furthermore, EDFAs make it feasible to use a large portion of the available amplification bandwidth for a long-haul links, as they can simultaneously amplify different data streams modulated by lasers at a slightly different wavelength (WDM) to be transmitted over the same fiber [17] – [23]. Indeed, the combination of EDFA, WDM, an advance made in electronic and optoelectronic devices has enabled transmission systems carrying up to 80 channels with an individual bit rate of 10 to 40 Gbps on the 50-GHz grid over thousands of km. This represents an increase in system capacity by a factor of 400 and considered as the fourth generation lightwave

systems. The revival of coherent transmission techniques in combination with high-speed digital signal processing (DSP) matured in the early 2000s, also considered as the fifth generation lightwave systems, granted access to the amplitude, phase and the two orthogonal polarizations of the optical carrier, enabling the so-called higher spectral efficient modulation formats. Today, coherent polarization division multiplexed (PDM) transmission systems modulated with the quadrature amplitude modulation (QAM) format has achieved a net WDM data rates of more than 115 Tbps in a single-mode fiber [24] – [37] as illustrated in Fig.(1).

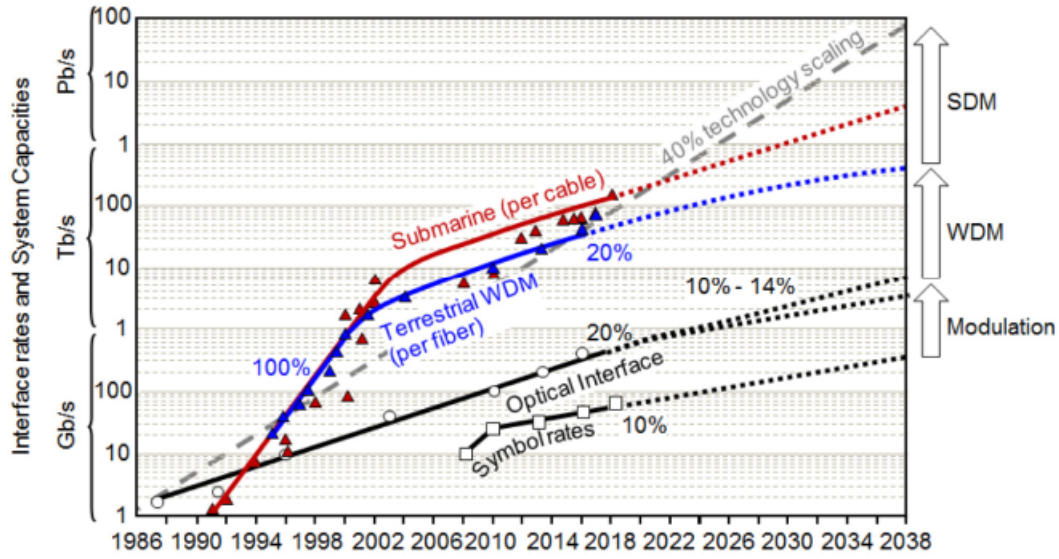


Figure 1: Evolution of commercial optical transmission system since mid 1980s and forecast for coming 20 years (after [45])

The technological advances made in lightwave technology over the last half-a-century (summarized in Fig.(1)), have led the optical channel capacity to skyrocket. As a result, an effort has been made in the early 2000s by scientist to estimate the ultimate capacity of single-mode fiber channels. In 1948 Claude E. Shannon introduced the concept of channel capacity, in which he showed that the SNR sets the ultimate achievable capacity of the a band-limited channel [27]. As opposed to linear channels, where the capacity can be increased by sending a more and more powerful signals, fiber optic channels suffers from nonlinear effects driven by the Kerr effect and inelastic scattering effects. The Kerr effect, which causes an optical power dependent variation of the refractive index, generates nonlinear signal distortions such as Self-Phase Modulation (SPM), Cross-Phase Modulation (XPM) and

Four-Wave Mixing (FWM) [1]. The interplay between these distortions and CD lead to progressive signal distortions that accumulate over the transmission link. These set a nonlinear propagation limit in the optical transmission systems, making it necessary to develop techniques for nonlinearity mitigation [28] – [29]. Several linear and nonlinear compensation techniques based on optical and digital methods have been proposed in order to increase the capacity of optical fiber links. However, digital compensation prevailed over their optical counterparts thanks to the combination of coherent detection with digital signal processing. However, the signal-noise nonlinear interaction set to the upper-bound of achievable performance gain by digital compensation methods.

Recently, eigenvalue communication has been considered as an emerging paradigm in fiber-optic communications, that could potentially overcome these limitations. This method, originally proposed by Hasegawa in 1993, is based on the fundamental observation that the discrete nonlinear spectrum of an optical signal is invariant (except for a trivial linear phase shift) upon propagation in the fiber channel, as described by the scalar NLSE. The method was never implemented since it was not suitable for the intensity-modulation and direct-detection (IM/DD) systems of the time. However, the recent development of practical coherent detectors based on fast digital signal processing enables the real-time measurement of both quadrature components of the received field. This means that the direct spectral transform (also known as nonlinear Fourier transform) of the received signal can be computed, and the eigenvalue spectrum fully recovered.

Motivation

Motivated by the eigenvalue communication in the coherent detection configuration, this thesis aims at the development of DSP methods for the implementation of nonlinear Fourier transform (NFT) and nonlinear frequency division multiplexing (NFDM), assisted by a comprehensive experimental validation in high-speed and long-haul coherent optical transmission systems. This thesis work is planned to accomplish the following main objectives

1. Develop a sufficiently accurate numerical implementation of NFT and inverse-NFT (INFT);
2. Quantify the numerical accuracy of INFT-NFT computational algorithm for different signal types;

3. Develop a full numerical model for the multi-carrier multiplexing technique based on NFT, also known as NFDM, both in single- and dual-polarization configuration;
4. Experimentally validate the developed techniques.

Thesis Outline

In order to accomplish the established research objectives, this thesis is organized into four chapters.

- **Chapter 1:** review the architecture and data traffic evolution of optical fiber networks, and the advent of the technology of coherent high-speed and long-haul optical transmission system. Afterward, SMF based transmissions and the associated channel impairments are described. To contextualize the nonlinear mitigation techniques in high-speed and long-haul transmission systems, this chapter provides a brief review of signal propagation in SMFs, exploring the scalar and vectorial nonlinear Schrödinger equation (NLSE) as the underlying signal propagation model, and introduces the nonlinear Shannon limit as setting a potential capacity crunch in the optical fibers. Finally, proposed solutions to increase channel capacity are reviewed.
- **Chapter 2:** provides the basic notions of the direct and inverse nonlinear Fourier transform (NFT/INFT) method and the associated eigenvalue communication systems. Next, the computation of the nonlinear spectrum of an ideal channel governed by the normalized NLSE, and its linear evolution in the nonlinear domain is presented. In addition, the numerical algorithms of implementation of the scattering transform and their accuracy are investigated briefly. Finally, a perturbation channel model that takes into account fiber losses and noise are discussed together with numerical validation of the effect this perturbation have on the ideal model of the channel.
- **Chapter 3:** addresses the experimental validation of high-speed long-haul coherent NFDM transmission systems, along with its linear counterpart, namely orthogonal frequency-division multiplexing (OFDM). The transmitter and receiver DSP design of NFDM is described, and compared against the traditional OFDM design, in terms of performance gain and complexity in an experiment for both single- and dual-polarization configurations, in both the focusing and the defocusing regime.

- **Chapter 4:** building upon the experimental observations, a numerical investigation is reported of challenges, faced when implementing long-haul transmission based on NFT such as noise, transmission loss, polarization mode dispersion (PMD), laser phase noise, oversampling, guard interval size, effective number of bits (ENOB), peak-to-average power (PAPR), etc.
- **Chapter 5:** summarizes, the main conclusions of the research and suggests research topics for future studies.

Main Contributions

This thesis proposes that the experimental validation should be preferentially conducted in the defocusing regime, where the discrete spectrum is absent and only the continuous nonlinear spectrum of the signal should be modulated. In this framework, user information streams are encoded onto parallel subcarriers (eigenvalues) that are analytically shown to be independent of each other upon a linear propagation in an ideal noise-free and lossless fiber channel. When compared with OFDM which is limited by fiber nonlinearity, NFDM will demonstrate a performance gain in terms of both Q-factor and optimal launch power. Furthermore, access to the polarization degree-of-freedom (DoF) will double the data. The main contribution of this thesis can be summarized as follows:

1. Describes the first experimental validation of a single-polarization long-haul NFDM transmission in the defocusing regime [C1].
2. Describes the first experimental demonstration of a dual-polarization NFDM transmission in defocusing regime[C2, J1].
3. Presents a study of challenges faced in the implementation of NFDM system which underlines the need for the search for better numerical algorithms to compute the spectral parameters, a transmitter (Tx) and receiver (Rx) DSP modules, new data encoding and multiplexing methods tailored to nonlinear fiber channels, and linear and nonlinear Tx-Rx distortion compensation methods.

List of Publications

The major achievements obtained from this thesis are published in the following list of peer-reviewed publications.

Papers in international journals

[J1] **Wasyhun A. Gemechu**, Tao Gui, Jan-Willem Goossens, Mengdi Song, Stefan Wabnitz, Hartmut Hafermann, Alan Pak Tao Lau, Mansoor I. Yousefi, and Yves Jaouën, "*Dual Polarization Nonlinear Frequency Division Multiplexing Transmission*", IEEE Photonics Technology Letters 30 (18), 1589-1592, July 2018.

Papers in conference proceedings

[C1] **Wasyhun A. Gemechu**, Mengdi Song, Stefan Wabnitz, Yves Jaouën and Mansoor I. Yousefi, "*Comparison of the Nonlinear Frequency Division Multiplexing and OFDM in Experiment*", paper W.3.C.4, ECOC (2017).
[C2] Tao Gui, **Wasyhun A. Gemechu**, Jan-Willem Goossens, Mengdi Song, Stefan Wabnitz, Mansoor I. Yousefi, Hartmut Hafermann, Alan Pak Tao Lau and Yves Jaouën, "*Polarization Division-Multiplexed Nonlinear Frequency Division Multiplexing*", paper STu4C.3, CLEO (invited), 2018.

Chapter 1

State of the Art of Optical Communication Systems

“ *In the beginning God said, "the four-dimensional divergence of an antisymmetric, second rank tensor equals zero", and there was light, and it was good. And on the seventh day he rested.* ”

Michio Kaku,

Introduction

THE introduction of long-haul optical fiber communication has been a key enabler of the information revolution, which pervades the modern society. Nowadays, the number and connection speed of internet users keeps increasing exponentially with time, generating an ever increasing amount of data traffic that demands matching communication capacity between network nodes. These advancements are driven by optical fibers channels, which characterized as transmission medium with low loss, huge bandwidth and low electromagnetic interference.

This chapter is organized as follows. The chapter starts from the introduction of current deployed fiber optics networks and their traffic evolution in section (1.1). Then, the single-mode fiber channel, section (1.2), and the origin of linear and nonlinear effects during the propagation of light in optical fibers is reviewed in section (1.3). This lead to the derivation of the

1.1. Fiber optic networks

nonlinear Schrödinger equation (NLSE), section (1.4), and Manakov equation, section (1.5). Finally, in section (1.6) the nonlinear Shannon limit of the fiber channel and methods to solve the capacity crunch is presented.

1.1 Fiber optic networks

The architecture of currently deployed optical networks can be roughly categorized into three groups, i.e. (i) long-haul to transoceanic core networks, (ii) Metro/regional and (iii) last-mile access networks. The schematic in Fig.(1.1) represents today's fiber optics networks. The classification of networks level is based mainly on the transmission reach and amount of data transmitted. The maximum distance covered by different levels of network-hierarchy is summarized in Table (1.1).

The global telecommunication network uses a (ultra) long-haul, and transoceanic links at a higher levels of the network architecture. These links form the optical backbone network and transport high capacity data over ultra-long reach (> 1000 km). These links demand technologies that enable long regeneration free transmission at low cost. Coherent optical transceivers at 112 Gb/s using dual polarization QPSK modulation format are currently deployed as long-haul transmission systems. Preliminary commercial solutions at a rate of 224 Gb/s using a dual-polarization 16-QAM format are available.

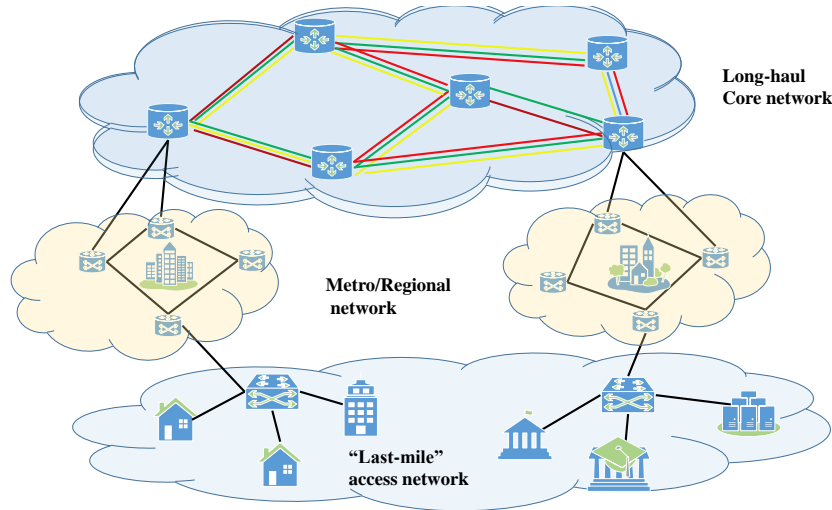


Figure 1.1: Optical network hierarchy; Long-haul core network, metro/regional and "last-mile" access network.

System	Distance (km)
Access	< 100
Metro	< 300
Regional	300 – 1,000
Long-haul	1,000 – 3,000
Ultra long-haul	> 3,000

Table 1.1: Optical network hierarchy by transmission reach.

Moving up in the optical network hierarchy, the metro/regional networks are responsible for connecting different metropolitan areas (< 300 km) or a small country (< 1000 km). The metro networks are evolving from the legacy ring or star topologies toward mesh architectures, in order to improve the capacity and reliability as well as increase link redundancy. The amount of data traffic carried by metro-networks is typically less than 100 Gbps.

The access (last-mile) network is the lowest level of a network hierarchy composed of a short links from the service provider to business or storage area networks. The link usually has a length up to 100 km. These networks are dominated by the legacy coaxial or twisted pair cables, however the service providers are changing the trend to optical fibers due to their much higher bandwidth-distance product and sound economical advantage, which enables high-speed connections over longer distances. Fiber-optics solutions are denoted as fiber to the 'x', where 'x' can be homes (FTTH), or curb (FTTC). The typical bandwidth of such networks scales to a few hundred Mbps, and are evolving towards 1 Gbps [30] – [31].

1.1.1 Traffic evolution of optical networks

The data traffic demand is expected to sky-rocket over the next few years. The latest global Internet Protocol (IP) traffic forecast by Cisco Visual Network Index (VNI) shown in Fig.(1.2) reported a global network traffic of 1.2 zettabytes (ZB), i.e. 10^{21} bytes, per year, or 96 ExaBytes (EB), i.e. 10^{18} bytes, per month [32]. The IP traffic is expected to grow with compounded growth rate of $\sim 24\%$ per year, resulting in roughly a three-fold increase in traffic over five years. In contrast, web-based applications, video streaming, and cloud computing have forced the short-reach optical link within data centers to grow even larger. The data center IP traffic is already exceeding 10 ZB, and it is expected to grow at $\sim 25\%$ per year as shown in Fig.(1.3(a)). The forecasts also projects that by the year 2021, that 71% of the global IP traffic distribution is expected to reside within data centers, while only 14%

1.2. The Optical Fiber Channel

accounts for user-destined traffic. The remaining 15% will be traffic between data centers, as indicated in Fig.(1.3(b)). This trend will be further stretched by machine-learning applications, whereby significant traffic is dedicated to answer simple queries.



Figure 1.2: Global IP data traffic forecast, in number of exabytes per month for the period of 2016-2021, as reported in the Cisco Visual Networking Index [32].

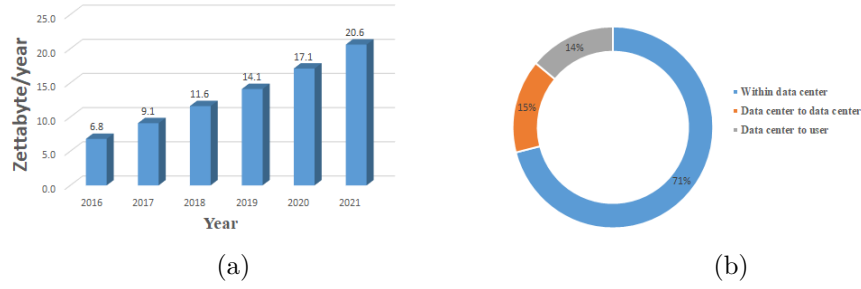


Figure 1.3: (a) Data centers global IP traffic growth. (b) projected data traffic distribution by destination in 2021. Source: Cisco Global Cloud Index, 2016-2021 [32].

1.2 The Optical Fiber Channel

Current high-speed long-haul data transmissions are carried out by optical fiber due to their low loss and large bandwidth when compared with other available waveguides [[1], Ch.2]. In a data communication scenario, optical fibers made of silica (SiO_2) glass are the workhorse of the industry. A typical fiber is composed by a cylindrical symmetric waveguide with three main layers, i.e. core, cladding, and external jacket. This structure allows light to mainly propagate inside the core in a guided mode, while a very small evanescent field propagates through the cladding. In order to guide light

inside the core, the refractive index of the core is kept slightly higher than that of the cladding. As a result, it becomes possible to propagate light inside a fiber thanks to total internal reflection (TIR).

Depending on the index profile, a typical fiber can be classified as either a step-index or a graded-index fiber. Most data transmission networks rely on step-index fibers, that show an abrupt change in the refractive index at the core and cladding interface. The light gathering capability of such fiber, also known as the numerical aperture (N.A.), is defined as:

$$\text{N.A.} = \sqrt{n_1^2 - n_2^2}. \quad (1.1)$$

where n_1 and n_2 represent the refractive index of the core and the cladding, respectively. In order to launch the maximum amount of light through the fiber, the value of the N.A. should be made as large as possible. However, as the N.A. increases, the light rays launched into the fiber take different path lengths to arrive at the output end of the fiber. As a result, the pulse at the fiber output exhibits a spreading in the temporal domain, which limits the achievable information rate (AIR) of the optical fiber. Such dispersive pulse spread is minimized by reducing the core radius and the refractive index difference between the core and cladding, so that few rays travel inside the core. Such fibers are called single mode fibers (SMFs) since they only support one spatial mode, also called the *fundamental mode*. As for today, the vast majority of deployed optical fibers are SMFs. In SMFs, the electric field of light, \mathbf{E} , that propagates at a carrier frequency, ω_0 , can be expressed as

$$\mathbf{E}_z(x, y, z, t) = F(x, y) A(z, t) \exp(i(\beta z - \omega_0 t)) \quad (1.2)$$

where $F(x, y)$ represents the spatial distribution of light in the transverse coordinates, t denotes time and β is the field propagation constant at λ_0 , which contributes to fiber dispersion. Furthermore, $A(z, t)$ is the slowly varying envelope of the light wave traveling in the z -direction.

In single-mode fibers, the difference between the refractive indices in the fiber's core and cladding is small. Such *weakly guiding* fibers support only two orthogonally polarized fundamental modes for wavelengths above a certain cutoff wavelength. Below cutoff, number of modes allowed to propagate depends on the normalized frequency or V-parameter of the fiber:

$$V = \frac{2\pi a}{\lambda} \text{N.A.} \quad (1.3)$$

where a is the core radius of the fiber and λ is the wavelength. Each mode is a solution of the wave equation, and is characterized by its own cut-off

1.3. Fiber impairments

frequency that depends on the fiber core radius, the operating wavelength, the difference in the refractive index of the fiber core and cladding. For typical single-mode fibers, i.e., ITU-T G.652 SMFs, the refractive index difference: $\Delta = n_1 - n_2 \approx 0.005$, core radius: $a = 4\mu\text{m}$, and the cutoff wavelength: $\lambda_{\text{cutoff}} \approx 1.2\mu\text{m}$. In order to allow only a single mode to propagate in a step-index fiber, the V number should have a value ≤ 2.405 . Fig.(1.4) illustrates the electric field profile of the mode propagating light in a single mode fiber. For $V \leq 2.4$, the fundamental mode field profile can be closely approximated by a Gaussian profile of form:

$$F(x, y) \approx \exp\left[-(x^2 + y^2)/w^2\right], \quad (1.4)$$

where the effective fiber core radius w is a wavelength-dependent fitting parameter. The Gaussian beam width parameter is evaluated by using

$$w^2 = \frac{a\sqrt{2}}{n_1 k_0 \sqrt{\Delta}} \quad (1.5)$$

for $k_0 = 2\pi/\lambda_0$. As illustrated in Fig.(1.4), the maximum field intensity of light is confined inside the core, with small evanescent field penetrating through the cladding. In the following subsection, the physical effects affecting wave propagation in optical fibers are summarized briefly.

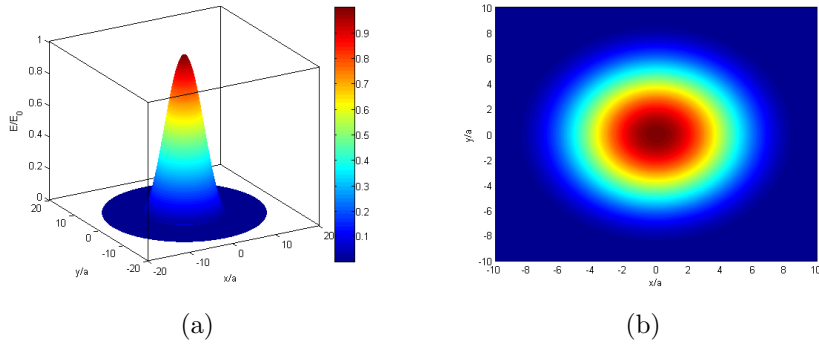


Figure 1.4: Illustration of an electric field distribution or mode solution of a single mode fibers along the cross-section.

1.3 Fiber impairments

As an optical signal propagates through an optical fiber, it is affected by several distortions. These distortions are categorized as linear and nonlinear

in nature. Linear fiber effects comprise attenuation, chromatic dispersion (CD), and polarization mode dispersion (PMD). On the other hand, nonlinear effects include the Kerr-effect, Raman scattering, and Brillouin scattering. These effects are discussed briefly in the following subsections.

1.3.1 Fiber loss

Optical fiber loss is the primary source of transmission power decay, and it depends on the wavelength (λ) of the signal as shown in Fig.(1.5). The optical power decays exponentially along the transmission distance according to Beer's law [1], given by

$$P(z) = P_o e^{-\alpha L}. \quad (1.6)$$

where P_o is the initial input power [W], α is the fiber attenuation coefficient, which typically is expressed in dB/km, and z is the propagation distance in [km]. Over sufficiently long distances z , the power of the detected signal will be too low, leading to a high error rate. Therefore amplification of the signal is needed for a long-haul optical communications.

Fiber loss can be regarded as equally distributed along the fiber length (when it is due to absorption and scattering) or occurs at a given point (due to connectors and splices). In an optical fiber, both silica and impurities in the glass contribute to the absorption of light, also called the **material absorption**. Besides silica, primary absorbers are residual hydroxyl ions (OH^-) and dopants used to modify the refractive index of the glass. The material absorption depends strongly on the wavelength of light. The OH^- absorption is predominant around $0.95 \mu\text{m}$, $1.244 \mu\text{m}$ and mostly $1.383 \mu\text{m}$ ¹. Today, in many single mode fibers the OH^- absorption peaks have been reduced greatly, e.g., in the "low water peak" or "zero water peak" fibers, which allows to extend WDM bands across these wavelengths, as shown in Fig.(1.5) ².

Main origin of transmission loss is scattering. Scattering occurs when photons encounter discontinuities in the refractive index and force light to be scattered at an angle outside of the numerical aperture of the fiber, leading to its leakage away from the fiber's core. During preform fabrication, silica molecules move randomly as a fluid. However, when the fiber solidified, microscopic fluctuations in material density occur, which lead to random

¹Gregory Lietaert, "Fiber Water Peak Characterization", JDSU white paper.

²<http://fiber-optic-catalog.ofsoptics.com/asset/single-mode-optical-fiber-selection-guide-fap-164-web.pdf>

1.3. Fiber impairments

and small variations in the refractive index on a scale smaller than the optical wavelength. Scattering from refractive index defects is called **Rayleigh scattering** and it is proportional to the inverse fourth power of the wavelength of light, i.e. $\sim 1/\lambda^4$.

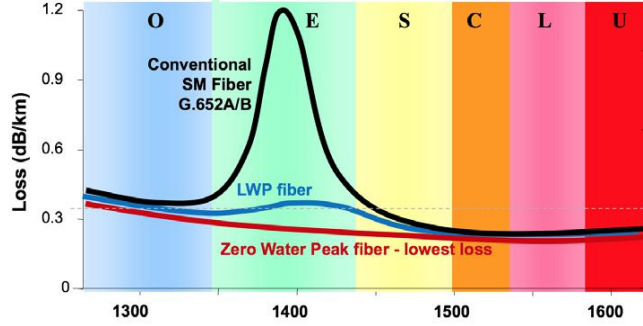


Figure 1.5: Attenuation curve of conventional G-652 fibers.

1.3.2 Chromatic dispersion

In optical fibers, group velocity of light is different for different frequency components of the wave. Therefore, the fiber medium is said to be dispersive and the effect is known as group velocity dispersion (GVD) or chromatic dispersion (CD). Consequently, an optical pulse will experience a temporal broadening leading to significant inter-symbol interference (ISI). By expanding the linear propagation constant β of the fiber mode around the carrier angular frequency ω_0 in a Taylor series [1], one writes

$$\beta(\omega) = \beta_0 + \beta_1 (\omega - \omega_0) + \frac{1}{2} \beta_2 (\omega - \omega_0)^2 + \dots \quad (1.7)$$

where β_m is the m^{th} derivative of β with respect to ω . An important parameter in optical communications is $\beta_2 [\text{ps}^2/\text{km}] = d^2\beta(\omega)/d\omega^2$ which is the GVD parameter of the fiber. It is related to the dispersion coefficient, $D = -(2\pi c\beta_2)/\lambda^2 [\text{ps}/(\text{nm} \cdot \text{km})]$, where λ and c represent the wavelength and speed of light.

Various types of single-mode fibers are characterized in terms of their dispersion parameter D . The *standard single-mode fiber* (SSMF) has a dispersion value of around 17 ps/nm/km at the minimum loss-window wavelength of $\lambda = 1.5 \mu\text{m}$. SSMFs exhibit zero CD in the 1.3 μm wavelength region. *Dispersion-shifted fibers* (DSF) is a type of single-mode optical fiber where their zero-dispersion wavelength shifted from the natural 1.3 μm to $\lambda = 1.5 \mu\text{m}$.

Their large-scale deployment in the WDM systems is prevented by nonlinear effects, since waves interact through four-wave mixing (FWM), being fully phase-matched in DSFs. In the 90s the *nonzero dispersion-shifted fibers* (NZDSF) with a reduced CD value (but non-null) has been deployed. The NZDSF fibers could have either slightly positive or slightly negative dispersion value at $1.55\text{ }\mu\text{m}$. *Dispersion-compensating fibers* (DCF) exhibit normal dispersion (i.e. $\beta_2 > 0 \Leftrightarrow D < 0$) at $1.55\text{ }\mu\text{m}$ [34]. Fig.(1.6) summarizes the dispersion curves for typical fiber types.

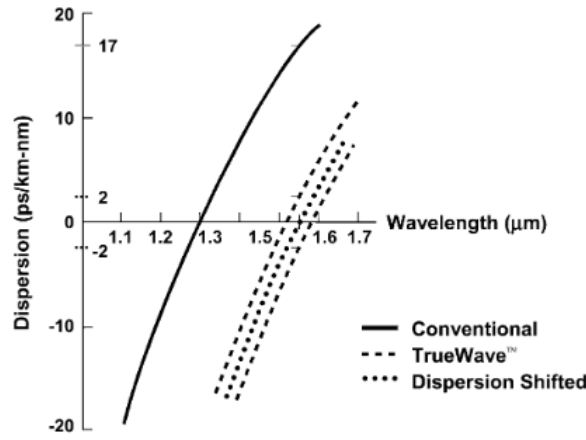


Figure 1.6: Dispersion curves of various single-mode fibers [37].

Dispersion is key factor affecting signal quality in long-haul optical fiber communication systems. Therefore its compensation is required. In mid-1990s, optical dispersion compensation based on dispersion compensation fibers (DCFs), fibers with an opposite sign of β_2 compared to the fiber deployed [23], was introduced in On-Off keying (OOK)-based optical transmission systems at 10 – Gb/s inline rate. Although DCFs can be used as part of a transmission link, they are commonly packaged as spool in conjunction with EDFAs. The advent of coherent detection enabled dispersion uncompensated links, thus the system design made a paradigm shift in the way dispersion is managed. Coherent detection receivers with digital equalization allow for full compensation of all linear channel impairments of the optical fiber channel. This allows for a pre- or post-compensation of CD using an electronic dispersion compensation (EDC) module instead of optical compensation modules such as (DCF) and fiber Bragg gratings (FBG) [33]. It has been proposed to employ an all-pass like frequency domain filter or finite impulse response (FIR) filter in the time domain to compensate CD in either the spectral or the temporal domain, respectively.

1.3.3 Polarization mode dispersion

Naturally single mode fibers support two orthogonally-polarized propagation modes. Ideally, optical fibers are circular-symmetric and isotropic waveguides, where the two orthogonal propagation modes have the same group velocity. However, in practice optical fibers are deployed in uncontrolled environments, where the fiber is continuously subjected to time-varying random mechanical forces. Together with intrinsic fiber stress, external forces break of cylindrical symmetry. Also fabrication of optical fibers leads to slight variations of fiber core ellipticity along its length, which breaks the degeneracy of orthogonal modes. Therefore, the fiber acquires birefringence. Due to fiber birefringence, the two polarization modes experience two slightly different propagation constant, β_f and β_s , where the subscripts f and s denote fast and slow polarization axes, respectively. The fiber birefringence, $\Delta\beta(\omega) = \beta_s(\omega) - \beta_f(\omega)$, leads to a random differential delay, also known as polarization mode dispersion (PMD), between the two orthogonally-polarized propagation modes. In the temporal domain, PMD manifests itself in the form of differential group delay (DGD), which is defined as [1]:

$$\tau = (\beta_s - \beta_f) L = \frac{L}{v_g^s} - \frac{L}{v_g^f}, \quad (1.8)$$

where L is the fiber transmission length, and $v_{g,f}, v_{g,s}$ are the different group velocities along the orthogonal slow and fast optical polarization axes, respectively. In practical fibers, the root mean square value of DGD $\Delta\tau_{\text{rms}} = D_p \sqrt{L}$ is considered, where D_p is the PMD parameter, usually provided by the fiber manufacturer and whose value for modern fibers is typically $D_p < 0.1 \frac{\text{ps}}{\sqrt{\text{km}}}$ [42].

1.3.4 Kerr nonlinearity

The linear approximation of a fiber channel is valid when the signal power is sufficiently low. However, for long-haul and WDM transmission systems, the launch power must be increased significantly in order to combat additive noise by the optical amplifier chain and keep the signal-to-noise ratio (SNR) to a level which permits error-free detection at the receiver. As signal power increases, the channel nonlinearity becomes significant, and leads to performance degradation.

Fiber nonlinearities are mainly due to two origins, the Kerr effect and inelastic scattering phenomena such as stimulated Raman scattering (SRS) and

stimulated Brillouin scattering (SBS). The Kerr effect originates from the power dependent refractive index of fiber [1], which can be written as

$$n = n_0 + n_2 \frac{P}{A_{\text{eff}}} \quad (1.9)$$

$$A_{\text{eff}} = \frac{\left(\iint_{-\infty}^{\infty} |F(x, y)|^2 dx dy \right)^2}{\iint_{-\infty}^{\infty} |F(x, y)|^4 dx dy}$$

where P [W] is the instantaneous optical power of the pulse, A_{eff} [m²] is the effective core area, typically varying in the range of 20 – 120 μm^2 for telecommunication fibers, depending on the fiber design, while n_0 and n_2 represent the linear and nonlinear refractive index of the fiber, respectively. Although $n_2 \sim 2.6 \times 10^{-20}$ [m²/W] is a tiny number for silica, the Kerr effect is still significant due to small effective area A_{eff} and the long transmission reach [2].

In WDM systems, nonlinear interactions between the signal in the channel of interest and signals in neighboring channels play a significant role. Intra-channel nonlinearity lead to self-phase modulation (SPM), and inter-channel nonlinearity lead to cross-phase modulation (XPM), and four-wave mixing (FWM) [2].

1.3.4.1 Self-Phase Modulation

The variation of signal intensity across a pulse lead to nonlinear refractive index variations in time. As a result, the signal phase is changed in proportion to the signal power. This effect is called self-phase modulation (SPM). SPM leads to frequency chirped pulses. Hence, SPM broadens the pulse spectrum while keeping the intensity profile unchanged in time [2]. The nonlinear phase shift is denoted by

$$\phi_{\text{SPM}} = \gamma P L_{\text{eff}}, \quad \gamma = \frac{2\pi n_2}{\lambda A_{\text{eff}}} \quad (1.10)$$

Here, the effective fiber length, $L_{\text{eff}}[1 - \exp(-\alpha L)]/\alpha$, measures the fiber length along which nonlinearities are effective. The SPM spectral broadening depends on the pulse shape, the peak power and the length of the transmission link. However, in some cases, a proper choice of both pulse shape and peak power may lead to a compensation between CD and SPM, which allows for the propagation of special undistorted pulses. These pulses are known as optical solitons and remain unchanged both in frequency and in time domain during their propagation.

1.3.4.2 Cross-Phase Modulation

When considering WDM systems, involving signals at a different wavelengths, cross-phase modulation (XPM) is another nonlinear effect originated by the power dependent refractive index. In the case of two channels that overlap in time, the nonlinear refractive index seen by each wave not only depends on the pulse itself, but also on the intensity of co-propagating waves. Therefore, all pulses mutually modulate their phases. The impact of the XPM-induced phase shift can be shown to be twice as strong as that of SPM on the i^{th} channel [2], and the total nonlinear phase shift reads as

$$\phi_{\text{XPM}}^i = \gamma \left(P_i + 2 \sum_{\substack{k=1 \\ k \neq i}}^N P_k \right) L_{\text{eff}} \quad (1.11)$$

The first term in Eq.(1.11) stand for the SPM contribution, whereas the second term represents the XPM contribution. The influence of XPM on a given system is severed when the number of channels is large, and channels are closely spaced with each other. Furthermore, in WDM systems, the XPM-induced phase shift on a the channel of interest is random, since at a given instant of time the amplitude of the neighboring channels varies, as each channel in WDM systems is independent of the other [35]. Due to the different group velocity of different wavelength channels there will be dispersive walk-off among them. This leads to averaging the power across neighboring channels leading to a reduction of the effect of XPM on the channel of interest. Therefore the impact of XPM can be reduced by increasing the spectral separation among channels, or increasing the GVD of the transmission fiber (i.e. the SMF-28 is much preferable compared to NZDSF) [36].

1.3.4.3 Four-Wave Mixing

In optical communications, FWM shows up when three spectral components with frequencies ω_1 , ω_2 , and ω_3 interact through the third-order nonlinearity, $\chi^{(3)}$, and generate a fourth spectral component with frequency ω_4 . The FWM process requires two basic conditions to be fulfilled, namely, the energy conservation and the phase matching condition. The first condition defines the frequency spacing between the spectral components that interact through FWM. The newly created spectral component is related to remaining frequencies as $\omega_4 = \omega_1 \pm \omega_2 \pm \omega_3$. The phase matching condition leads to the generation of a strong spectral components [2].

In the high nonlinear regime, the FWM results in a power transfer between channels; such power transfer may subtract power from certain channels,

thus forcing their SNR to degrade significantly. The efficiency of FWM tone generation heavily relies on phase matching between the three pumps (spectral components). Dispersion has a significant role on the efficiency of power transfer because of the phase matching condition is disrupted, which leads to a steep decrease in the efficiency of power transfer to newly generated frequencies. Systems that employ dispersion-shifted fibers (DSFs) overcome CD effects, while enhancing FWM. However, fibers such as NZDSF maintain a reduced CD value FWM efficiency.

1.3.5 Optical amplification and noise

When signals propagates in optical fibers, their power decays exponentially due to fiber loss. As a result, after a certain distance the SNR of the received signal will be too low, resulting in too high BER. Therefore signal amplification is needed in long-haul communications. Optical signal amplification can be done either in a lumped or in a distributed fashion [38]. These two categories differ by the manner in which the amplification is introduced.

Traditional erbium-doped fiber amplifiers (EDFAs) are lumped amplifiers, since amplification occurs in erbium-doped fibers (EDF) located in a compact amplifier module [14],[15]. These amplifiers are placed periodically every $\sim 50 - 100$ km span length, as illustrated in the schematics diagram of Fig.(1.7). The EDFA provide broadband amplification of optical signals over about 30 nm. For long-haul transmissions, the available bandwidth of the optical amplifiers in C-band and L-band is summarized in Table (1.2)³. Unfortunately, amplification in a EDFA is accompanied by the generation of amplified spontaneous emission (ASE) noise as shown in the inset of Fig.(1.7). ASE noise can be modeled as a complex additive white Gaussian noise (AWGN), which can be considered to be independent and identically distributed (i.i.d.) [1]. The one-sided power spectral density per polarization component of the noise added by an amplifier is

$$N_{\text{ASE}} = (G - 1) h\nu n_{\text{sp}}, \quad (1.12)$$

where $G = \exp(\alpha L)$ is the gain needed to compensate for the attenuation in the fiber of length L , h is Planck's constant, ν is the optical center frequency, and n_{sp} is the spontaneous emission factor. The spontaneous emission factor cannot be directly observed, so the optical amplifier is characterized by its noise figure NF . The NF is calculated assuming an ideal receiver as [16]

$$NF = 2 \cdot n_{\text{sp}} \cdot \frac{G - 1}{G} \quad (1.13)$$

³<https://www.fiberlabs-inc.com/glossary/about-optical-communication-band/>

1.3. Fiber impairments

In a fiber optic transmission link with N_A amplifiers, the optical signal to noise ratio (OSNR) is given by

$$\text{OSNR} = \frac{P_s}{N_A \cdot P_{\text{ASE}}} \quad (1.14)$$

where P_s is the transmitted power, P_{ASE} is the spontaneous emission noise power defined by

$$P_{\text{ASE}} = 2 \cdot N_{\text{ASE}} \cdot B_{\text{opt}} \quad (1.15)$$

where B_{opt} is the optical resolution bandwidth of the optical spectrum analyzer (OSA).

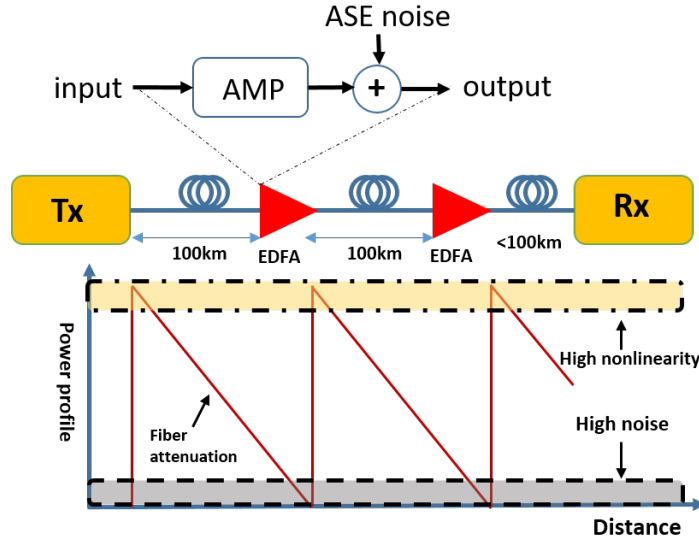


Figure 1.7: Schematic representation of lumped amplification using EDFAs.

Band	Technology	Wavelength [nm]	Use
O-band	SOA	1260 - 1360	Legacy short reach transmission.
E-band	SOA	1360 - 1460	Extended band for short reach transmissions.
S-band	Tm-DFA	1460 - 1530	Extended C-and L-band.
C-band	EDFA	1530 - 1565	Metro/ (ultra) long-haul transmission.
L-band	EDFA	1565 - 1625	Expanded C-band (DWDM) band.

Table 1.2: Different optical communication wavelength bands.

The transmission band range from the original O-band to the L-band. Single mode fiber transmission began in the O-band. This band is extended to the

so-called E-band in the $1.3\mu\text{m}$ loss windows. However, the E-band correspond to high transmission loss region among the five bands (i.e. this represents the water peak region). Though the dehydration technique is used during the fiber production in order to reduce the attenuation value in the E-band.

Current systems, however, use the S-, C- and L-band because of the low optical losses in glass fiber. EDFAs are a key enabling technology in the C- and L-band systems instead of a semiconductor optical amplifiers (SOAs) used in the O- and E-band. However, EDFA are less efficient in the L-band. In recent years, EDFAs became commercial available for both the C- and L-band⁴.

On the other hand, distributed-amplification provide amplification along the transmission fiber itself, by taking advantage of the SRS nonlinear effect [61]. This enables distributed Raman amplification (DRA), i.e. the transmission fiber itself is pumped at the end of each span to provide amplification of the signal. Since gain occurs along the entire fiber length, DRA prevents a signal to being attenuated to a too lower power level, thus improving the Optical Signal to Noise Ratio (OSNR) of the transmitted signal. Regardless of the amplification scheme, the optically amplified signal undergoes OSNR degradation due to added noise by the amplifiers.

The impact of noise in a long-haul systems is reduced by increasing the launch power into the fiber. However, the power increase moves the channel into the nonlinear regime, where the signal is distorted by nonlinear impairments. Thus, the transmission regime can be divided into a linear regime, where the system performance is limited by CD and noise, and the nonlinear regime, where the system performance is limited by fiber nonlinearities. Therefore, it is essential to identify the optimal operating point of a system. This optimal launch power depends on factors such as transmission reach, Kerr nonlinearity coefficient γ and dispersion parameter (D), the noise figure (NF) of EDFAs, the type of modulation, and the compensation DSP used at the receiver. ASE noise can be modeled as an AWGN process in the linear regime at end of the link. In the nonlinear regime, however, the ASE model deviates from white to colored noise corresponding to a non-Gaussian random process [39],[40].

⁴<https://www.lightwaveonline.com/articles/print/volume-16/issue-9/special-report/amplifiers-designed-for-the-l-band-53489027.html>

1.4 Scalar nonlinear Schrödinger equation

The propagation of an optical signals in optical fibers is governed by the generalized scalar nonlinear Schrödinger equation (NLSE) [2]. The evolution of the slowly varying amplitude of the optical field envelope $A(\ell, t)$ obeys the NLSE

$$\frac{\partial A}{\partial \ell} = -i\frac{\beta_2}{2}\frac{\partial^2 A}{\partial t^2} + i\gamma|A|^2A - \frac{\alpha}{2}A + n(t) \quad (1.16)$$

where β_2 is the group velocity dispersion coefficient, γ is the nonlinear coefficient, α is the loss coefficient of the fiber, $\ell \in [0, L]$ is the distance of propagation, and $n(t)$ is the noise. In the stated form, t is the time coordinate, in a reference frame that moves with the group velocity of the pulse. In order to remove the dependence on any specific channel, i.e. the fiber parameters, it is common to normalize Eq.(1.16). Neglecting the loss and noise terms, the normalized form of the NLSE reads as:

$$\frac{\partial q(z, \tau)}{\partial z} = -i\frac{\partial^2 q(z, \tau)}{\partial \tau^2} + i2s|q(z, \tau)|^2q(z, \tau), \quad (1.17)$$

where τ and z represent the normalized time and distance, respectively. Here, $s = +1$ corresponds to the defocusing (normal dispersion) regime while $s = -1$ corresponds to the focusing (anomalous dispersion) regime. Eq.(1.17) is obtained from Eq.(1.16) by performing the change of variables

$$q = \frac{A}{\sqrt{P_0}}, \quad \tau = \frac{t}{T_0}, \quad z = \frac{\ell}{L_D}, \quad (1.18)$$

with $L_D = 2T_0^2/|\beta_2|[m]$ and $P_0 = \frac{2}{\gamma L_D}[W]$. Here, L_D represents the dispersion length, which is the propagation distance after which the dispersive effects become important, and P_0 is the peak power of the pulse. The normalization time T_0 , which is the symbol period, is a free parameter.

An analytical solution to the NLSE can be formally obtained by a Volterra series expansion [52]. Several algorithms exist to numerically simulate the wave propagation described by the NLSE; in this thesis, the *split-step Fourier method* (SSFM) is used for numerical simulations. The idea of the SSFM algorithm is to divide the fiber into small segments of length h [1]. In each segment, linear and nonlinear fiber effects are supposed to act independently so that the exact solution to Eq.(1.16) can be approximated as

$$A(z+h, t) \approx \exp(h\widehat{D}(t)) \exp(h\widehat{N}(A(z, t))) A(z, t) \quad (1.19)$$

where \widehat{D} is the linear operator given by

$$\widehat{D}(t) = -\frac{\alpha}{2} - i\frac{\beta_2}{2}\frac{\partial^2}{\partial t^2} \quad (1.20)$$

and \widehat{N} is the nonlinear operator that reads as

$$\widehat{N}(A(z, t)) = i\gamma|A(z, t)|^2. \quad (1.21)$$

The choice of the step size h represents a trade-off between accuracy and computational complexity. Fig.(1.8) illustrates the temporal and frequency domain pulse broadening induced by CD and SPM, respectively. Algorithm 1 summarizes the implementation of the simplified version of the split-step Fourier method.

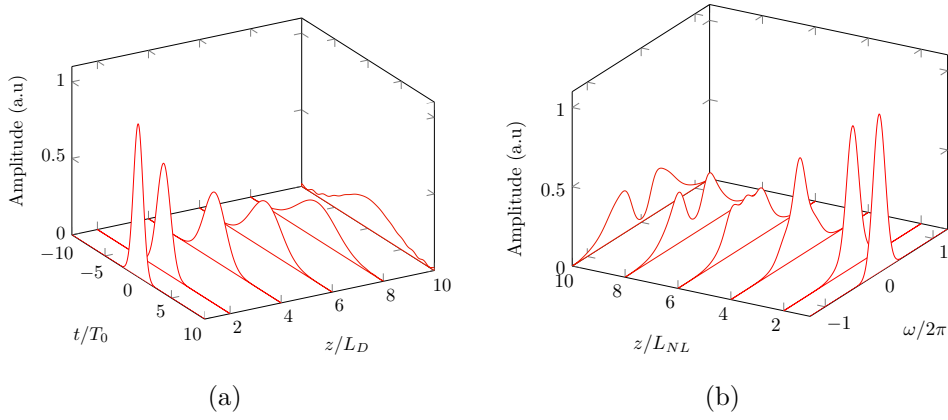


Figure 1.8: Illustration of pulse broadening effect due to GVD (a), and (b) SPM-induced spectral broadening of a Gaussian pulse.

Algorithm 1 SSFM algorithm

```

1: procedure SSFM( $A, \alpha, L, \gamma, \beta_2, h$ )
2:    $\widehat{D}$                                  $\triangleright$  Compute linear operators using Eq.(1.20)
3:    $\widehat{N}$                                  $\triangleright$  Compute nonlinear operators using Eq.(1.21)
4:    $\widetilde{A} \leftarrow \mathcal{F}(A)$            $\triangleright$  Take spectrum of input
5:   for  $\langle$ for step size  $0:h:L\rangle$  do
6:      $\widetilde{A} \leftarrow \widetilde{A} * \exp\left(\frac{h}{2} * \mathcal{F}(\widehat{D})\right)$   $\triangleright$  Linear operation in Fourier domain
7:      $A \leftarrow \mathcal{F}^{-1}(\widetilde{A})$            $\triangleright$  Time domain conversion
8:      $A \leftarrow A * \exp(h * \widehat{N}(A))$   $\triangleright$  Nonlinear operation in time domain
9:      $A \leftarrow \mathcal{F}(\widetilde{A})$            $\triangleright$  Fourier domain conversion
10:     $\widetilde{A} \leftarrow \widetilde{A} * \exp\left(\frac{h}{2} * \mathcal{F}(\widehat{D})\right)$   $\triangleright$  Linear operation in Fourier domain
11:     $A \leftarrow \mathcal{F}^{-1}(\widetilde{A})$            $\triangleright$  Time domain conversion
12:   return  $A$                          $\triangleright$  Return nonlinear pulse propagation
    
```

1.5. Coupled nonlinear Schrödinger equation

For the numerical simulations and experimental work in this thesis, the fiber parameters specified in Table 1.3 have been used.

Type	α [dB/km]	D[ps/nm/km]	$A_{\text{eff}}[\mu\text{m}^2]$	γ [1/W km]
SSMF	0.2	+17	80	1.47
DSF	0.2	0	50	2.35
NZDSF+	0.2	+2.8	53	2.22
NZDSF-	0.2	-2.3	57	2.06
DCF	0.5	-80	20	5.88

Table 1.3: Typical parameters of different fiber types at $\lambda = 1.55 \mu\text{m}$.

1.5 Coupled nonlinear Schrödinger equation

In single-mode fibers, two orthogonal fundamental modes are able to propagate. However, in the derivation of the scalar NLSE of eq.(1.16), an ideal geometry of the fiber was assumed, where the fundamental modes have identical propagation properties. In practice, however, all fibers exhibit birefringence and polarization-related effects. In a polarization division multiplexed (PDM) scheme, two coupled nonlinear Schrödinger equation (CNLSE) [42] are required to describe light propagation in a single-mode fiber. Signals propagating in the two orthogonal polarization states can be described by the vector propagation equation

$$\frac{\partial \mathbf{A}}{\partial z} = -\frac{\alpha}{2} \mathbf{A} + \Theta(z) \left[\frac{\Delta\beta_0}{2} \mathbf{A} - \frac{\Delta\beta_1}{2} \frac{\partial \mathbf{A}}{\partial t} \right] - i \frac{\beta_2}{2} \frac{\partial^2 \mathbf{A}}{\partial t^2} + i\gamma \left[|\mathbf{A}|^2 \mathbf{A} - \frac{1}{3} (A^\dagger \sigma_3 \mathbf{A}) \sigma_3 \mathbf{A} \right] \quad (1.22)$$

where $A = [A_x(z, t) A_y(z, t)]^T$ is the Jones vector of light, that models x and y polarization, $(\cdot)^T$ and $(\cdot)^\dagger$ stand for transpose and transpose conjugate operators, while β_0 , and β_1 account for birefringence and differential group delay, respectively. The polarization mode-coupling is defined as

$$\Theta(z) = \sigma_1 \cos(\theta(z)) + \sigma_2 \sin(\theta(z)) \quad (1.23)$$

where $\theta(z)$ introduces a random rotation of birefringence axes in the z direction, and the Pauli spin matrices are given by

$$\sigma_1 = \begin{bmatrix} 1 & 0 \\ 0 & -1 \end{bmatrix}, \quad \sigma_2 = \begin{bmatrix} 0 & 1 \\ 1 & 0 \end{bmatrix}, \quad \sigma_3 = \begin{bmatrix} 0 & -i \\ i & 0 \end{bmatrix} \quad (1.24)$$

Note that the birefringence beat length (typically few meters) is considered to be much shorter than the nonlinear length (typically several kilometers). In addition to the fiber impairment presented above, Eq.(1.22) introduces polarization dependent linear impairments originating from the two polarizations such as polarization mode dispersion (PMD) and polarization dependent loss (PDL).

Eq.(1.22) poses a significant challenge for a numerical solutions, as the birefringence coefficient $\theta(z)$ varies over a small length when compared with the PMD, CD and the Kerr nonlinearity lengths. Therefore, an accurate solutions require tracking of the rapid change of varying birefringence. To overcome such problem, the combined action of Kerr nonlinearity with birefringence can be averaged over the Poincaré sphere, in order to obtain the Manakov equation. Neglecting the PMD and PDL effects, the Manakov equation is given by (ME) [43]

$$\frac{\partial \mathbf{A}}{\partial z} = -\frac{\alpha}{2} \mathbf{A} - i \frac{\beta_2}{2} \frac{\partial^2 \mathbf{A}}{\partial t^2} + i \gamma \frac{8}{9} |\mathbf{A}|^2 \mathbf{A} \quad (1.25)$$

Neglecting fiber loss, Eq.(1.25) can be expressed in a normalized form as

$$\frac{\partial \mathbf{q}(z, \tau)}{\partial z} = -i \frac{\partial^2 \mathbf{q}(z, \tau)}{\partial \tau^2} + i 2s |\mathbf{q}(z, \tau)|^2 \mathbf{q}(z, \tau) \quad (1.26)$$

using the change variable

$$\mathbf{q} = \frac{\mathbf{A}}{\sqrt{P_0}}, \quad \tau = \frac{t}{T_0}, \quad z = \frac{\ell}{L_D} \quad (1.27)$$

with

$$L_D = \frac{2T_0^2}{|\beta_2|}, \quad P_0 = \sqrt{\frac{2}{8/9\gamma L_D}}. \quad (1.28)$$

1.6 Capacity of optical fiber channels

Present day optical networks, including (ultra) long-haul and trans-oceanic links, are largely dominated by the use of single-mode fiber. The fiber channel combines a large bandwidth and low attenuation, with a low-loss bandwidth of $\sim > 50$ THz, so that capacity is limited by dispersion, and nonlinear effects and ASE accumulation [1].

The amount of data that can be transmitted reliably over any channel, including optical fibers, is limited by the channel's capacity. Determining channel capacity is the foundation of *information theory*, as described by *Claude*

1.6. Capacity of optical fiber channels

Shannon in his 1948 publication *A mathematical theory of communication* [27]. Shannon showed that, for a band-limited AWGN channel, the channel capacity C is given by

$$C = 2 \cdot B \log_2 \left(1 + \frac{P_{\text{avg}}}{N_0 B} \right) \quad (1.29)$$

where B is the channel bandwidth, N_0 is the power spectral density of accumulated noise, and P_{avg} is the average power of the signal. Here, the factor 2 describes the two information-carrying polarization states of the fiber. From a simplified channel model that neglects all nonlinear effects, an amplified optical link can be considered as AWGN channel. However, with the advent of high-speed and long-haul optical fiber communications, the difficulty in the estimation of channel capacity is mostly due to the presence of fiber nonlinearity. Nonlinear phenomena in long-haul systems are mainly determined by Kerr induced nonlinear distortions such as SPM, XPM and FWM [28], [29], [47]. The impact of these distortions rapidly increases with the launch power and the propagation distance, causing a progressive signal degradation and thus limiting the maximum achievable SNR for a given optical link.

1.6.1 Fiber capacity increment

Communicating through a nonlinear channel, such as an optical fiber, poses many practical and theoretical challenges. Capacity increases were mostly facilitated by improving the fiber quality and the electronics for transmitters and receivers. Coherent detection techniques in combination with a pre-existing technologies such as EDFAs and WDM, led to a dramatic increase of the capacity of the fiber channel though accessing every degree of freedom (DoF) available for modulation and multiplexing of optical signals [45]. Fig.1.9 summarizes the five DoF for an electromagnetic wave that propagates in an optical fiber, as proposed in [45]:

Time: The time dimension is exploited in the optical time-domain multiplexing (OTDM) technique. OTDM generates a high-speed serial data stream and sends it in temporal succession. Pulse shaping can be used to compress the spectrum of signal pulses subject to fundamental time/frequency constraints. The OTDM technique is fundamentally compatible with modern multi-level quadrature amplitude modulation (QAM) formats and digital coherent detection to increase the achievable information rate.

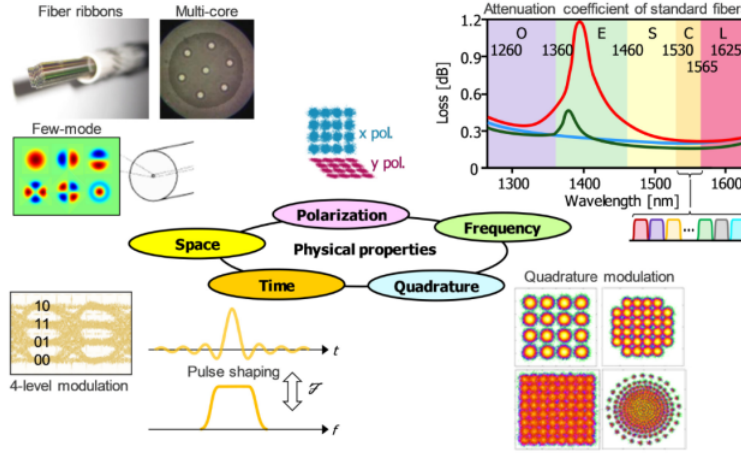


Figure 1.9: Physical available degree-of-freedom for modulation and multiplexing of optical signal [45].

Frequency: Since optical fiber provides a huge bandwidth, one may transmit multiple parallel channels at different carrier frequencies over the same link. This technique is called wavelength-division multiplexing (WDM), and it allows to tremendously increase optical fiber systems capacity by transporting independent wavelength channels.

Quadrature: The introduction of coherent detection allows access to the real and imaginary components of the electromagnetic wave, which are referred to as the two quadrature dimensions. Consequently, spectrally efficient modulation formats such as M-level QAM can be used. Recently, techniques such as probabilistic shaping of QAM were proposed to increase the system throughput [46].

Polarization: As opposed to direct detection receivers, coherent detection allows to access the polarization DoF. Due to the possibility to transmit different data in each polarization mode, the capacity of channel increases by a factor of 2 in polarization-division multiplexed (PDM) systems.

Space: One of the most promising approaches for increasing the capacity of the optical fiber channel is space-division multiplexing (SDM) in multi-mode or multi-core optical fibers. With this approach, information is transmitted simultaneously over a number of parallel spatial paths, while relying on multiple-input and multiple-output (MIMO) DSP to resolve each channel and issues related to mode coupling during pulse propagation.

Despite the effort to increase capacity by exploiting these DoFs, the Kerr nonlinearity is still regarded as the ultimate limit to the achievable channel capacity.

1.6.2 The nonlinear Shannon limit

Unlike linear channels, where signal transmission capacity can be increased indefinitely by using higher signal powers and higher-order modulation formats, Eq.(1.29), the capacity of a nonlinear channel does not grow indefinitely and it has a maximum value. This maximum capacity is called the *nonlinear Shannon limit* [47]. Such fundamental limit imposed by Kerr nonlinearity on the fiber channel can be demonstrated by examining the dependence of the achievable information-rate on optical power. Fig.(1.10) depicts a typical example of the achievable fiber capacity of a nonlinear optical communication systems. The optimal launch power where the capacity reaches its maximum value is referred to as nonlinear threshold (NLT) power. The figure shows that in the linear regime, where the launch power is less than the optimal NLT, the spectral efficiency (SE) increases as the logarithm of signal power. The SE is defined as the ratio of system capacity (C) to system bandwidth (B) [45],

$$SE = \frac{C}{B}. \quad (1.30)$$

Here, fiber nonlinearities limit the signal power below the NLT. As the signal power increases above the NLT, fiber nonlinearity introduces an upper bound to the spectral efficiency, thus limiting the capacity in fiber optic communications systems. In addition to the capacity limit, fiber nonlinearities also restrict the transmission reach of any high-speed long-haul system. In fact, fiber nonlinearity is the major limiting factor today for any such system. As a result, it is of great interest researching for approximated closed-form expressions which describe the impact of fiber nonlinearity on the transmission performance. Furthermore, the analytical characterization of the relationship between the input and output signal of the fiber links is of paramount importance for solving the optical fiber channel capacity problem. This characterization is usually referred to as channel modeling. The most common approach is the Gaussian noise (GN) model, which was first introduced by Poggiolini et. al. [48]. According to the GN-model, distortions arising from fiber nonlinearity can be accounted for as a source of additive (Gaussian) noise, which is independent of both the signal and ASE noise. As a result, a nonlinear noise source adds in power to the ASE noise accumulated over

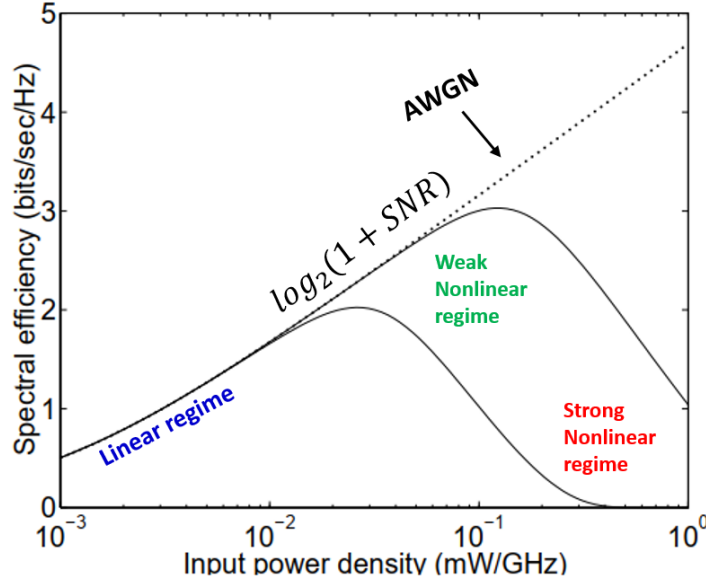


Figure 1.10: Estimated of achievable data-rates versus input power of a nonlinear fiber channel [47].

the transmission reach, which is usually referred to as nonlinear interference (NLI). This allows the adoption of a detection strategy tailored to AWGN channels.

According to the GN-model, nonlinear distortions result from both the signal-signal and the signal-noise interactions. However, non-deterministic signal-noise interactions contribute significantly to the fiber capacity limit as they are hard to predict and fully compensate for. Nevertheless, considering deterministic signal-signal interactions have opened a possible transparent and low-cost digital post-compensation solution to enhance both the optimum launch power and the maximum achievable capacity.

1.7 Fiber nonlinearity mitigation

The mitigation methods for nonlinear optical fiber impairments described in previous section can be broadly classified into two categories: optical compensation, and electronic compensation through DSP [49]. Examples of optical technique is optical phase conjugation (OPC) and optical back-propagation (OBP) [50] – [51]. The physical implementation of optical compensation techniques requires the introduction of additional active optical components in the transmission system. Unlike optical methods, with the advent of

coherent optical transmission systems, it became possible to implement digital nonlinear equalization methods such as digital back-propagation (DBP) [53], and the Volterra series transfer function method (VSTF) [52]. Digital compensation techniques can provide mitigation of both linear and nonlinear effects in coherent optical communication systems and fall into two main categories: (a) pre-compensation methods that create a more resilient signal to fiber impairments prior to fiber propagation; and (b) post-compensation techniques, which are applied on the distorted signal after propagation. In the following a brief summary of DBP and VSTF-based equalization techniques are presented.

1.7.1 Digital back-propagation

During fiber propagation, optical signals become significantly distorted owing to linear and nonlinear fiber impairments. A digital technique can be used as a general method for the compensation of both linear and nonlinear effects. Such a technique involves solving the spatially inverted NLSE, enabling to exactly recover the transmitted signal from the received one, which leads to the concept of digital back-propagation (DBP) [53]. The effectiveness of the DBP technique depends on a complete knowledge of the transmission link, such as the fiber parameters α , β_2 and γ , the EDFA gain, and the fiber span length L_s . In the absence of noise, taking advantage of the fact that the NLSE is an invertible equation, propagating the output signal through a virtual fiber with symmetric parameters $(-\alpha, -\beta_2, -\gamma)$ inverts the channel effects. To back-propagate the signal through a section of virtual fiber which extends from $z + h$ to z , where h represents a given increment of the spatial coordinate, methods such as non-iterative asymmetric SSFM and iterative symmetric SSFM have been used, as depicted in Fig.(1.11). Despite its high computational complexity, DBP has been recently proposed as an effective way for jointly compensating the linear and nonlinear impairments and is often used as a benchmark against other equalization techniques. For a given step h the NLSE is solved by ignoring the nonlinear term, and in the next step, it is solved by ignoring the dispersion term.

Multi-channel digital back-propagation (MC-DBP) has been proposed as a promising approach for compensating both intra-channel and inter-channel deterministic fiber Kerr nonlinearities. In a single-channel transmission system, MC-DBP can perfectly mitigate the deterministic signal-signal interactions and nonlinear inter-symbol interference (NISI). This means, in the absence of noise, that DPB can fully compensate deterministic intra-channel impairments such as CD and SPM, and inter-channel effects such as XPM

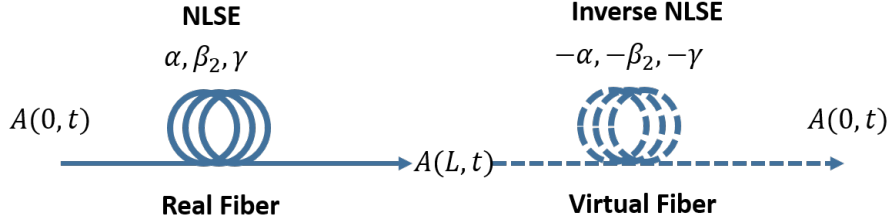


Figure 1.11: Illustration of forward propagation in real fiber governed by NLSE and digital backward propagation (DBP) through virtual fiber using the inverse NLSE.

and FWM jointly [54]. In addition, it has also been demonstrated that DBP allows to reduce the growth of nonlinearly-induced noise with increasing optical power [55]. However, DBP does not account for non-deterministic channel impairments such as the nonlinear signal-noise interactions (NSNI), hence it can be applied in situations where the accumulated ASE noise in fiber links, the transmitter-receiver induced imperfections and uncertainty in fiber parameters can be neglected. The first DBP based equalizations were performed on the transmitter-side as electronic pre-compensation, in order to improve the performance of direct detection systems. With the advent of coherent detection, post-compensation based on DBP in a single-polarization, either in single-channel or WDM systems, has become a widely acceptable implementation [56]. This approach has enabled adaptive equalization without full knowledge of the transmission system, and the need to have high-precision and high-resolution DAC technology. Furthermore, the DBP can be implemented as pre- and post-compensation method to reduce the NSNI effect.

1.7.2 VSTF based nonlinear equalizer

Nonlinear time-invariant casual systems such as the scalar NLSE can be solve numerically without the need for sub-span iterations, by using a 3^{rd} -order Volterra series transfer function (VSTF) [52]. This method enables the separate evaluation of the linear and nonlinear operators in the NLSE. As a result, recently different digital nonlinear equalizers (NLEs) and pre-distorters based on the inverse VSTF (IVSTF) have been proposed, in order to mitigate partially the nonlinear distortions introduced by the fiber link. The IVSTF can be implemented in the time domain (TD), in the frequency domain (FD) and in a hybrid configuration, where the CD is compensated in the spectral-domain and the nonlinearity in the temporal-domain [58].

1.7. Fiber nonlinearity mitigation

IVSTF equalization is applied in parallel as shown in Fig.(2.1(a)), and involves three stages; the first stage is the CD compensation per span in the frequency domain by using an all pass-like filter. The second stage involves a time domain nonlinearity equalization, and finally the equalized field is obtained by the addition of the independent linear and nonlinear equalization contributions. Note that the IVSTF NLE is analogous to the forward VSTF, but with symmetric fiber parameters $(-\alpha, -\beta_2, -\gamma)$ [59]. The authors have demonstrated performance gain using the IVSTF-NLE when compared to various DBP-SSFM equalizers in 3-channel WDM using 4-sub-band PDM-16QAM OFDM transmission in 1000 km SSMF. Fig.(2.1(b)) shows that IVSTF-NLE has ~ 0.6 dB gain in Q-factor with respect to unequaled systems, which is comparable to DBP-SSFM₆₄.

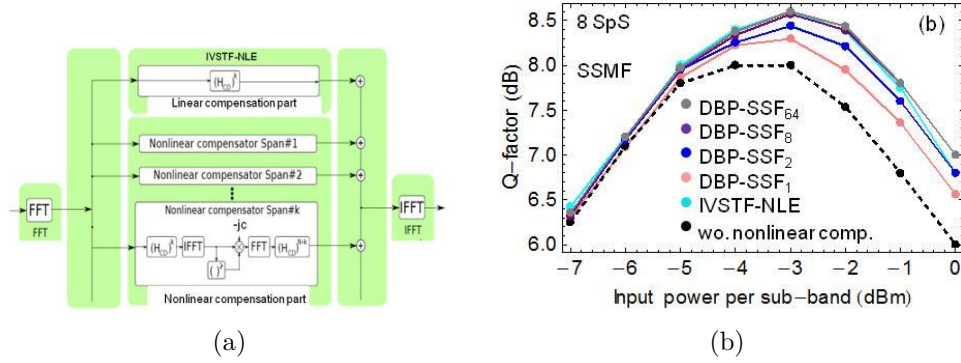


Figure 1.12: (a)Block diagram of IVSTF-NLEs equalizer; and (b) Q-factor vs. input power performance improvement obtained for 400 Gb/s without/with IVSTF-NLEs and DBP-SSFM_{1,2,8,64} in SSMF (after [59]).

In WDM systems, it is not possible to perform joint transmission and detection, since many channels join and leave the optical link at reconfigurable optical add-and-drop multiplexers (ROADM), without being acknowledged by other channel users, thus the information from neighboring channels is unavailable. For this reason, in a network scenario, both DBP and IVSTF based NLEs are used mainly for the channel of interest, thereby reducing the compensation of inter-channel effects which are treated ultimately as noise. However, the potential performance gain for such nonlinear mitigation approaches is limited to $\sim 0.5 - 1$ dB, because of inter-channel interference (ICI) and noise-nonlinearity interactions. Because the noise generated by different noise sources in the link is back-propagated during post-compensation, undesirable noise amplification and artificial signal-noise interactions occur

at the receiver. Additionally, inter-channel nonlinear interactions strongly depend on the polarization state of each channel. For typical values of PMD parameters, multi-channel NLEs techniques become ineffective as the back-propagation bandwidth increases. Furthermore, these techniques requires very high computational complexity even in single channel compensation. Therefore, the practical implementation of NLEs demands an improved algorithm that could provide efficient compensation at a relatively low computational cost [57] – [44].

1.8 Summary

In this chapter, the architecture, the traffic evolution, and advanced modulation techniques inspired by coherent detection in optical fiber networks have been reviewed. Prior to outlining the scalar nonlinear Schrödinger equation (NLSE) and the Manakov equation that govern signal propagation in nonlinear dispersive fibers, linear impairments were described. Next, the nonlinearity induced channel capacity for the optical fiber channel and the compensation methods proposed to mitigate nonlinear effects in order increase such capacity have been presented.

One can observe that communicating through a nonlinear channel poses many practical and theoretical challenges. Basic communication methods and paradigms used in current fiber optic communications are borrowed from linear channels, thus have to be re-examined. This includes questions such as how to encode information and modulate signals, multiplex different information channels, detect signals at the output of a link in the weak- and strong-nonlinear regimes, and so on. These questions necessitate an accurate modeling of nonlinear channels. The search for the solution to these questions leads to the revival of eigenvalue communication systems, based on the idea of the inverse scattering transform (IST). The scope of this thesis is to discuss the implementation and experimental validation of such techniques.

Chapter 2

Optical Transmission Systems based on the Nonlinear Fourier Transform

“ Everything should be made as simple as possible, but not simpler.”

Albert Einstein,

2.1 Introduction

IN contrast to linear channels, optical fibers exhibit nonlinearity, and signal amplification is a source of distributed noise. The interplay between dispersion, nonlinearity, and noise over the transmission length makes light propagation in fibers a complex process making it difficult to establish a channel input-output map for the simple estimation of the capacity of optical fiber channels. As described earlier, the evolution of optical signals in a fiber is modeled through the scalar NLSE, Eq.(1.16), for single-polarization, and the Manakov equation, Eq.(1.25), for a dual-polarization signal. These equations do not lend themselves to an analytic solution except for some specific cases, also known as soliton solutions. However, approximate analytical solutions exist for the fiber-optic channel. The NLSE, Eq.(1.17), is one of a very special class of nonlinear equations, that is an integrable nonlinear equation, which can be solved by using the NFT technique, which was first introduced by Zakharov and Shabat [60]. With the help of the NFT, a sig-

2.1. Introduction

nal can be represented by its continuous (dispersive) and discrete (solitonic) nonlinear spectrum. While the evolution of signals along the fiber is remains complex in the temporal domain, all the complexity disappears in the spectral domain, where the wave evolution is linear. Based on this, Hasegawa et al. came up with the proposal to use multiple optical solitons in a communication system, a technique also known as eigenvalue communication [61]. Such communication method integrates the Kerr nonlinear effect into the system design, so that the optical envelope maintains its shape along fiber propagation. The eigenvalue communication is preceded by the classical soliton communication. Soliton communications have been investigated intensively in the 1990s [62], and the experimental demonstration of 10 Gbit/s data transmission over one million kilometers has been provided by Nakazawa et al. [63]. However, soliton based ultra-high data rate communications suffer from effects such as soliton-to-soliton collisions, inter-channel cross-talk, noise, loss, high-order dispersion and, SRS, etc. [62].

With the advent of coherent detection, complex advanced digital signal processing, and the maturity in the EDFA and WDM technologies, attention was diverted from solitons to coherent long-haul transmission, in order to significantly improve the system transmission capacity. However, once again Kerr nonlinearity remained the limiting factor even with advanced high-spectral efficient modulation formats and error-correcting codes. Moreover, partial nonlinearity mitigation techniques in a weakly-nonlinear regime, such as DBP, VSTF, and others, exhibited limited performance gain due to noise-nonlinearity interactions, and inter-channel cross-talk in WDM systems. Recently, the idea of eigenvalue communications revived as a possibility to encode information for nonlinear-dispersive channels, namely the optical fiber channel [64]. This proposal, simply put, combines high-order soliton solutions with advanced digital communication techniques to achieve high spectral efficiency, and its given the name of nonlinear frequency division multiplexing (NFDM) [64] for its similarity with the orthogonal frequency-division multiplexing (OFDM) technique. The proposal to encode information in the continuous spectrum of NFDM systems was suggested by S. K. Turitsyn *et al* [93]. This is done by modulating the amplitude and the phase of the complex amplitude associated with independent and parallel spectral sub-carriers that are shown to be independent upon propagation in noiseless and lossless fiber transmissions. Furthermore, the continuous spectrum is reduced to the ordinary Fourier transform as the intensity of the potential function is low.

Modelling a NFDM system involves solving the so-called spectral problem associated with the integrable NLSE equation, also known as the Zakharov-Shabat spectral problem (ZSSP). For this purpose, the NFT is used to

mathematically linearize the NLSE by solving the ZSSP. The NFT operation transforms the optical signal to its corresponding nonlinear spectrum, where the evolution along the fiber is linear. The inverse problem on the other hand maps the nonlinear spectral data back into the optical field. This can be achieved by using either the Riemann-Hilbert problem [64] or the Gelfand-Levitan-Marchenko (GLM) equation [93]. Several authors have proposed numerical NFT algorithms with higher orders of accuracy, utilizing the layer-peeling [75], Ablowitz-Ladik integrable discretization [69], forward and central discretizations with first-order Euler method, the fourth-order Runge-Kutta method [76], and the piecewise-constant approximation (PCA) method [103]. In this thesis, the Ablowitz-Ladik discretization and the layer-peeling method of computing the forward NFT and inverse NFT (INFT) of the ZSSP with vanishing boundary condition, respectively, are used.

The organization of this chapter is as follows. The ZSSP is introduced in section 2.3 [85] – [88], providing an independent treatment of the computation of the spectral data associated with a potential function in the ZSSP, their spatial evolution in nonlinear-dispersive channels and the spectral inversion problem. In 2.4, the numerical algorithms associated with computing both forward and inverse problems are formulated. Next, the NFDM transmission architecture for a high-speed long-haul transmission system is addressed in section 2.5. Finally, the analytical formulation is extended to dual-polarization transmissions in section 2.6, considering the Manakov system in the absence of polarization induced fiber impairments (i.e., PMD or PDL).

2.2 Principle of the nonlinear Fourier transform

The most efficient techniques to solve the scalar or vector NLSE requires the use of either the split-step Fourier method (SSFM) or the Volterra series transfer function (VSTF). Under some specific circumstances in which the loss is neglected or mitigated by using distributed amplification, the nonlinear Fourier method provides an elegant method to solve the NLSE. The NLSE (Eq.(1.17)) is an integrable nonlinear PDEs that can be solved using the NFT and INFT. From its beginnings, this method has been known to be the nonlinear analogous of the well-known procedure for solving the initial value problem (IVP) of a linear PDEs by mean of the Fourier transform (FT). The parallelism between the two methods has allowed authors such as M. J. Ablowitz to rename IST as NFT [67]-[69]. This similarity can be

2.2. Principle of the nonlinear Fourier transform

understood as follows.

For example, the evolution of an optical pulse over a purely dispersive fiber channel is ruled by the equation

$$\frac{\partial q(z, \tau)}{\partial z} = -i \frac{\partial^2 q(z, \tau)}{\partial \tau^2} \quad (2.1)$$

given the initial ($\tau = 0$) waveform $q(z = 0, \tau)$ is a known solution at the position $z = 0$. The problem is to find the solution or waveform $q(z, \tau)$ for some specific spatial coordinate z if the initial condition is given. The first step is to map the evolution in the Fourier domain form as

$$\frac{\partial Q(z, \omega)}{\partial z} = i\omega^2 Q(z, \omega), \quad Q(z = 0, \omega) \quad (2.2)$$

where $Q(z, \omega) = \mathcal{F}(q(z, \tau))$ is the FT of the signal $q(z, \tau)$. Then the spatial evolution of $Q(z, \omega)$ for each ω can be obtained by integrating over the spatial coordinate z as

$$Q(z, \omega) = \exp(i\omega^2 z) Q(z = 0, \omega) \quad (2.3)$$

Finally, the inverse FT (IFT) is computed on the spatially evolved transform data $q(z, \tau) = \mathcal{F}^{-1}(Q(z, \omega))$. This is precisely the solution of the IVP.

Such a mechanism is extended to the IVP of a nonlinear PDEs such as the NLSE. Solution of the NLSE using NFT/INFT is evaluated by associating a linear differential operators to the nonlinear PDE. When using the INFT to search for solutions of nonlinear integrable systems, the strategy is similar, and can be summarized by using the following procedure:

1. Search for linear operators associated to the nonlinear PDE that produce the evolution equation $q_z = K(q)$ comparable with the NLSE.
2. Transform the initial value, i.e. the optical signal at the transmitter, from the time domain to the nonlinear spectral domain, where the space evolution is linear, i.e. $\widehat{q}(0, \lambda) = \text{NFT}(q(z = 0, \tau))$.
3. Then calculate the spatial evolution of the transformed spectral data, i.e. $\widehat{q}(0, \lambda) \rightarrow \widehat{q}(z, \lambda)$. Similar to the Fourier transform, the spatial evolution of the spectral data is transformed into a simple phase rotation in the transform domain, which allows the spectral data to propagate as a linear and independent entity.
4. Finally, the inverse transform is applied to obtain the solution in time domain, i.e. $q(z, \tau) = \text{INFT}(\widehat{q}(z, \lambda))$.

The analogy between the two methods is illustrated in Fig.(2.1).

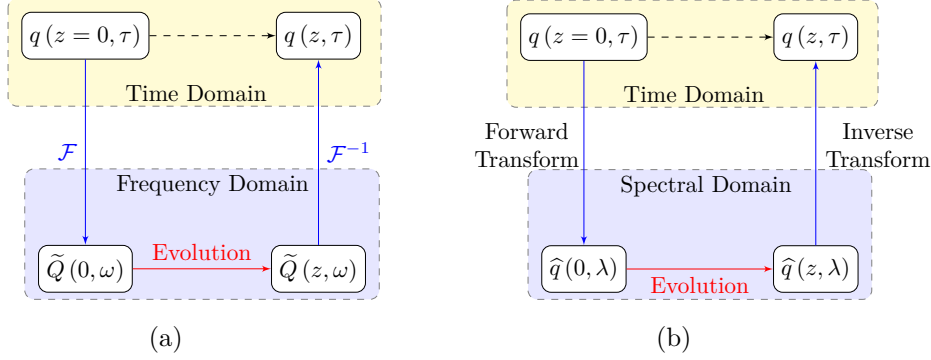


Figure 2.1: Schematic representation of solving the IVP of PDEs in (a), direct and inverse Fourier transform;(b), direct and inverse NFT.

Finding the INFT is a difficult inverse problem. This chapter will address this issue.

2.3 Theory of the nonlinear Fourier transform

The key idea behind the NFT, also known as the scattering theorem, is to search for a linear operator \mathbf{L} whose spectrum (eigenvalues) remains invariant even when the signal $q(z, \tau)$ evolves in space, z , according to some evolution equation $q_z = K(q)$. The operator \mathbf{L} is considered as a diagonalizable matrix and belongs to the family of isospectral (that is, with invariant eigenvalues) operators; it must satisfy the compatibility equation

$$\frac{\partial \mathbf{L}}{\partial z} + [\mathbf{L}, \mathbf{M}] = 0, \quad (2.4)$$

for some linear operator \mathbf{M} . This pair of linear operators, (\mathbf{L}, \mathbf{M}) , that satisfy Eq.(2.4) is called the Lax pairs [66]. This pair was first discovered for the NLSE by Zakharov and Shabat [60], and they are

$$\mathbf{L} = i \begin{bmatrix} \frac{\partial}{\partial \tau} & -q(z, \tau) \\ sq^*(z, \tau) & -\frac{\partial}{\partial \tau} \end{bmatrix}, \quad \mathbf{M} = \begin{bmatrix} i2\lambda^2 - i|q(z, \tau)|^2 & -2\lambda q(z, \tau) - iq_\tau(z, \tau) \\ 2\lambda q^*(z, \tau) - iq_\tau^*(z, \tau) & -i2\lambda^2 + i|q(z, \tau)|^2 \end{bmatrix} \quad (2.5)$$

The systematic method is known as the 'AKNS' formalism, which was developed by Ablowitz, Kaup, Newell, and Segur [67], is used to define the

2.3. Theory of the nonlinear Fourier transform

auxiliary problem associated to NLSE by means of the following pair of linear differential equations

$$\frac{\partial \mathbf{v}}{\partial z} = \mathbf{M} \mathbf{v} \quad (2.6a)$$

$$\frac{\partial \mathbf{v}}{\partial \tau} = \mathbf{P} \mathbf{v} \quad (2.6b)$$

where

$$\mathbf{P} = \begin{bmatrix} -i\lambda & q(z, \tau) \\ -sq^*(z, \tau) & i\lambda \end{bmatrix} \quad (2.7)$$

is the operator of the linear Zakharov-Shabat spectral problem (ZSSP) Eq.(2.6b). Here, $\mathbf{v} = (v_1, v_2)^T \in \mathbb{C}$ are the eigenfunctions of the ZSSP. These matrices, \mathbf{P} and \mathbf{M} , are associated to the eigenvalue λ and the potential function, $q(z, \tau)$ with its complex conjugate, and are the solution of the two coupled nonlinear evolution equations. By cross-differentiating \mathbf{M} and \mathbf{P} and equating the results, the zero-curvature condition

$$\frac{\partial \mathbf{P}}{\partial z} - \frac{\partial \mathbf{M}}{\partial t} + [\mathbf{P}, \mathbf{M}] = 0, \quad (2.8)$$

can be found. Here, $[\mathbf{M}, \mathbf{P}] = \mathbf{M}\mathbf{P} - \mathbf{P}\mathbf{M}$ stand for the commutator operator. The derivation of Eq.(2.8) relies on the assumption that the eigenvalues (λ) are invariant for the evolution equation and a non-vanishing solution ($\mathbf{v} \neq 0$) to NLSE exist.

The NFT of a given fast decaying potential function $q(z, \tau)$, i.e. $|q(z, \tau)| \rightarrow 0$, $|\tau| \rightarrow \infty$ and $q(z, \tau) \in \mathbb{L}^1(\mathbb{R})$, can be obtained by solving the ZSSP (2.6b) for eigenfunctions that have the following asymptotic boundary condition at $\tau \rightarrow \pm\infty$ [68]

$$\Phi(\lambda, \tau) \equiv \begin{pmatrix} \phi_1 \\ \phi_2 \end{pmatrix} \xrightarrow{\tau \rightarrow -\infty} \begin{pmatrix} 1 \\ 0 \end{pmatrix} e^{-i\lambda\tau} \quad \Psi(\lambda, \tau) \equiv \begin{pmatrix} \psi_1 \\ \psi_2 \end{pmatrix} \xrightarrow{\tau \rightarrow +\infty} \begin{pmatrix} 0 \\ 1 \end{pmatrix} e^{i\lambda\tau} \quad (2.9)$$

These functions are known as Jost solutions. The Wronskian of the Jost solutions, $W(\phi, \bar{\phi}) = W(\bar{\psi}, \psi) = 1$, is non-zero, and the pair of vectors $\{\phi, \bar{\phi}\}$ and $\{\psi, \bar{\psi}\}$ are linearly independent. Therefore, they can be chosen to form the basis for the ZSSP (2.6b). Hence the solution set $\{\phi, \bar{\phi}\}$ can be written as a linear combination of $\{\psi, \bar{\psi}\}$

$$\phi(\lambda, \tau) = a(\lambda) \bar{\psi}(\lambda, \tau) + b(\lambda) \psi(\lambda, \tau) \quad (2.10a)$$

$$\bar{\phi}(\lambda^*, \tau) = -\bar{b}(\lambda^*) \bar{\psi}(\lambda^*, \tau) + \bar{a}(\lambda^*) \psi(\lambda^*, \tau). \quad (2.10b)$$

The coefficients $\{a, b, \bar{a}, \bar{b}\}(\lambda)$ are known as the Jost scattering coefficients and defined as

$$a(\lambda) = \lim_{\tau \rightarrow +\infty} \phi_1(\lambda, \tau) e^{i\lambda\tau}, \quad b(\lambda) = \lim_{\tau \rightarrow +\infty} \phi_2(\lambda, \tau) e^{-i\lambda\tau} \quad (2.11)$$

These coefficients are a time-independent and complex-valued function. The NFT of a vanishing potential $q(z, \tau)$ is defined as

$$\widehat{q}(\lambda) = \frac{b(\lambda)}{a(\lambda)}, \quad \lambda \in \mathbb{R}. \quad (2.12)$$

$$\widetilde{q}(\lambda_j) = \frac{b(\lambda_j)}{a'(\lambda_j)}, \quad \lambda_j \in \mathbb{C}^+, \quad (2.13)$$

where $\widehat{q}(\lambda)$ and $\widetilde{q}(\lambda_j)$ represent the **continuous spectrum** (also called the **reflection coefficient**) and the **discrete spectrum** (also called the **norming constant**) that corresponds to the *radiation (a non-solitonic)* and the *solitonic* component of the potential function, respectively. Here, the $\lambda_j, j = 1, \dots, N$ are the eigenvalues of $\widetilde{q}(\lambda_j)$ in the upper-half of the complex plane where $a(\lambda_j) = 0$, and $a'(\lambda_j)$ denotes the derivative $da(\lambda)/d\lambda|_{\lambda=\lambda_j}$. The NFT operation thus involves a mapping of the initial field value, $q(0, \tau)$, onto a set of a scattering data (amplitude) $\{\widehat{q}(\lambda), \widetilde{q}(\lambda_j)\}$ for the continuous and discrete spectral parameters $\{\lambda \in \mathbb{R}, \lambda_j \in \mathbb{C}^+\}$ [60].

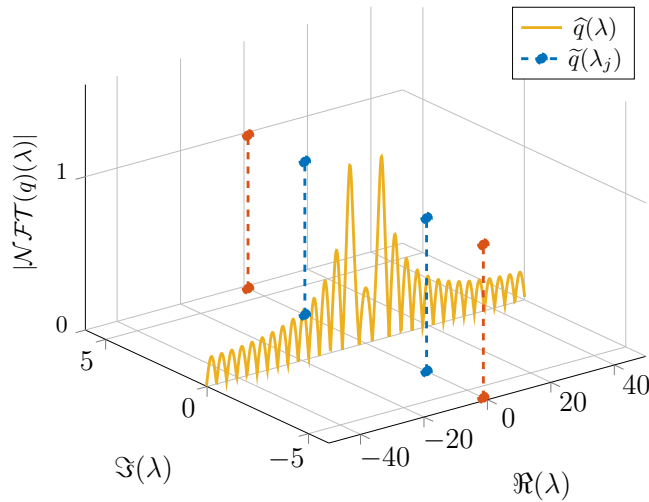


Figure 2.2: nonlinear spectrum of a potential function with vanishing boundary condition.

2.3. Theory of the nonlinear Fourier transform

Fig.2.2 illustrates the nonlinear spectrum of a potential function $q(0, t)$ with a vanishing boundary condition. The nonlinear spectrum contains some isolated discrete spectrum (red and blue) and one continuous spectrum (orange). The continuous spectrum lies on the real axis, for sufficiently vanishing boundary grants the existence of a bounded solution for the ZSSP. The discrete spectrum corresponds to a particular solution of the NLSE that preserve the spectral shape upon fiber propagation thanks to balancing act between dispersion and nonlinear effects.

Eq.2.10 can be written as projection operation as

$$\begin{pmatrix} \phi(\lambda, \tau) \\ \bar{\phi}(\lambda^*, \tau) \end{pmatrix} = \underbrace{\begin{pmatrix} a(\lambda) & b(\lambda) \\ -b^*(\lambda^*) & a^*(\lambda^*) \end{pmatrix}}_{\mathbf{S}} \begin{pmatrix} \bar{\psi}(\lambda^*, \tau) \\ \psi(\lambda, \tau) \end{pmatrix} \quad (2.14)$$

where the matrix \mathbf{S} is known as the scattering matrix and contains the continuous nonlinear spectrum coefficients. The continuous spectrum-also referred to as reflection coefficient-can be interpreted using the scattering problem as shown in Fig.2.3. The solution for the ZSSP is evaluated by applying a field $\phi(-\infty, \tau) = (1, 0)^T e^{-i\lambda\tau}$ at $t = -\infty$ where the potential q is absent. The field propagate forward in time according to the ZSSP formalization, interacts with the potential function (the scattering potential) at finite value of t , and subsequently allowed to propagate toward $t = +\infty$ where the potential function absent once again. At $t = +\infty$ the field $\phi(+\infty, \tau)$ is measured and gives information about the scattering potential seen from a distance [64]. The scattering matrix entries can be used as a data carrier in fiber optic communication.

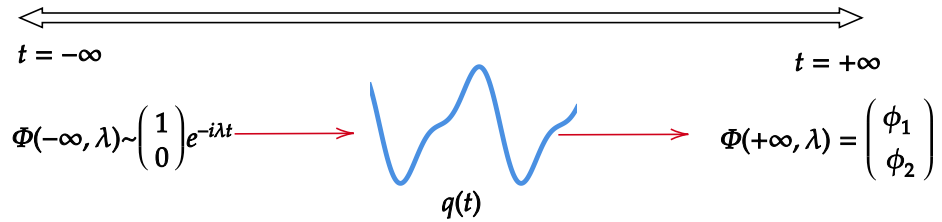


Figure 2.3: Scattering problem associated with the continuous spectrum.

The discrete and continuous spectrum representation of the waveform $q(z, \tau)$ is advantageous, since the magnitude of the nonlinear spectra at each eigenvalue λ does not change with z upon propagation if fiber loss and noise is

neglected. Moreover, the phase of the scattering coefficients obeys a simple linear evolution, so that the spectral amplitude computed at any given spatial-coordinate can be simply inverted in order to compensate for the action of the channel on the spectral amplitudes. In the absence of noise and loss, the spectral amplitude at the transmitter can be computed from the received spectrum by using the following relations

$$\widehat{q}(\lambda, z) = \widehat{q}(\lambda, 0) e^{i4s\lambda^2 z}, \quad \lambda \in \mathbb{R} \quad (2.15a)$$

$$\widetilde{q}(\lambda_j, z) = \widetilde{q}(\lambda_j, 0) e^{i4s\lambda_j^2 z}, \quad \lambda_j \in \mathbb{C}^+, \quad i = 1, \dots, N \quad (2.15b)$$

$$\lambda(z) = \lambda(0), \quad \lambda \in \mathbb{R} \quad (2.15c)$$

$$\lambda_j(z) = \lambda_j(0), \quad \lambda_j \in \mathbb{C}^+ \quad i = 1, \dots, N \quad (2.15d)$$

Thus by associating the NLSE with the ZSSP, it is possible to reduce the spatial evolution of the spectral data to just a phase change in the transform domain. The channel transfer function is, therefore, modeled as an all-pass filter, and reads as

$$H(\lambda, z) = e^{i4s\lambda^2 z}. \quad (2.16)$$

Similar to the ordinary Fourier transform that maps a linear convolution channel into a number of independent linear scalar channels, the NFT method transforms the nonlinear-dispersive channel into a simple multiplicative channel, thus revealing the hidden "linearity" in the NLSE (1.17) [60] – [64].

The inverse NFT (INFT), which is commonly known as the IST, address the issue of reconstructing the potential function $q(\tau)$ from the continuous spectral amplitude $(\widehat{q}(\lambda), \widetilde{q}(\lambda_j))$. As the spatial evolution of the scattering data is known, it possible to reconstruct the potential function. The potential function reconstruction from the scattering data can be achieved either by solving the Riemann-Hilbert (RH) or the Gelfand-Levitan-Marchenko (GLM) integral equation when the spectrum is purely continuous [64], [68]. However, due to the computational complexity needed to directly solve the GLM integral equation, in this thesis, the RH-approach is used due to its efficiency [71]–[74]. The potential function at time τ can be reconstructed by using the following expression [64]

$$\begin{aligned} q(z, \tau) &= \text{IST}(\widehat{q}(\lambda), \widetilde{q}(\lambda_j)) \\ &= \left(2i \sum_{j=1}^N \widetilde{q}(\lambda_j) e^{2i\lambda_j \tau} V_2^1(\lambda_j, \tau) - \frac{1}{\pi} \int_{-\infty}^{\infty} \widehat{q}(\lambda) e^{2i\lambda \tau} V_2^1(\lambda, \tau) d\lambda \right)^* \end{aligned} \quad (2.17)$$

where $V_2^1(\cdot, \tau)$ is the scaled version of the Jost-solution (for a detailed derivation refer to the appendix of [64]).

2.4. Numerical method for computing the NFT

In general, the forward and inverse NFT methods may be viewed as a nonlinear generalization of the linear Fourier transform. Indeed, when the modulus of the potential function (signal) $q(z, \tau)$ approaches to zero asymptotically, the continuous spectrum (the reflection coefficient) converges to the linear Fourier transform of a signal. This justifies the use of the term inverse/nonlinear Fourier transform (INFT/NFT) to represent the inverse and direct scattering transform (IST/DST) in recent publications. The spectral parameter, $\lambda \in \mathbb{R}$, thus takes the role of a frequency and is often called the *nonlinear frequency*.

2.4 Numerical method for computing the NFT

Numerical simulation plays a significant role in validating the algorithm used to implement the forward- and inverse NFT, especially in the development of eigenvalue communications. In the past, several discretization and integral methods have been proposed to find the nonlinear spectrum associated with the ZSSP. The main part of numerically solving the ZSSP is to replace the differential problem, ∂_t , with a finite-difference approximation which can be Forward-Euler, central-difference, Runge-Kutta, etc [64]. Some of these methods are robust and computationally sound. Numerical algorithms for the NFT computation includes methods such as the Ablowitz-Ladik discretization [69] and the Boffetta-Osborne method [70]. To compute the continuous spectrum of a signal, the AL-discretization procedure described in [75] was used, where the implementation procedure is shown in Fig.(2.7).

The goal of the AL-discretization method is to calculate the continuous nonlinear spectrum $\widehat{q}(\lambda)$ from the given space-time-domain potential function $q(z, \tau)$. This process involves computing the scattering coefficients $a(\lambda)$ and $b(\lambda)$ associated with the potential function $q(t)$, i.e., it solves the ZSSP associated with NLSE. Meanwhile, the layer peeling (LP) remains one of the most efficient methods to invert the nonlinear spectrum (compute the INFT of a potential profile). The LP method is a two-step process as shown in Fig.(2.8). The first step consists in computing the NFT coefficients $a(\lambda)$ and $b(\lambda)$ from the nonlinear spectral amplitude $\widehat{q}(\lambda)$, and the second step consists in retrieving the potential function from the scattering coefficients. Applying the LP method to the AL-discretization was proposed by Wahls and Poor [77] – [80], and it has been shown to be an effective method to compute the potential function from the scattering coefficients. In this iterative methods, the computational error accumulates as the number of iterative increases [64], [75].

2.4.1 Numerical Forward NFT using the AL-discretization method

This study make use of the AL-discretization method to calculate the NFT [64] or, equivalently, to solve the ZSSP. Let us assume that $q(t) \in L^1(\mathbb{R})$ with support set $[\tau_1, \tau_2]$ and consider a uniform grid with $\tau[k] = \tau_1 + k\epsilon$, $k = 0, 1, \dots, N-1$, $\tau_1 = -\frac{\tau}{2}$, $\epsilon = \frac{\tau}{N}$ where N is the number of temporal sample size. Similarly, the nonlinear frequency uniform grid is defined as $\lambda[k] = -\frac{L}{2} + k\mu$, $k = 0, 1, \dots, N-1$ and $L = \frac{\pi}{\epsilon}$.

To calculate the nonlinear spectrum using the AL-discretization method, the procedure described in [64] was used. For every eigenvalue λ , the ZSSP is solved in iterative way during each time-step,

$$\frac{\phi[k+1] - \phi[k]}{\epsilon} = \begin{pmatrix} -i\lambda[k] & q[k] \\ -sq^*[k] & i\lambda[k] \end{pmatrix} \phi[k] = T[k]\phi[k] \quad (2.18)$$

which can be simplified as

$$\begin{aligned} \phi[k+1] &= \begin{pmatrix} 1 - i\epsilon\lambda[k] & q[k] \\ -sq^*[k] & 1 + i\epsilon\lambda[k] \end{pmatrix} \phi[k] \\ &= (I_{2 \times 2} + \epsilon T[k]) \phi[k] \end{aligned} \quad (2.19)$$

The AL-discretization method introduce discretization of NLSE by replacing $1 \pm i\epsilon\lambda$ by $e^{\pm i\lambda\epsilon}$ for small ϵ , and let $Q[k] = \epsilon q[k]$ and $z = e^{-i2\lambda\epsilon}$, thus Eq.2.19 can be written as

$$\phi[k+1, z] = c_k \begin{pmatrix} z^{\frac{1}{2}} & Q[k] \\ -sQ^*[k] & z^{-\frac{1}{2}} \end{pmatrix} \phi[k, z], \quad \phi[0] = \begin{pmatrix} 1 \\ 0 \end{pmatrix} z^{\frac{k_0}{2}}, k_0 = \frac{\tau_1}{\epsilon} \quad (2.20)$$

where $c_k = \frac{1}{\sqrt{1-s|Q[k]|^2}}$ is the normalization constant and $\phi[0]$ is the boundary condition for $\phi(\lambda, \tau)$. The NFT coefficients are obtained from the end point solution as

$$a[k, z] = z^{-\frac{k_0+k}{2}} \phi_1[k], \quad b[k, z] = z^{\frac{k_0+k}{2}} \phi_2[k] \quad (2.21)$$

which can be written in a scaled format as

$$A[k, z] = a[k, z] = z^{-\frac{k_0+k}{2}} \phi_1[k], \quad B[k, z] = z^{-(k_0+k)+\frac{1}{2}} b[k, z] \quad (2.22)$$

The forward iteration of the scaled AL-discretization method is given by

$$\begin{aligned} \begin{pmatrix} A[k+1, z] \\ B[k+1, z] \end{pmatrix} &= c_k \begin{pmatrix} 1 & Q[k]z^{-1} \\ -sQ^*[k] & z^{-1} \end{pmatrix} \begin{pmatrix} A[k, z] \\ B[k, z] \end{pmatrix} \\ \begin{pmatrix} A[0, z] \\ B[0, z] \end{pmatrix} &= \begin{pmatrix} 1 \\ 0 \end{pmatrix}, \quad 0 \leq k \leq N-1 \end{aligned} \quad (2.23)$$

2.4. Numerical method for computing the NFT

Instead of updating the scaled NFT coefficients in Eq.2.23 for each z , one can update the coefficients of the z -transform transform polynomial as

$$\begin{aligned} A[k, z] &= \sum_{m=0}^{M-1} A_m[k] z^{-m} \\ B[k, z] &= \sum_{m=0}^{M-1} B_m[k] z^{-m} \end{aligned} \quad (2.24)$$

where M stand for non-zero coefficients and $A_m[k]$ and $B_m[k]$ are calculated as

$$A_m[k] = \frac{1}{L} \int_{L_1}^{L_2} A[k, e^{-i2\lambda\tau[k]}] e^{-i2m\epsilon\lambda} d\lambda \quad (2.25)$$

Finally, the continuous nonlinear spectrum is evaluated as ratio of the scattering coefficients $\widehat{q}(\lambda) = b(\lambda)/a(\lambda)$. The flow chart in the Fig.2.7 illustrates the steps of the AL-discretization routine in computing the continuous spectrum of a vanishing potential.

2.4.2 Numerical Inverse NFT using the LP method

The LP method is used for fast and accurate computation of the inverse transform based on the RH-problem. In the LP method, the NFT coefficients are computed from the continuous nonlinear spectral amplitude using the relation

$$|a(\lambda)| = \frac{1}{\sqrt{1 - s|\widehat{q}(\lambda)|^2}} \quad (2.26)$$

following the unimodularity condition

$$|a(\lambda)|^2 - s|b(\lambda)|^2 = 1, \quad \lambda \in \mathbb{R} \quad (2.27)$$

The amplitude $|a(\lambda)|$ and $\arg(a(\lambda))$ are related by the Hilbert transform

$$\arg(a(\lambda)) = \mathbb{H}(\log |a(\lambda)|), \quad \lambda \in \mathbb{R} \quad (2.28)$$

where \mathbb{H} is the Hilbert transform and \arg is the principal value of the phase. As a result, $b(\lambda) = \widehat{q}(\lambda)/a(\lambda)$.

The recovered potential function waveform at a discrete time $\tau[k] = k\epsilon$ is given by

$$Q^*[k] = s \lim_{z \rightarrow \infty} z^{-(k+k_0)+\frac{1}{2}} \frac{b[k+1, z]}{a[k+1, z]} \quad (2.29)$$

after which dividing by ϵ and taking the complex conjugate gives the potential function $q(t)$. The numerical implementation of the LP method is summarized in the Fig.2.8.

For example, consider a rectangular pulse

$$q(t) = \begin{cases} A, & t \in [\tau_1, \tau_2] \\ 0, & \text{otherwise} \end{cases}$$

where A is the amplitude of the pulse. Let $T = \tau_2 - \tau_1$ and $T' = \tau_1 + \tau_2$.

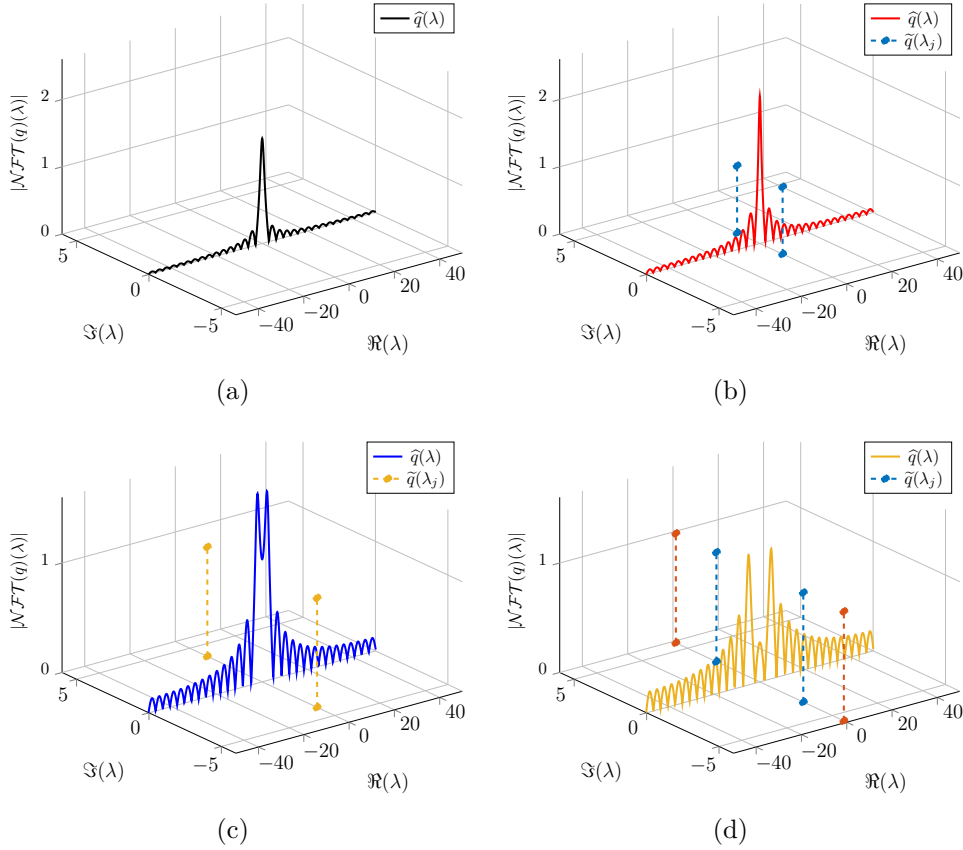


Figure 2.4: Illustration of the NFT of a simple un-modulated rectangular pulse. The absolute value of the continuous spectrum of a rectangular pulse $q(t) = A * \text{rect}(t)$, (a), evolves from a simple sinc-type for (b) $A=1$, to more complicated shapes for (c) $A=4$, and (d) $A=6$.

Fig.(2.4) illustrate the spectral amplitude for $T = 64$ and various value of A . For small amplitude, A , the continuous spectrum becomes the ordinary Fourier transform (FT) of $q(t)$ as shown in Fig.2.4(a), i.e., the sinc-pulse, given by:

$$\widehat{q}(\lambda) = \mathcal{F}\{q(t)\} = -A \cdot T e^{-i2\pi f T'} \text{sinc}(2Tf), \quad \lambda = 2\pi f$$

2.4. Numerical method for computing the NFT

as solitons are absent. For higher amplitudes, the continuous spectrum deviation from the ordinary FT, i.e., from a simple sinc-shape to more complicated shapes, as discrete spectrum or solitons emerge [64] as illustrated in the Fig.(2.4(b) – 2.4(d)).

The computational complexity of the forward and inverse scattering transform operation poses a significant challenge both in numerical simulations and experimental validations. In the past few years, the numerical complexity of computing the NFT of a signal has been reduced quite significantly by using a fast polynomial arithmetic approach [77]. The INFT computation algorithm, however, becomes a computational bottleneck. The LP-method that is applied to compute the time-domain signal requires that the spectral amplitude to remain quite small within the discretization step so that they can be combined together. Otherwise, the computational error will propagate between discretization steps and increase exponentially to corrupt the signal. For this reason, for spectral amplitude values that approach the unit value, i.e. $\widehat{q}(\lambda) \rightarrow 1$, a large number of temporal samples and higher spectral resolution (i.e. smaller step in λ or $d\lambda$) are required for a better accuracy in the forward and in the inverse spectral problem, respectively.

In order to test the relative error in the numerical computation of the continuous spectrum of the potential function using both the NFT and the INFT, digital back-propagation based on NFT (NFT-DBP) is used as proposed in [81]. As illustrated in Fig.(2.5), a pure un-modulated Gaussian optical signal $q(z=0, \tau) = q_0 = A \cdot \exp(-0.5 \cdot \tau^2)$ from the transmitter propagates in the fiber according to the NLSE. Here, the pulse duration is set to $T = 64$, and, both the time and nonlinear frequency λ uniform grid is defined over a sample size of $N = 2^{15}$ points. Then, the NFT algorithm is used to compute the continuous spectrum ($\widehat{q}(z, \lambda) = \widehat{q}_z$) from the received signal ($q(z, \tau) = q_z$). The spatial evolution of the signal given by the analytic expression of (2.15) is inverted using a one-tap channel equalizer. Here, the interplay of both CD and nonlinearity on the signal is removed in the nonlinear frequency domain. Finally, the time domain signal $\widetilde{q}(z, \tau)$ is computed from the equalized spectral domain signal $\widehat{q}_{eq}(z, \lambda)$ via the INFT. For nonlinear spectrum with a norm close to one, a larger number of step are required to accurately compute the INFT of the given pulse. The numerical error in the computation of the nonlinear spectrum using the NFT-INFT procedures is quantified by the relative (percentage) error, and reads as

$$Error [\%] = \frac{\text{norm}(\widehat{q}(0, \lambda) - \widehat{q}_{eq}(z, \lambda), 2)}{\sqrt{\text{norm}(\widehat{q}(0, \lambda)) \cdot \text{norm}(\widehat{q}_{eq}(z, \lambda))}} \quad (2.30)$$

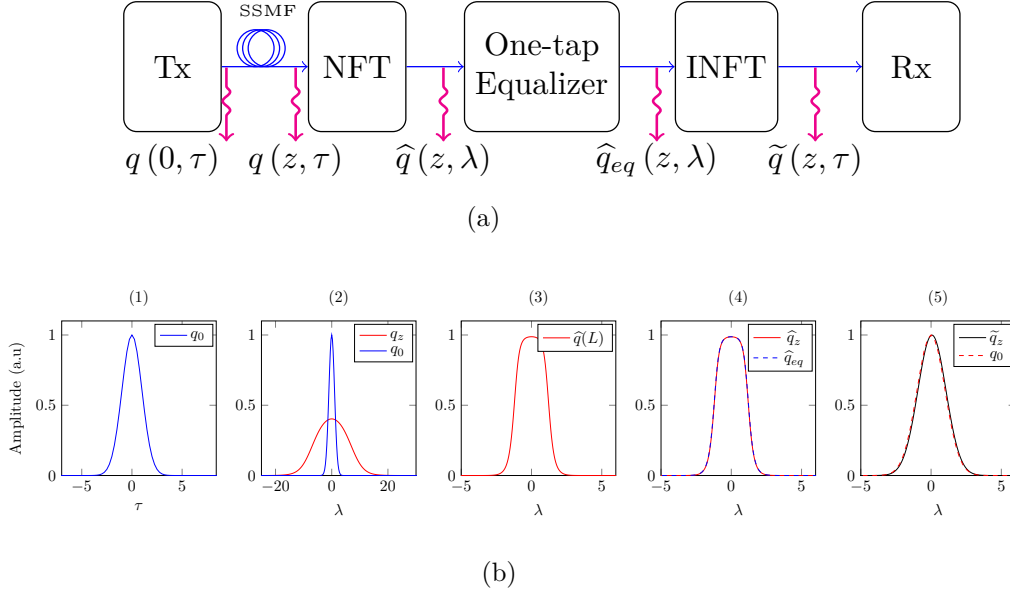


Figure 2.5: A schematic diagram of digital back-propagation based on nonlinear Fourier transform (a). The NFT-DBP block diagram, where the time domain signal q_0 (b.1) propagates inside a nonlinear-dispersive fiber channel so that the interplay of dispersion and nonlinearity results a broadened pulse q_z , (b.2). The channel effect is removed in the spectral domain $\hat{q}_z \rightarrow \hat{q}_{eq}$ (b.3-4) before the time domain information signal \tilde{q}_z is recovered using the INFT (b.5).

Following the NFT based DBP configuration in Fig.(2.5), the numerical accuracy analysis of the NFT-INFT computation for different signal shapes of the potential function is demonstrated in Fig.(2.6). In this simulation different potential functions such as secant-hyperbolic, Gaussian, rectangular and sinc-function are considered as possible candidates of the NFT basis functions. The relative error is measured as a function of the number of floating point operations (flops), which represent the number of sample points, used in the NLSE discretization. Signals which are well-shaped and decay exponentially demonstrate a lower error value as the number of points is increased when compared with pulse shapes with either a sharp and oscillatory decaying behavior. Here, the author point out that the LP-method is only adequate to extract the potential function from nonlinear spectral amplitude norm upto 0.9999 because of the large increase in computational error with the iterative matrix inversion procedure.

Current communication methods were ones developed for the linear channels. This design approaches are flawed when dealing with the fiber channels

2.4. Numerical method for computing the NFT

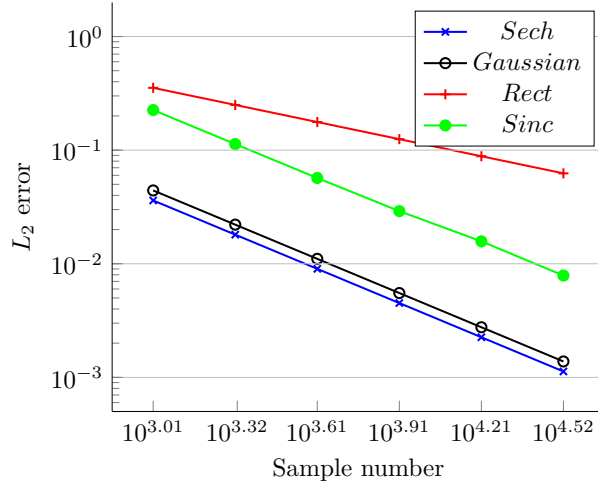


Figure 2.6: The numerical accuracy of the NFT-INFT algorithm as function of the number of samples for a different signal types.

in the sense that the fiber nonlinear effect was neglected in the such design. In a typical quadrature amplitude modulation (QAM), for example, the transmitted signal in absence of noise is

$$q(t) = \sum_k c_k g(t - kT) \quad (2.31)$$

such that the set of time-shifted pulses

$$\{g(t - kT) : k = \dots, -2, -1, 0, 1, 2, \dots\}$$

are used as an orthonormal basis to perform a projection of user symbols. Here, each pulse $g(t - kT)$ (for a choice of k -subcarriers) essentially defines a channel which do not interfere with each other. As a general principle, a channel capacity crunch occurs if the basis function used for communication is not compatible with the channel. Therefore, choosing NFT basis function that satisfies the Nyquist criterion for zero ICI and ISI is key for a real-world application of NFT based communication systems. The next section investigates the concepts of Nonlinear Frequency Division Multiplexed (NFDM) system.

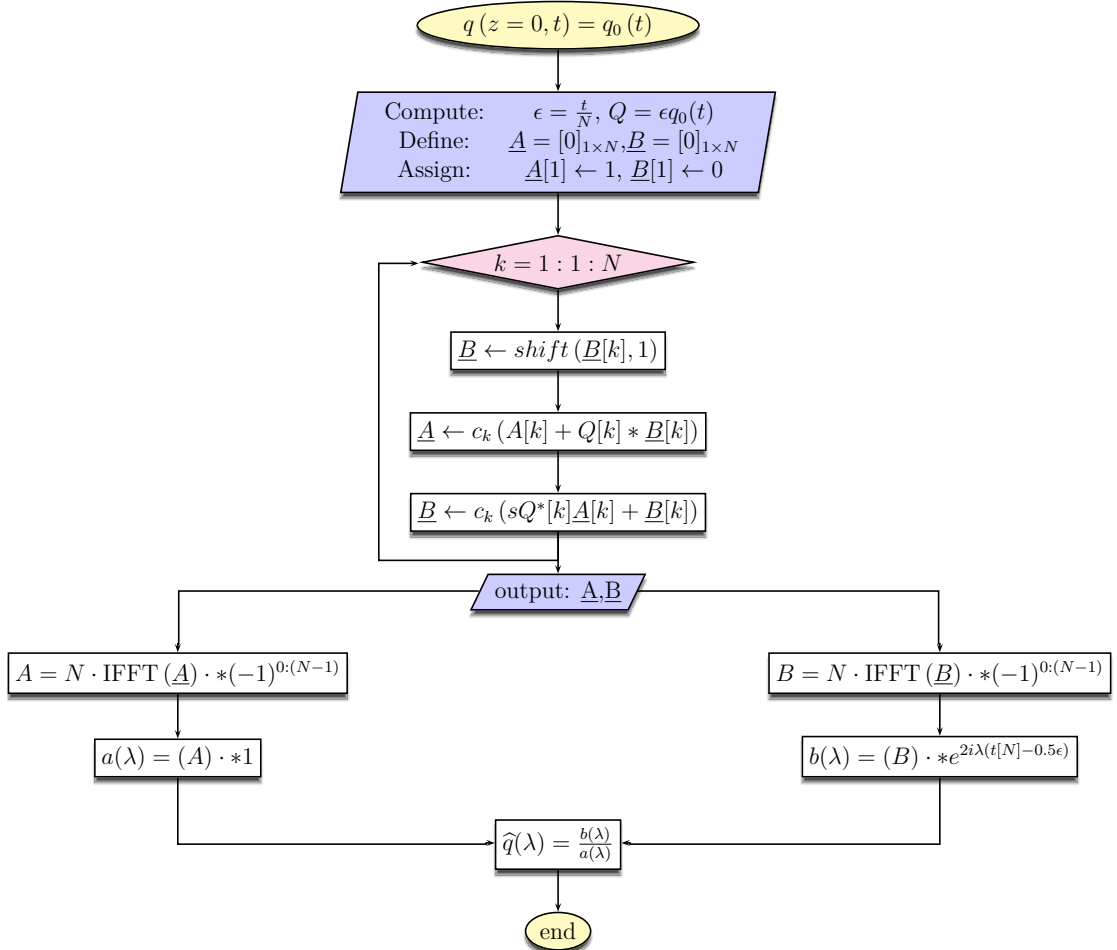


Figure 2.7: Flow chart of NFFT algorithm implementation (after [75]).

2.4. Numerical method for computing the NFT

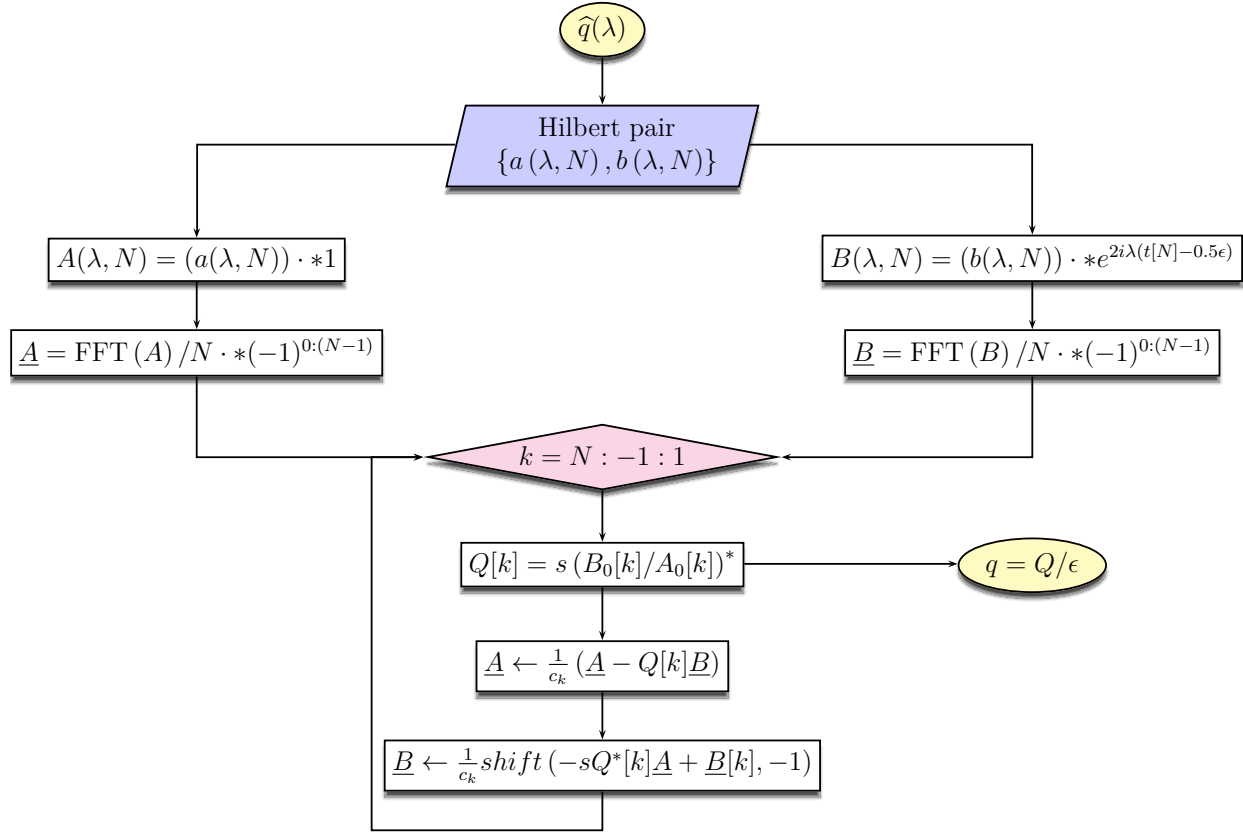


Figure 2.8: Flow chart of INFT algorithm implementation (after [75]).

Symbol	Description
$\{a(\lambda), b(\lambda)\}$	NFT coefficients
$\{A(\lambda), B(\lambda)\}$	Scaled NFT coefficients
$\{\underline{A}(\lambda), \underline{B}(\lambda)\}$	The Fourier transform of the scaled coefficients
$shift(\cdot)$	Matlab®shift operation

Table 2.1: Parameters in NFT/INFT algorithms.

2.5 Nonlinear Frequency Division Multiplexed Systems

The approach of optical transmission system design based on NFT, which takes into account the fiber nonlinearity as an essential element rather than considering it as a destructive effect, has a promising potential to overcome nonlinear distortions. Similar to the linear Fourier transform that translates dispersive effects into a simple phase rotation in the frequency domain, the NFT leads to a nonlinear spectrum which has a non-interfering and linear evolution, as it couples both dispersion and nonlinearity effects in the nonlinear spectral domain. This suggests that information can be encoded on the nonlinear spectrum directly, such that it can be restored at the receiver avoiding any nonlinear interference due to propagation. This scheme is referred to as nonlinear frequency division multiplexing (NFDM) [64]. The idea is similar to the OFDM in the linear domain, in which interference is avoided in frequency domain by properly allocating transmission modes (eigenmodes) with the help of Fourier transform (FT). Let us consider a transmitted signal over a distance z over linear channel. The input and output signal is related through the channel transfer function, $h(z, t)$, such that

$$y(z, t) = y(0, t) \otimes h(z, t)$$

where the input signal is $x(t) = y(0, t)$. Invoke FT on $y(0, t)$ and $y(z, t)$ results

$$Y(z, f) = Y(0, f) \cdot H(z, f)$$

where $Y = FT(y)$ and $H = FT(h)$. As a results, the channel is "diagonalised" into multiple independent channels (each indexed by a different frequency). In the NFDM, the FT is replaced by the NFT and the signal input-and-output relation in the nonlinear spectral domain becomes linear scalar multiplication, which significantly "diagonalised" the nonlinear fiber channel [64]. The linear evolution of the nonlinear spectral data can be demonstrated by comparing a nonlinear signal evolution in temporal and transform domain. Let us consider the evolution signal $q(t)$ inside a nonlinear dispersive channel. In the temporal domain, the action of dispersion and nonlinearity force the input $q(z = 0, t)$ -to-output $q(z = L, t)$ mapping to be a complex process as shown in Fig.2.9(a). However, for integrable channel characterized by the Lax pair (\mathbf{L}, \mathbf{M}) , the output of the channel $q(z = L, t)$ is given as a Lax convolution between the input $q(z = 0, t)$ and the action of the integrable system $(\mathbf{L}, \mathbf{M}; L)$, i.e., $q(L, t) = q(0, t) \otimes (\mathbf{L}, \mathbf{M}; L)$. In the NFT domain, the Lax convolution is translated into a simple multiplication operation such that

2.5. Nonlinear Frequency Division Multiplexed Systems

in the absence of noise the input and the output spectrum are related by

$$\hat{q}(L, \lambda) = \hat{q}(0, \lambda) \cdot H(L, \lambda)$$

where $H(L, \lambda)$ is an all-pass like filter which allow a linear evolution of spectral data as shown in the Fig.2.9(b).

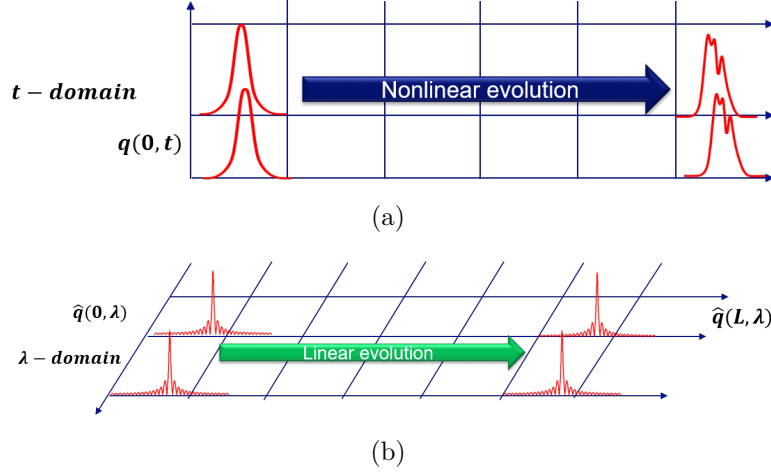


Figure 2.9: Illustration of nonlinear pulse evolution in a nonlinear dispersive channel in, (a) temporal domain where the input-output mapping become complex; and (b) nonlinear frequency domain where the nonlinear spectral amplitude evolve in linear and trivial manner.

These property motivates to directly modulate the continuous and discrete part of the nonlinear spectrum either separately or jointly. An alternative approach to modulated the continuous part of the nonlinear spectrum, called nonlinear inverse synthesis (NIS), uses the INFT and NFT DSP blocks as extra layers in a traditional OFDM based transmission architecture as shown in Fig.(2.10) [93]. Here, the linear spectrum from OFDM block is mapped to the continuous part of the nonlinear spectrum before being transmitted over the fiber in the nonlinear regime. In this thesis, however, the NIS system considered as a special case of NFDM.

For the NFDM NIS-system shown in Fig.(2.10), at the transmitter, the incoming serial information bits $\{b_k\}$ are converted to parallel by a serial-to-parallel (S/P) converter and mapped according to the high-level modulation techniques such as QPSK or QAM. After that, the subcarriers are modulated in the digital domain by using the inverse fast Fourier transform (IFFT)

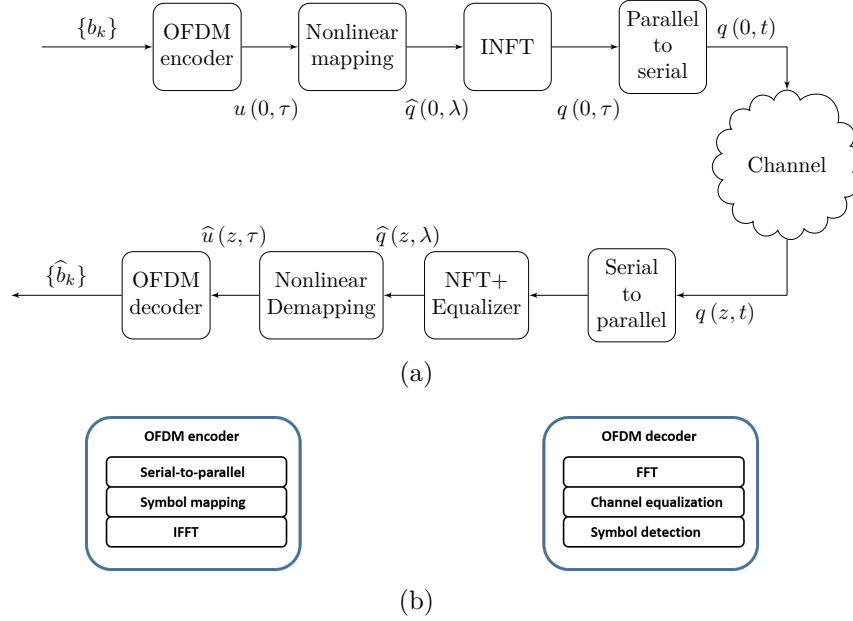


Figure 2.10: The architecture of NFDM transmission system (a) and (b) the corresponding DSP.

module. The output of the IFFT, $u(0, \tau)$, represents the linear spectrum, i.e. the OFDM signal, which is then mapped on to the continuous nonlinear spectrum $\hat{q}(0, \lambda)$. The time domain signal $q(0, \tau)$ is generated by taking the INFT according to Eq.(2.17). The output of the INFT block can be seen as a superposition of all modulated nonlinear frequency subcarriers. Since the NFT/INFT computation is done in the normalized domain, the signal must be denormalized according to Eq.(1.18). Then, the subcarriers are converted to a serial signal $q(0, t)$ by a parallel-to-serial (P/S) converter and transmitted through amplified multi-span optical fiber links.

At end of the transmission line, the receiver processes the modulated signal to restore the transmitted data. At the receiver side, the digital signal is normalized and arranged into parallel signal using the serial-to-parallel (S/P) converter before the spectral of $q(z, t)$ is recovered by the NFT operation, $\hat{q}(z, \lambda) = \text{NFT}(\hat{q}(z, \lambda))$, and a simple one-tap equalizer $H = \exp(-4i\lambda^2 L)$ is used to reverse the action of dispersion and nonlinearity on the nonlinear spectral amplitude. Each equalization output is de-mapped into the nonlinear spectral domain $\hat{u}(z, \tau)$, demodulated by the FFT operation, and then a residual channel equalization is applied before being decoded by the symbol decoding block. The numerical implementation and experimental validation of NFDM system is revisited in details in the next chapter.

2.6 NFT of polarization division multiplexed signal

Increasing the capacity and spectral efficiency (SE) per unit bandwidth of optical communication systems is one of the ultimate goal of researchers and engineers. It was possible to achieve this goal on the basis of technologies such as advanced modulation techniques, coherent detection, wavelength division multiplexing, polarization multiplexing, and complex digital signal processors. The polarization-division-multiplexing (PDM) scheme, which supports two independent data channels on a single wavelength with orthogonal polarization states, has become a standard in most state-of-the-art optical fiber communication systems. As a result, it has been proposed [82] – [83] and experimentally demonstrated [84] that the INFT can be applied to a PDM system if the optical field propagation follows the Manakov equation [43]. Manakov first recognized that Eq.(1.26) is an integrable system and the corresponding scattering transform is developed as follows.

The integrable Manakov equation (1.26) can be associated to a linear system of ordinary differential equations (ODEs) that depend on a spectral parameter λ [85],

$$\frac{\partial \mathbf{v}}{\partial \tau} = (i\lambda\sigma + \mathbf{Q})v \quad (2.32a)$$

$$\frac{\partial \mathbf{v}}{\partial z} = [2i\lambda^2\sigma + 2\lambda\mathbf{Q} + i\sigma(\mathbf{Q}^2 - \mathbf{Q}_\tau)]v \quad (2.32b)$$

where $\mathbf{v}(\lambda, z, \tau)$ is 3×3 eigenfunction matrix, σ is a constant diagonal matrix given by

$$\sigma = \begin{pmatrix} 1 & 0 & 0 \\ 0 & 1 & 0 \\ 0 & 0 & 1 \end{pmatrix}, \quad (2.33)$$

and $\mathbf{Q} = \mathbf{Q}(z, \tau)$ and the time derivative $\mathbf{Q}_t = \mathbf{Q}_\tau(z, \tau)$ are 3×3 matrix potential functions which read as

$$\mathbf{Q}(z, \tau) = \begin{pmatrix} 0 & q_x & q_y \\ -sq_x^* & 0 & 0 \\ -sq_y^* & 0 & 0 \end{pmatrix} \quad \mathbf{Q}_z(z, \tau) = \begin{pmatrix} 0 & q_{x,\tau} & q_{y,\tau} \\ -sq_{x,\tau}^* & 0 & 0 \\ -sq_{y,\tau}^* & 0 & 0 \end{pmatrix} \quad (2.34)$$

The system of equations, Eq.(2.32a) is known as the Lax pair or scattering problem associated with the Manakov system. The Lax pair of these

equations is found through the modified ZSSP given by [43]:

$$\mathbf{L} = i \begin{bmatrix} \frac{\partial}{\partial \tau} & -q_x & -q_y \\ sq_x^* & -\frac{\partial}{\partial \tau} & 0 \\ sq_y^* & 0 & -\frac{\partial}{\partial \tau} \end{bmatrix}, \quad \mathbf{M} = \begin{bmatrix} 2i\lambda^2 + si|\mathbf{q}|^2 & -2\lambda q_x - iq_{x,\tau} & -2\lambda q_y - iq_{y,\tau} \\ -s2\lambda q_x^* + siq_{x,\tau}^* & -i2\lambda^2 - i|q_x|^2 & -siq_y q_x^* \\ -s2\lambda q_y^* + siq_{y,\tau}^* & -siq_1 q_y^* & -2i\lambda^2 - is|q_y|^2 \end{bmatrix} \quad (2.35)$$

To compute the spectral data associated with a given potential \mathbf{q} , the so-called Jost-solution matrix Φ and Ψ for Eq.(2.32a) defined by their corresponding asymptotic behaviour:

$$\Phi(\lambda, \tau) \equiv \begin{pmatrix} \phi_1 \\ \phi_2 \\ \phi_3 \end{pmatrix} \xrightarrow{\tau \rightarrow -\infty} \begin{pmatrix} 1 & 0 & 0 \\ 0 & 1 & 0 \\ 0 & 0 & 1 \end{pmatrix} e^{-i\lambda\tau} \quad \Psi(\lambda, \tau) \equiv \begin{pmatrix} \psi_1 \\ \psi_2 \\ \psi_3 \end{pmatrix} \xrightarrow{\tau \rightarrow +\infty} \begin{pmatrix} 0 & 0 & 1 \\ 1 & 0 & 0 \\ 0 & 1 & 0 \end{pmatrix} e^{-i\lambda\tau} \quad (2.36)$$

The set of these solution matrices $\{\Phi, \Psi\}(\lambda, \tau)$ defines a linearly independent set which spans the solutions space of (2.32a). One can expand Φ in the basis of Ψ :

$$\phi_1(\lambda, t) = \psi_1(\lambda, \tau) b_1(\lambda) + \psi_2(\lambda, \tau) b_2(\lambda) + \psi_3(\lambda, \tau) a(\lambda) \quad (2.37)$$

where $a(\lambda)$, $b_1(\lambda)$ and $b_2(\lambda)$ are nonlinear spectral coefficients, with

$$a(\lambda) = \lim_{\tau \rightarrow +\infty} \phi_1(\lambda, t\tau) e^{i\lambda\tau}, \quad b_1(\lambda) = \lim_{\tau \rightarrow +\infty} \phi_2(\lambda, \tau) e^{-i\lambda\tau}, \quad b_2(\lambda) = \lim_{\tau \rightarrow +\infty} \phi_3(\lambda, \tau) e^{-i\lambda\tau} \quad (2.38)$$

These coefficients are used to define the DST/NFT of the potential $\mathbf{q}(\tau)$ as

$$\text{NFT}(q_p(\tau))(\lambda) = \begin{cases} \widehat{q}_p(\lambda) = \frac{b_p(\lambda)}{a(\lambda)}, & \lambda \in \mathbb{R}, \\ \widetilde{q}_p(\lambda) = \frac{b_p(\lambda_j)}{a'(\lambda_j)}, & \lambda_j \in \mathbb{C}^+, \quad p = x, y; j = 1, \dots, N \end{cases} \quad (2.39)$$

where $a'(\lambda_j) = da(\lambda)/d\lambda|_{\lambda=\lambda_j}$ and the set of N discrete eigenvalues λ_j corresponds to the zeros of $a(\lambda_j)$ in the upper-half complex plane, i.e. $a(\lambda_j) = 0, \forall \lambda_j \in \mathbb{C}^+$. In the absence of noise, these time-independent nonlinear spectral amplitudes, $\{\widehat{\mathbf{q}} = \widehat{q}_{x,y}(\lambda), \widetilde{\mathbf{q}} = \widetilde{q}_{x,y}(\lambda)\}$, have a linear spatial evolution:

$$\widehat{\mathbf{q}}(z, \lambda) = \widehat{q}_p(z=0, \lambda) e^{-i4s\lambda^2 z}, \quad \widetilde{\mathbf{q}}(z, \lambda_j) = \widetilde{q}(z=0, \lambda_j) e^{-i4s\lambda_j^2 z}, \quad (2.40)$$

where the channel transfer function is modeled as the all-pass filter $H(z, \lambda) = \exp(-i4s\lambda^2 z)$. The nonlinear spectral coefficients must satisfy the unimodularity condition

$$|a(\lambda)|^2 - s(|b_1(\lambda)|^2 + |b_2(\lambda)|^2) = 1. \quad (2.41)$$

2.6. NFT of polarization division multiplexed signal

The mathematical procedure for reconstructing the potential function is quite similar to the single polarization case, but depends on the modified Manakov-Zakharov-Shabat spectral problem (MZSSP), Eq.(2.32a). The numerical approaches of forward and inverse NFT used to compute the continuous nonlinear spectrum are based on the Ablowitz-Ladik (AL) discretization and discrete layer peeling (DLP)-methods, respectively [83]. Similar to the single-polarization case, the accuracy of the AL and the DLP methods is demonstrated in Fig.(2.11) for two displaced Gaussian nonlinear spectral amplitudes $\hat{\mathbf{q}} = [\hat{q}_x, \hat{q}_y]$ with standard deviation $\sqrt{2}$, a time window size $T = 64$, and a fixed number of 2048 samples in the defocusing regime. Fig.(2.11) demonstrates a deviation in spectral amplitude of coupled shifted pulse when it is computed directly by numerically solving the Manakov equation, and after NFT-INFT joint processing, unlike the single polarization case illustrated in Fig.(2.5). Such deviation is attributed to the reduced accuracy of the NFT-INFT algorithm at higher signal powers. As a result, higher sampling rates are required to generate the NFT and INFT of a signal. Moreover, compared to single-polarization, the Manakov NFT requires twice the number of samples for a similar accuracy.

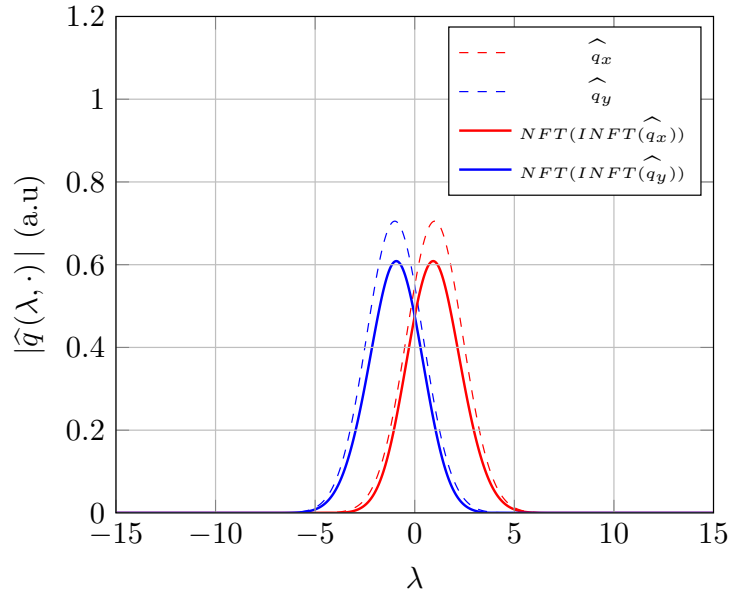


Figure 2.11: The numerical accuracy of a dual-polarization NFT-INFT pair for a dual polarization signal which given by a shifted Gaussian shaped initial spectrum $\hat{\mathbf{q}} = [\hat{q}_x, \hat{q}_y]$ and $\text{NFT}(\text{INFT}(\hat{\mathbf{q}}))$ at high power. For a fixed sample size, the accuracy of algorithm decreases at large amplitudes (after [83]).

2.7 Summary

This chapter provided an overview of analytical and numerical methods to compute the continuous nonlinear spectrum of the potential function, including the spatial evolution and the inverse problem. Neglecting the effect of PMD, the spectral problem associated to the Manakov equation is presented. Finally, the concept of nonlinear frequency division multiplexing was introduced briefly, and will be used in the remainder of this thesis as the underlying architecture for an experimental validation and further numerical investigations.

2.7. Summary

Chapter 3

Experimental demonstration of a NFDM based optical transmission system

“ Experimenters are the shock troops of science. ”

Max Planck,

3.1 Introduction

A well-known technique for high-speed and long-haul optical fiber transmissions is orthogonal frequency division multiplexing (OFDM) [89]. In OFDM, the overlapping orthogonal property of sub-carriers allows for an increase of the spectral efficiency [90]. However, at relatively high transmission power, the nonlinearity in the fiber causes nonlinear mixing between sub-carriers, limiting the maximum achievable transmission capacity and reach [92]. As mentioned in section 2.5, the NFDM transmission based on the NFT technique has been proposed as a potential approach to increase the OSNR value, and ultimately an increase the spectral efficiency [64],[93]. In recent years, either the continuous or the discrete spectrum have been considered as data encoding mechanisms. Several experimental demonstrations of NFDM have been reported: these experiments employed transmission fibers operating either in the anomalous or in the normal dispersion regime, respectively. In the former case, the nonlinear spectrum consists of continuous and discrete components, which can be separately [94] – [96],[100] or jointly [101]

3.1. Introduction

modulated. In the latter case, there is no discrete spectrum and only the continuous spectrum can be modulated [102]. NFDM systems underwent a rapid progress, going from 4 Gbps transmission rate using 2-eigenvalues [104] to 65 Gbps systems using both continuous and discrete spectrum [101]. The current record transmission burst-rate for NFDM is 125 Gbps, which results in effective bit-rate of 25 Gbps, with a spectral efficiency of 2.3 bit/s/Hz using the continuous spectrum [105].

Modulation	Gross data rate	L [km]	Year	Ref.
QPSK	10.7 Gb/s	7344	2016	U. Aston [94]
16-QAM	25.6 Gb/s	1632	2016	Nokia Bell Labs [95]
32-QAM	125 Gb/s	1464	2017	Nokia Bell Labs [105]
64-QAM	150 Gb/s	976	2017	Nokia Bell Labs [101]
7-soliton QPSK	7 Gb/s	1440	2017	Nokia Bell Labs [97]
2-soliton QPSK	4 Gb/s	640	2018	Nokia Bell Labs [99]
2-soliton QPSK*	8 Gb/s	373.5	2015	DTU [84]
1-soliton 16-APSK	24 Gb/s	1000	2016	PolyU [100]

Table 3.1: Experimental demonstration of a continuous and discrete spectrum based optical NFDM transmission systems. (* Dual-polarization NFDM transmission systems.)

The Table 3.1 shows the gross data rate, transmission reach and modulation formats for different experimental validations of optical NFDM transmission using either the continuous or the discrete spectrum. In the continuous spectrum, the QPSK modulation format has a very small gross data rate when compared with the highest order modulation formats, i.e. 16, 32, 64QAMs. Similarly, the gross data rate of the discrete (soliton) methods can be increased by adding more eigenvalues and using higher-order modulation formats.

The method used by Le *et al.* in [105] is considered as a bench mark. In [105], the authors have experimentally demonstrated NFDM transmission using 64 orthogonal sub-carriers modulated with 32QAM format using the continuous spectrum over 1464 km. This demonstration has achieved a record net data rate of 32 Gb/s and a performance gain of 0.8 dB as indicated in Fig.(3.1(a)). Another experimental performance of NFDM transmissions using a discrete spectrum modulation in a dual-polarization configuration is shown in Fig.(3.1(b)). In this case, a gross data rate of 8 Gb/s over 373.5 km was achieved.

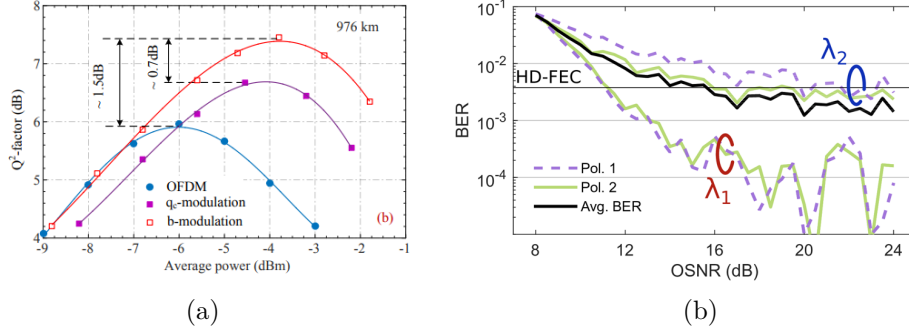


Figure 3.1: Illustration of NFDM optical transmissions. (a) A Q-factor as function of the launch power when modulating the continuous spectrum [105]; (b) BER performance as a function of OSNR for discrete spectrum modulation in a dual-polarization configuration [84].

In this thesis, the numerical implementation and an experimental validation of NFDM transmission system is carried out in the normal dispersion regime. This choice is justified due to the fact that in normal dispersion regime only the continuous spectrum DoF can be modulated as the soliton components are assumed to be absent. Therefore, this work can be considered as original in its own right as most experiments are done by using the SSMFs (i.e. anomalous dispersion fibers). Furthermore, this is the first experiment intended to demonstrate the dual polarization NFDM transmission system following the theoretical work done in [83].

This chapter begins by briefly reviewing the description of the NFDM transmission scheme, by drawing a parallelism with OFDM systems in section 3.2. Next, the experimental NFDM signal generation is presented in section 3.3. In section 3.4 and 3.5 the functional DSP module for the transmitter and receiver are discussed in great details. Finally, section 3.6 presents a detailed account of the experimental validation of NFDM transmission by using the continuous spectrum in both the normal and the anomalous dispersion regime, with both a single- and a dual-polarization configuration, respectively.

3.2 Brief review of the coherent optical OFDM transmissions

OFDM is one of the most popular among a broad class of multi-carrier modulation (MCM) schemes, here, instead of transmitting data using a single high-rate carrier, one transmits in parallel on a number of low-rate different subcarriers [106]. As a result, each low-rate subcarrier sees a channel with a flat-frequency response, resulting in a longer symbol period (T_s) for the same total data rate, and better tolerance to ISI. Therefore, the channel impairment equalization is simplified. The key feature in OFDM is the use of orthogonal subcarriers, which is achieved through the inverse fast Fourier transform (IFFT). This enables a precise and computationally efficient way of generating orthogonal subcarriers in OFDM.

The spectrum of OFDM is obtained from the sum of N sinusoidal impulses of the same duration, but with different frequencies. These sub-carriers satisfy the orthogonality condition in the frequency domain as illustrated in Fig.(3.2(a)): each sub-carriers spectrum must have a null point at all frequencies of other subcarriers used to form the OFDM symbols. The orthogonality condition is given by $\Delta f = 1/T_s$ where Δf represents the sub-carriers frequency spacing. Although the spectra of individual sub-carriers overlap, they can be demodulated without inter-carrier interference (ICI). The sub-carrier packing in OFDM can fill the bandwidth close to the Nyquist bandwidth, as illustrated in Fig.(3.2(b)), which eventually increases the spectral efficiency. However, due to fiber dispersion, the sub-carriers may lose their orthogonality. In order to cope with dispersive channel effects such as CD and PMD, a guard interval (GI) in the time domain is used between two consecutive OFDM symbols [107]. The guard interval is implemented as a zero-padded (ZP) symbol. In order to be effective, the guard interval duration must exceed the maximum delay spread of the channel. Such a design is known as the burst-mode OFDM system, and as mentioned in section 2.5, it is the preferable modulation format for NFDM-based optical transmission schemes [93].

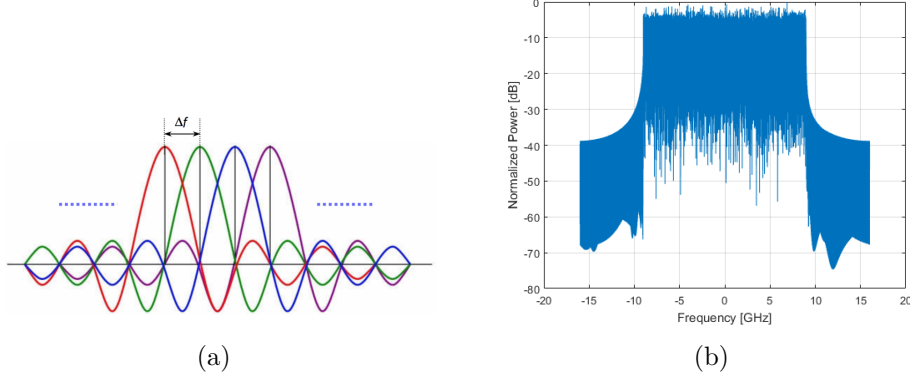


Figure 3.2: Principle of OFDM and its spectrum. (a) Theoretical overlapping and orthogonal subcarriers, (b) experimental Nyquist bandwidth of OFDM.

3.3 Experimental generation, transmission and detection of NFDM signal

In its most general form, an optical fiber transmission system is composed of a transmitter, an optical channel containing amplified fiber spans, other optical components, and a receiver. The optical transmission system based on NFDM involves a linear modulation, linear evolution of the nonlinear spectral amplitude over the channel, and linear demodulation [96]. Consequently, a linear transformation between the transmitter and the receiver chain is key for a proper NFDM implementation. However, both linear and nonlinear distortions may arise from the optical modulator, the electrical and optical front-end amplifiers, and the non-flat gain-loss profile of fiber link, which make it hard to achieve full linearity in a real world transmission system.

Fig.(3.3) shows a typical experimental schematic design of a DSP based NFDM optical transmission system. The offline transmitter DSP block is shown in the inset of Fig.(3.3). It is quite trivial to draw a parallelism between the coherent NFDM transmitter and the burst-mode CO-OFDM implementation. Here, the additional DSP layers required by the NFDM system are indicated in yellow blocks [94].

3.3.1 NFDM signal generation

At the transmitter side, user information bits are encoded using a square-16QAM modulation format and parallelized before being processed by the IFFT block. After that, a guard interval is inserted to the time domain

3.3. Experimental generation, transmission and detection of NFDM signal

NFDM symbols to prevent inter-symbol interference (ISI) due to channel dispersion. The FFT of the time domain signal is encoded onto the nonlinear continuous spectrum by the forward mapping stage before the time domain complex signal is computed via the INFT. The temporal domain signal then denormalized according to Eq.(1.18) and serialized by the parallel-to-serial (P/S) converter. The in-phase (I) and quadrature (Q) digital signals are converted to analog signals using a digital-to-analog converter (DAC), and the aliasing signal is filtered out by the low-pass filter (LPF). The output analog signal is up-converted to the optical signal via the IQ modulator (i.e. Mach-Zehnder IQ modulator). The power of the optical envelope at the output of the modulator may be boosted to the desired power level by using an erbium doped fiber amplifier (EDFA) [111] before its launching into an optical channel.

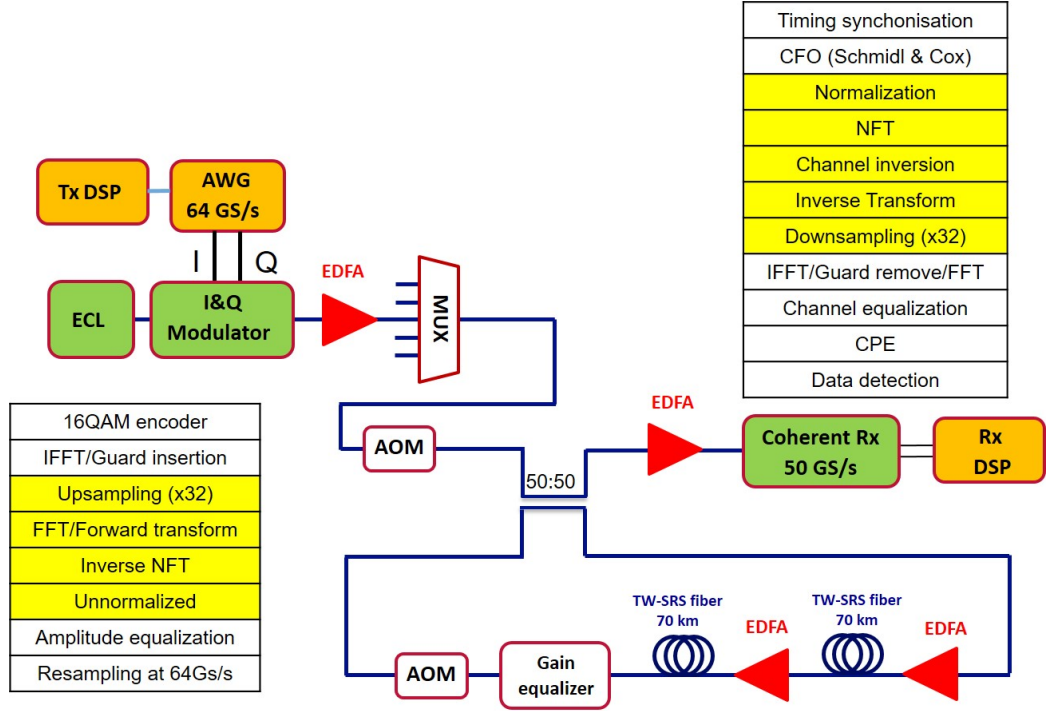


Figure 3.3: The experimental setup block diagram and the associated offline DSP chain at the TX and RX.

3.3.2 Optical modulator

The basic functionality of the optical transmitter is to convert an electrical complex waveform into an optical pulse for its transmission through the

optical link. For typical high-speed long-haul systems, this process is achieved by the modulation the optical carrier of the laser source with an external optical modulator as shown in Fig. (3.4(a)), which is driven by an electrical baseband signal containing the data to be transmitted [109],[110]. Hence, the output of the MZM takes the form

$$E_{out}(t) = E_0 \cdot \cos\left(\pi \frac{V_1 - V_2}{2V_\pi}\right) \cdot \exp\left(i\pi \frac{V_1 + V_2}{2V_\pi}\right), \quad (3.1)$$

where E_0 and E_{out} are the fields at the input and output of the modulator respectively, V_1 and V_2 are the voltages applied to the arms, and V_π is the half-wave voltage of the modulator. Such configuration of the MZM can be used to generate modulation formats encoding transmitted bits on the field amplitude (e.g. on-off keying (OOK) and amplitude shift keying (ASK)) or phase (e.g. binary phase shift keying (BPSK)).

In order to utilize quadrature components of the optical carrier for data transmission, an optical IQ-modulator is required. As a result, for high spectral efficiency, all possible physical degrees of freedom, i.e. amplitude, phase, and polarization, of light should be modulated [108],[110]. Unlike a single MZM that modulates the phase of the optical carrier along one axis (either I or Q-phase), in order to exploit the functionality of an IQ-modulator, two MZMs are required, as shown in Fig.(3.4(b)). After signal pre-equalization to combat any amplitude distortion in the transmitter, the complex waveform in the digital domain is separated into its real (I) and imaginary (Q) components, and transformed into an analog electrical signal by means of DACs and LPFs. As shown in Fig.(3.4(b)), an optical IQ-modulator consisting in two nested Mach-Zehnder modulators (MZMs) with a $\pi/2$ shift between their outputs. After modulation, the two MZM output waves are recombined to form a total optical field that reads as

$$E_T = E_{out,I} + \exp(i\pi/2) \cdot E_{out,Q}. \quad (3.2)$$

For high-speed long-haul transmissions, the electro-optical bandwidth, the insertion loss, the carrier extinction ratio, and the modulator linearity are the most important properties of the MZM. A modulation format with a higher spectral efficiency requires a MZM to operate in the linear regime, so that the distances between constellation point are preserved in the optical domain. However, the MZM has a cosine nonlinear response and it introduces a significant distortion to the NFDM signal. In order to achieve a linear operation regime, the NFDM signal should be pre-distorted at the transmitter.

3.3. Experimental generation, transmission and detection of NFDM signal

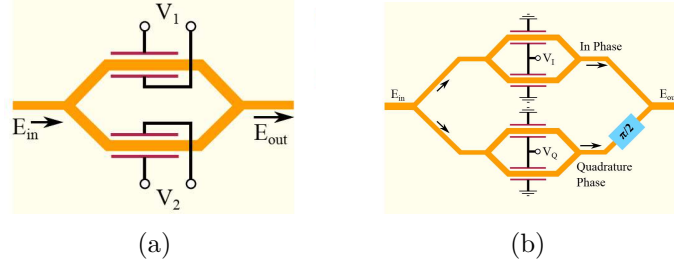


Figure 3.4: Structure of (a) a Mach-Zehnder-Modulator (MZM), (b) an IQ-modulator made of two MZMs and a $\pi/2$ phase shifter.

3.3.3 Amplified Optical fiber transmission link

A multi-span fiber link is emulated with a recirculation loop, which consists of single mode fiber and EDFA (with a pre-defined NF of 5.5 dB). During fiber propagation, the NFDM signal will be impaired by fiber linear and nonlinear effects, as well as by amplified spontaneous emission (ASE) noise introduced at each EDFA stage and accumulates over the transmission link. Therefore, a bandpass optical filter (OBPF) is used to eliminate the out-of-band ASE noise. Throughout this thesis, the transmission link does not include any in-line dispersion and nonlinearity compensation modules, thus the fiber linear and nonlinear impairments are left uncompensated.

3.3.4 Coherent receiver

The fundamental functionality of a coherent receiver is transforming the incoming optical field into an electrical waveform [112]. In a coherent detection configuration, frequency locking of the free-running local oscillator (LO) and the optical carrier is a difficult task, thus coherent receivers are designed in an intradyne configuration [113]. As a result, the transmitter and receiver laser are free to have a drift in both frequency and/or phase by small but arbitrary shift. In this thesis, the intradyne configuration is used, which allows for the mixing of the continuous-wave free-running LO, from the same ECL that generated the optical carrier, with the electric field of the modulated optical signal. Such detection provides access to the complete physical degrees of freedom of the optical field, i.e. amplitude, phase, and polarization. As a result, coherent detection enables the use of high-SE modulation formats, where the information is encoded jointly on the amplitude, phase and polarization state of the optical field. The schematic of a typical polarization diversity front-end coherent receiver is shown in Fig.(3.5).

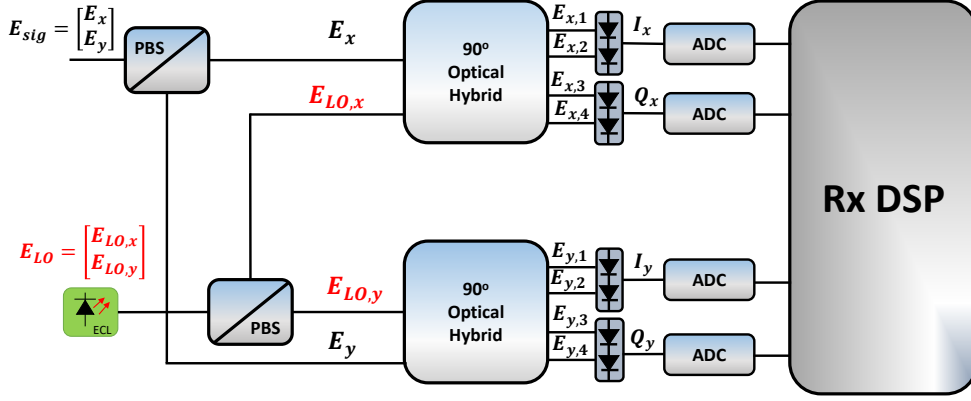


Figure 3.5: Polarization diversity intradyne receiver.

At the receiver input, two polarization beam splitters (PBSs) split both the signal and LO into two orthogonal polarizations. In order to recover the in-phase and in-quadrature components of the signal, each polarization enters into the 90° optical hybrid, which allows for the coherent mixing of the LO tuned at the carrier frequency, i.e. $\omega_{LO} = \omega_c$, and the incident x- and y-polarization components of the optical signal. The output of each optical hybrid is connected to four pairs of high-speed balanced photodiodes (PDs) that separate the IQ-components of each polarization, and at the same time suppress the DC component corresponding to direct detection. The IQ-components of the photocurrent of each polarization is proportional to the field values, which are defined as

$$\begin{bmatrix} I_x \\ Q_x \end{bmatrix} \propto \begin{bmatrix} \Re\{E_x E_{LO,x}^*\} \\ \Im\{E_x E_{LO,x}^*\} \end{bmatrix} \quad \begin{bmatrix} I_y \\ Q_y \end{bmatrix} \propto \begin{bmatrix} \Re\{E_y E_{LO,y}^*\} \\ \Im\{E_y E_{LO,y}^*\} \end{bmatrix} \quad (3.3)$$

where $E_{x\&y}$ and $E_{LO,x\&y}$ represent the x and y polarization components of the signal and LO, respectively. The differential electrical currents from each pair of PDs are converted to electrical signals by four linear trans-impedance amplifiers. Following signal conversion, the photo-currents are sampled by analog-to-digital converters (ADCs). Subsequently, the sampled data are processed by RX-DSP blocks to decode the transmitted data.

3.4. NFDM digital transmitter design

3.3.5 NFDM signal detection

The optical signal out of the loop is detected by using a polarization diversity coherent receiver, comprising a polarization beam splitter, a local oscillator, two hybrids, and four balanced detectors which are described in section 3.3.4. After the down-conversion of the optical signal, each detected RF tributaries (I_x , Q_x , I_y , and Q_y) signals are digitized by using ADCs. After a successful NFT window synchronization and carrier frequency offset (CFO) compensation, the NFDM signal is normalized and the nonlinear continuous spectrum is obtained by using the NFT. The interplay between nonlinearity and dispersion can be removed in the NFT domain using a 1-tap channel equalizer. Then, once the nonlinear spectrum is reverse mapped, the complex waveform is recovered by using IFFT operation and the guard interval is removed in the temporal domain. The resulting signal is down-sampled in the Fourier domain and residual channel estimation is done by using the zero-forcing 1-tap equalization per subcarrier per symbol. Finally, the laser phase noise estimation and compensation, carrier recovery, demodulation, and BER estimation are done before data detection.

In the following sections, all the blocks of the DSP chain are described in details.

3.4 NFDM digital transmitter design

In this section, the basic NFDM transmitter DSP block is presented.

3.4.1 Modulation and symbol mapping

At the transmitter, the linear feedback shift register (LFSR) method is used to generate a pseudo random bit sequence (PRBS), $\{b_k\}$, with a bit duration $T_b = 0.5$ ns. These bits are encoded using the desired modulation format and parallelized before the subcarrier assignment is done. A constellation alphabet with M -points can carry a maximum of $n = \log_2(M)$ bits per symbol. This maximum number of bits per symbol is achieved when the constellation points are uniformly distributed. The most used modulation formats for coherent optical communication systems are quadrature phase shift keying (QPSK) and M -level quadrature amplitude modulation (M -level QAM) [108],[110]. The average power associated with such constellations is given by:

$$P = \frac{1}{M} \sum_{k=1}^M |c_k|^2 \quad (3.4)$$

where c_k is the symbol sequence drawn from 16-QAM constellations. In this thesis, a transmission reach of ~ 2000 km was investigated, thus the 16QAM modulation format based on a Gray mapping architecture is proposed as the M-level modulation scheme.

3.4.2 Baseband signal generation

After performing bit modulation, the modulated symbols are encoded over orthogonal subcarriers in the nonlinear Fourier domain. The signal waveform can be written as [75]:

$$U(0, \lambda) = \sum_{l=1}^{N_{sym}} \sum_{k=1}^{N_{sc}} c_k^l G(\lambda - kW_0) \quad (3.5)$$

where N_{sc} is the total number of nonlinear subcarriers, N_{sym} is the total number of symbols, c_k^l corresponds to the l^{th} -symbol transmitted over the k^{th} -subcarrier at the frequency $\lambda = kW_0$ chosen from the constellation symbol set, $W_0 = \Delta f$ is the subcarrier spacing, and $G(\lambda)$ is an orthogonal basis function. For a given symbol-rate, the basis function that minimizes the signal bandwidth is the *sinc* function, as its Fourier transform is a rectangular function which is commonly used in linear multiplexing, i.e., in OFDM. The multiplexing in Eq.(3.5) can, therefore, be considered as a nonlinear analog of linear multiplexing. The time domain equivalent signal is generated by using the IFFT (\mathcal{F}^{-1}) of Eq.(3.5) as [75]

$$u(0, \tau) = \mathcal{F}^{-1}(U(0, \lambda)) = \sum_{l=1}^{N_{sc}} \sum_{k=1}^{N_{sym}} \widehat{c}_k^l g_k(\tau) e^{i2\pi kW_0 \tau} \quad (3.6)$$

where τ is interpreted as a virtual time (normalized time), $g(\tau) = \mathcal{F}^{-1}(G(\lambda))$ is the orthogonal basis in the temporal domain, \widehat{c}_k^l is the IFFT of the transmitted symbols, and $W_0 = 1/T_s$, where T_s is the symbol duration.

3.4.3 Guard interval insertion

The continuous part of the nonlinear spectrum of the potential function is dispersive, which suggest that signal broadening occurs during its evolution. As a result, the NFDM signal is designed in the burst mode, which is similar to the CO-OFDM signal, i.e. the neighboring NFDM/OFDM symbols are separated with a zero guard interval in the temporal domain in order to prevent inter-symbol interference upon a propagation. The length of the guard interval (GI) introduced between symbols must be longer than the

3.4. NFDM digital transmitter design

channel memory as a result of accumulated dispersion in the optical link due to both the CD and PMD [101], and it is defined as

$$T_{ch} = 2\pi B\beta_2 L + 3 \cdot D_p \sqrt{L} \quad (3.7)$$

where β_2 , D_p , and L represent the second order dispersion coefficient, the PMD coefficient, and the transmission length of the fiber, respectively. The total duration of the dispersed waveform T_{DW} in the quasi-linear regime, i.e. whenever nonlinear effects are negligible, is given by $T_{DW} = T_s + T_{ch}$.

Fig.(3.6) shows the NFDM signal broadening in a pure dispersive channel. Here, a channel memory of $T_{ch} = 2.8$ ns (red) is introduced on each side of the initial symbol with a duration of $T_s = 2$ ns (blue), resulting in a total symbol duration of $\mathcal{T} = T_s + GI > T_s + T_{ch} = 8$ ns (red) including the guard interval.

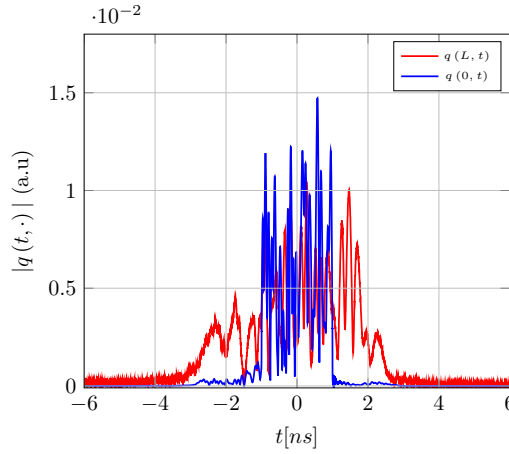


Figure 3.6: Signal broadening due to dispersion in NFDM transmission over 1600 km fiber link.

3.4.4 Forward mapping

The forward nonlinear mapping DSP layer is a unique process for NFDM transmissions. The continuous spectrum in the nonlinear Fourier domain is mapped from the complex-plane into the z -plane [75] according to the following transformation:

$$\widehat{q}(0, \lambda) = \sqrt{s - se^{-\frac{s}{2}|U'(0, \lambda)|}} e^{i \angle U'(0, \lambda)} \quad (3.8)$$

where $U'(0, \lambda)$ is the FFT of $u'(0, \tau)$, which is the burst-mode temporal domain signal and can be considered as the nonlinear equivalent of the burst-mode CO-OFDM time domain signal. Finally, the nonlinear Fourier spectral signal is fed to the INFT block to convert it to the time domain complex waveform $q(\tau)$ as

$$q(0, \tau) = \text{INFT}(\widehat{q}(0, \lambda)). \quad (3.9)$$

The INFT of the signal is computed numerically by using the layer-peeling algorithm shown in Fig.(2.8).

3.4.5 Signal denormalization

The complex waveform $q(\tau)$ at the output of the INFT block is computed in the normalized domain, in order to remove any channel dependency. However, the signal $A(t)$ that is going to be optically modulated and launched into the fiber link must be denormalized according to eq.(1.18) in order to match the real channel parameters [75], [64]. This denormalized signal, must satisfy the energy conservation condition given by Parseval identity

$$\mathbf{E} = \sum_{k,l} |c_k^l|^2 = \int_{-\infty}^{\infty} |q(t)|^2 dt = -\frac{s}{\pi} \int_{-\infty}^{\infty} \log(1 - s|\widehat{q}(\lambda)|^2) d\lambda, \quad (3.10)$$

which guarantees the magnitude of the continuous spectrum to be less than one, i.e. $|\widehat{q}| < 1$ [75], in the defocusing regime, following Eq.(3.8). The power of the signal is then computed as

$$P = \frac{\mathbf{E}}{\mathcal{T}} = \frac{1}{\mathcal{T}} \int_{-\infty}^{\infty} |q(t)|^2 dt, \quad (3.11)$$

where \mathcal{T} is the period of the NFDM signal. The shape of the complex time-domain INFT signal is directly dependent of the input signal power as indicated in Eq.(3.10). In Fig.(3.7), different output signals of the INFT block with different input signal power levels are compared by using a numerical simulation. At the launch input power of -7 dBm, the INFT approximates the IFFT and the signal resembles the burst-mode OFDM signal. As the input launch power increased, i.e. from -4 dBm to -2 dBm, the signal energy is leaking toward the decaying tail, which leads to a pronounced longer tail. This decaying tail puts a large strain on the effective number of bits (ENOBs) requirement of the analog-to-digital converter (DAC) at the transmitter front-end [94]. Here, the effective burst power of the signal is evaluated while taking the energy of the tail into consideration.

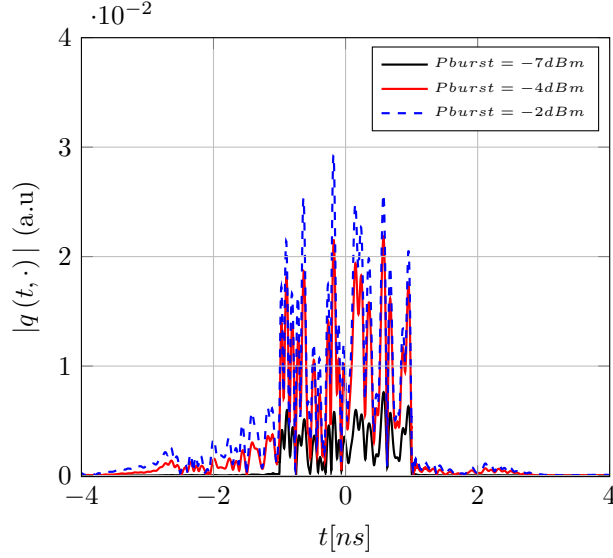


Figure 3.7: Comparison of NFDM signal with different input power levels.

3.5 NFDM digital receiver design

As shown in Fig.(3.3), the standard DSP processing blocks for a single polarization NFDM transmission system consists of time-synchronization, CFO estimation and compensation, signal normalization, NFT computation, 1-tap channel inversion, reverse mapping, guard interval removal, down-sampling, residual channel equalization, laser phase noise equalization, demodulation and BER estimation. The receiver DSP operation chain is described here briefly.

3.5.1 Time synchronization

Due to the absence of a synchronization mechanism between the transmitter and receiver, the transmitter clock is recovered from the received signal. Incorrect estimation of the starting point of the NFT window results in ICI between the subcarriers, and induces ISI between the NFDM symbols. The synchronization process uses the Schmidle-Cox method [114], which is the most celebrated synchronization method in linear OFDM systems, which relies on training symbols with two identical patterns, called the synchronization symbols (SS).

Let us assume that the first pattern of synchronization symbols at the receiver of length L is r_m . Then the auto-correlation metric is computed over a pre-

defined search by

$$P(d) = \sum_{m=0}^{L-1} r_{d+m}^* r_{m+d+L}, \quad (3.12)$$

where d is a randomly picked time index. The maximum value of the correlation metric $P(d)$ will determine the start point of the NFT window. In the burst mode NFDM/OFDM signal design, the correlation metric peak poses a sharp peak which is considered to be more accurate. However, the sharp peak is sensitive to the synchronization error as a result of a slight offset on timing estimation. From the time shift property of the NFT, a slight temporal shift in the synchronization window can be translated into a frequency dependent phase shift in the nonlinear frequency domain, that reads [94]

$$q(t - t_0) \leftrightarrow e^{-2i\lambda t_0} \cdot \widehat{q}(\lambda). \quad (3.13)$$

Such phase drift is common among symbols in a given frame, which makes it simple to compensate by using training symbols.

3.5.2 Carrier frequency offset compensation

The CFO in optical transmission is induced by the frequency mismatch between the optical carrier at the transmitter and the free-running LO at the receiver. CFO results in ICI, that destroys the orthogonality between neighboring subcarriers. CFO can be corrected by using an identical pattern in the synchronization symbol in the temporal domain [90].

In the presence of CFO ΔF_{CFO} , the n^{th} received sample becomes:

$$r_n = e^{i2\pi n\epsilon/N_{sc}} \sum_{m=1}^L h_m x_{n-m} \quad (3.14)$$

where x is the transmitted data, h is the transfer function of the channel and ϵ is the normalized CFO with respect to the subcarrier spacing Δf : $\epsilon = \Delta F_{CFO}/\Delta f_{sub}$. The estimated frequency offset at the k^{th} subcarrier can be written as:

$$R_k = \sum_{m=1}^{N_{sc}} \Psi_m^{CFO} H_m X_m \quad (3.15)$$

where Ψ^{CFO} is considered as common for all the subcarriers, i.e., independently of the subcarrier index, and is modeled as

$$\Psi_m^{CFO} = \frac{1}{N} \frac{\sin(\pi(\epsilon - m))}{\sin(\pi(\epsilon - m)/N)} e^{i\pi(\epsilon - m)(1 - \frac{1}{N})} \quad (3.16)$$

which suggests that the CFO induces an amplitude distortion, a phase shift on each subcarrier, and an ICI between different subcarriers.

3.5. NFDM digital receiver design

The CFO is a time-varying effect due to wavelength instability between the optical carrier and the LO. As a result, CFO rotates the received constellation and can reach values up to ~ 500 MHz (its typical value is < 50 MHz). The fractional and integral portion of the CFO value is estimated and compensated in the temporal and in the spectral domain, respectively [91]. The temporal domain compensation takes advantage of the repetitive structure of synchronization symbol in the frame-synchronization algorithm, while the residual frequency domain compensation is done by using the training symbols prior to residual channel estimation. It should be noted that, since CFO is a polarization independent effect, CFO in both polarizations can be compensated jointly for a better estimation.

3.5.3 Signal normalization

The NFT of the signal is computed by taking the normalized NLSE based channel model [75]. The received complex digital signal after synchronization is pre-distorted in the spectral domain to compensate for amplitude distortions experienced by the transmitter-receiver chain. First, the received signal, $Q(z, t)$, power is re-assigned to the power of the transmitted signal, as the performance of the NFDM depends on the power of the spectral amplitude. Next, the signal is normalized according to the normalization constant in Eq.(1.18) to remove any channel dependency.

3.5.4 NFT computation and channel inversion

Once the received signal is normalized, the nonlinear spectral amplitude $\widehat{q}(\lambda, L)$ at the receiver is computed by using the NFT block [75] (i.e., $\widehat{q}(\lambda, L) = \text{NFT}(q(z, t))$), where its implementation is given by Fig.(2.7). The NFT is used for sub-carrier demultiplexing. In the absence of noise, the linear propagation of the spectral data allows for a 1-tap channel inversion [75], [94]:

$$\widehat{q}_{eq}(\lambda, L) = H^{-1}(\lambda, L) \widehat{q}(\lambda, L) \quad (3.17)$$

where $\widehat{q}(\lambda, L)$ and $\widehat{q}_{eq}(\lambda, L)$ represent the nonlinear spectral amplitude at receiver before and after the channel inversion, respectively. Here, $H(\lambda, L) = e^{-i4s\lambda^2 L}$ is an all-pass-like channel filter. As mentioned several times, the 1-tap channel inversion stage removes the inter-play of dispersion and nonlinearity on the received NFDM symbols.

3.5.5 Spectral demapping and guard interval removal

Following channel inversion, the nonlinear spectrum amplitude is transformed from $\widehat{q}(\lambda, L)$ to $U(\lambda, L)$ as[75]:

$$U(\lambda, L) = \left(-2s \log \left(1 - s |\widehat{q}(\lambda, L)|^2 \right) \right)^{\frac{1}{2}} e^{i \angle \widehat{q}(\lambda, L)}. \quad (3.18)$$

The time domain equivalent signal is computed by the IFFT, i.e. $u(\tau, L) = \mathcal{F}^{-1}(U(\lambda, L))$, and the guard interval introduced at the transmitter is removed at the receiver in the normalized temporal domain.

3.5.6 Residual channel equalization

Due to the non-flat gain-loss spectrum of the fiber links, accumulated ASE noise, and random polarization fluctuations in fibers, the received signal always contains a mix of data from both polarization modes. Although the 1-tap channel inversion in Eq.(3.17), which assumes a lossless and noiseless transmission channel, is capable of compensating the interplay of fiber dispersion and nonlinearity, residual channel distortions still remain. In addition to the residual channel distortions due to non-ideal transmission components, distortion from electrical and optical components in the transmitter and receiver chain also contribute to residual distortions. All these effects should be compensated either completely or partially before mapping symbols to bits at the decoder. It is the task of the equalizer to mitigate all those effects in order to successfully recover the transmitted symbol stream.

In this thesis, a linear Zero-Forcing (ZF) equalization based on the training symbols is proposed, due to its simplicity in implementation and low computational complexity [115]. Moreover, any frequency and phase distortion introduced in time domain on the NFDM signal can be tracked by using a training symbols added in the nonlinear frequency domain. This assumption is based on the property of NFT for any phase and frequency offset, i.e., $e^{i\phi}q(t) \leftrightarrow e^{-i\phi}\widehat{q}(\lambda)$ and $e^{-i2\omega t}q(t) \leftrightarrow \widehat{q}(\lambda - \omega)$. ZF-equalization is performed when the residual channel impulse response H_R is compensated by directly applying its inverse to the detected signal at the receiver after the channel. Here, the channel response is assumed to be known at the receiver. Let us assume an optical channel with polarization diversity, which can be modeled as a 2×2 MIMO system

$$\mathbf{TS} = \begin{bmatrix} \mathcal{TS}_{t_1, x} & \mathbf{0} \\ \mathbf{0} & \mathcal{TS}_{t_2, y} \end{bmatrix}, \quad (3.19)$$

3.5. NFDM digital receiver design

where $\mathcal{TS} = [\mathcal{TS}(0), \dots, \mathcal{TS}(N_{sc})]$ and $\mathbf{0}$ represents the training symbols and the zero vector of subcarrier length N_{sc} . The training symbols in eq.(3.19) are implemented by sending a known symbol in the first NFDM symbol on the x -polarization, while zero symbols are sent over the y polarization, and the opposite is done for the second symbol. The symbols are concatenated in time, and they are separated by the symbol duration T_s , i.e. $t_2 = t_1 + T_s$. As a consequence of Lax convolution,[64], the receiver estimates the channel impulse response at each subcarrier $H_{R,k}$ by applying the following relation:

$$\widetilde{\mathbb{TS}}_k(\lambda, L) = H_{R,k}(\lambda, L) \mathbb{TS}_k(\lambda, 0) \quad (3.20)$$

where $\widetilde{\mathbb{TS}}_k(\lambda, L)$ is the received training symbols and $\mathbb{TS}_k(\lambda, 0)$ is the transmitted training symbols which is known at the receiver. The associated ZF-equalizer takes the form of the inverse, i.e. $H_{R,k}^{-1} = 1/H_{R,k}$. Therefore, a simple multiplication of the received signal with the ZF-equalizer is enough to restore the transmitted signal at the receiver. However, the ZF-equalizer is prone to noise enhancement, which leads to further system performance degradation. Therefore, channel transfer function estimation by averaging over several numbers of training symbols or channel estimation based on the minimum mean-square-error (MMSE) can be used to attenuate the noise contribution.

3.5.7 Laser phase noise compensation

The NFDM implementation requires a high-quality laser with a linewidth of few kHz to slow down the evolution of the random phase shift introduced by the optical carrier and the LO laser. Using a free-running laser with a large linewidth results in a phase drift within a given symbol, making it impossible to estimate and correct the phase error. Assuming that the phase evolution is slow compared to the symbol duration, phase noise induces a phase noise error common to all subcarriers, called the common phase error (CPE), and an ICI term [116].

In absence of ASE noise, the received NFDM signal can be written as

$$E(t) = E_0 \cdot e^{i(\Delta\omega\tau + \theta(\tau))} \quad (3.21)$$

where $\Delta\omega$ is the CFO, and $\theta(\tau)$ is the laser phase noise (PN). The laser phase noise at any discrete time instant is the phase noise difference between the transmitter and the LO lasers, i.e $\theta(n) = \theta_c(n) - \theta_{LO}(n)$. If the signal and LO lasers have Lorentzian line-shapes, the phase noise can be modeled by a Wiener process

$$\theta(n) = \theta(n-1) + \Psi(n) \quad (3.22)$$

where $\Psi(n)$ is a Gaussian random process with zero mean, and variance $\sigma^2 = 2\pi\Delta\nu T_s$, where $\Delta\nu$ is laser linewidth defined as the bandwidth at the full-width half-maximum (FWHM) of the laser power spectral density. Due to the time-varying random phase walk, a laser exhibits a typical linewidth in the range of $\sim 0.1\text{--}0.2$ MHz. In this work, an ECL with a typical linewidth value around 100 kHz was used. The phase noise can be estimated by removing the data subcarriers and then track the phase change using the pilot tones (known data on certain subcarriers). This pilot tone will experience the same phase noise than the whole NFDM signal, however, they are not used to encode any useful user information data.

Once a perfect time-synchronization, CFO compensation, and residual channel equalization have been performed, the pilot subcarriers dedicated to the phase noise estimation are extracted from the equalizer output for each NFDM symbols. Let us consider the received symbols corrupted with phase noise as [117]:

$$\tilde{U}_{l,k} = \tilde{c}_{l,k} H_{R,l,k} e^{i\Theta_l^{CPE}} + \epsilon_{l,k} \quad (3.23)$$

where $\tilde{U}_{l,k}$ and $\tilde{c}_{l,k}$ are the received and transmitted QPSK modulated pilot tones on k th subcarriers, $H_{R,l,k}$ is the channel impulse response, and $\epsilon_{l,k}$ is the ICI term modeled as additive white Gaussian noise. The term Θ^{CPE} is the CPE term in a given NFDM symbol. The QPSK modulated is used because of its tolerance to noise as the separation between constellations points are wider compared to 16-QAM modulation formats. This CPE value can be estimated by using the pilot tones, and the phase difference between the received pilot tones and the transmitted ones can be evaluated by averaging as [117]:

$$e^{i\Theta_l^{CPE}} = \frac{1}{N_p} \sum_{k \in \mathbb{PT}} \frac{\tilde{U}_{l,k} |\tilde{c}_k^d|}{|\tilde{U}_{l,k}| |\tilde{c}_k^d|} \quad (3.24)$$

where N_p is the number of known pilot tones \mathbb{PT} at the receiver. The phase equalization is done by multiplying the received symbols with the inverse of the estimated phase shift (Θ_l^{CPE}) as

$$U'(\lambda) = \tilde{U}_{l,k}(\lambda) e^{-i\Theta_l^{CPE}}, \quad (3.25)$$

In practice, only the common phase noise is compensated without addressing the ICI: such technique is known as pilot-aided phase compensation.

3.5.8 Data decoding and performance measurement

The NFDM decoder employs a maximum-likelihood detection method to recover the transmitted symbols from the noisy received symbols. The decoder

3.6. Experimental Validation

compares the received constellation symbols with every and each transmitted constellation points. Thereafter, the constellation point that corresponds to the smallest distance is selected as the most likely digital symbol, which can then be rearranged as a bit value.

The correct way to measure system performance is to evaluate the bit error ratio (BER), by comparing the received bits and the transmitted bits:

$$\text{BER} = \frac{\text{number of error bits}}{\text{number of total bits}}$$

In experimental measurements, the BER is estimated by directly counting the number of error bits. To ensure a reliable estimation, it is necessary to transmit a sufficient number of bits for a certain BER level. In optical communication systems, the measured BER is usually converted to an equivalent Gaussian noise quality factor (Q-factor) through the inverse complementary error function (erfc^{-1}) [118]. The Q-factor in dB as a function of BER is given by

$$Q_{dB} = 20 \cdot \log_{10} \left(\sqrt{2} \cdot \text{erfc}^{-1} (2 \cdot \text{BER}) \right). \quad (3.26)$$

Moreover, an alternative suitable metric for evaluating system performance is the error vector magnitude (EVM), which evaluates the average deviation of the received signal from the corresponding ideal signal in the constellation diagram. The EVM is represented by the normalized root mean square of the error vector of the received symbol from the reference position of the ideal symbols, denoted by E_{err} [119]:

$$E_{err,l} = E_{r,l} - E_{t,l}, \quad \text{EVM} = \frac{\sqrt{\langle |E_{err,l}|^2 \rangle}}{\max(|E_t|)}, \quad (3.27)$$

where $E_{r,l}$ is the l^{th} received symbol, $E_{t,l}$ is the l^{th} transmitted symbol, and $\langle \cdot \rangle$ is the averaging operation over the number of symbols. The EVM value, assuming AWGN channel, is converted approximately to the BER by [119]:

$$\text{BER} = 0.5 \cdot \text{erfc} \left(\frac{\text{EVM}^{-1}}{\sqrt{2}} \right). \quad (3.28)$$

In the following section, the experimental validation based on such DSP design is presented and discussed.

3.6 Experimental Validation

Numerical simulation is vital for testing the robustness of the INFT/NFT algorithm. However, the experimental demonstration is the ultimate validation tool to show that the NFDM is a data encoding scheme which is

compatible with the nonlinear-dispersive optical fiber channel. Two major distinct experimental setups for a single- and dual-polarization configuration will be considered for the demonstration of the gain achieved by the NFDM transmission, when compared to its linear counterpart, OFDM. A detailed description of the laboratory setup and the obtained results are provided in the following subsections.

3.6.1 Experimental demonstration of a single-polarization NFDM transmission

A simplified experimental schematic of a single polarization NFDM/OFDM transmission setup is presented in Fig. (3.3). In the experiment, OFDM and the NFDM systems with comparable transmitter (TX) and receiver (RX) DSPs are considered. The DSPs are summarized in the inset of Fig. (3.3), where the white DSP blocks correspond to the OFDM, and the yellow DSP blocks indicate the additional DSP layers required for NFDM.

The data structure of NFDM consists of a 32×64 matrix of complex symbols at the transmitter as illustrated in Fig.3.8. The symbols duration for NFDM is 2 ns, which correspond to a baud rate of 16Gbd (gigabaud). The rows and columns denote, respectively, the orthogonal sub-carriers and the corresponding symbols. The symbols include synchronization symbols, training symbols, data symbols, and zeros. The INFT and IFFT in NFDM are applied to each column, except for the synchronization symbols. The resulting sub-signals are concatenated, to obtain the entire signal that is transmitted over the fiber channel.

In NFDM, the offline transmission DSP begins by modulating a sequence of complex symbols $\{c_l\}$ according to eq.(3.5) from a 16QAM constellation as [96],[75]

$$\begin{aligned} U(0, \lambda) &= P_{max} \sum_{l=1}^{N_{sym}} \sum_{k=1}^{N_{sc}} c_l^k \frac{\sin(\lambda - kW_0)}{(\lambda - kW_0)} e^{i\lambda lT} \\ &= P_{max} \sum_{l=1}^{N_{sym}} \sum_{k=1}^{N_{sc}} c_l^k \delta(\lambda - kW_0) \end{aligned} \quad (3.29)$$

where P_{max} is the peak power of the signal, N_{sc} is the number of sub-carriers, N_{sym} is the number of symbols, W_0 is the sub-carrier spacing, and $\lambda = \pi f$, where f is the frequency. Here, $G(\lambda - kW_0) = \text{sinc}(\lambda - kW_0)$ is a narrow width *sinc* basis function borrowed from the OFDM, which can fairly be approximated by the Kronecker delta function $\delta(\lambda)$ so that U is discretized

3.6. Experimental Validation

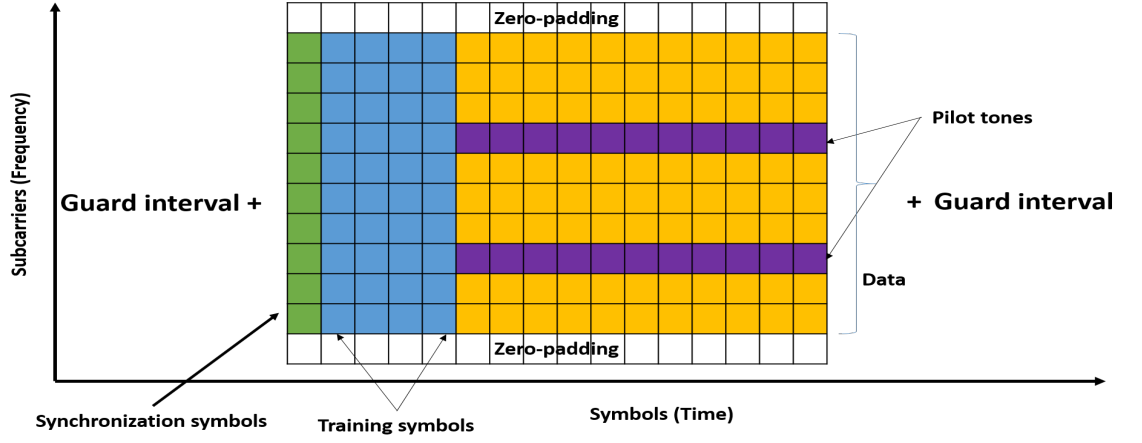


Figure 3.8: 2D symbol matrix structure of NFDM/OFDM in frequency (subcarriers) and time (symbol).

to the vector of symbols $\{c_l^k\}$. It is clear that the NFDM system is the nonlinear counterpart of OFDM, i.e. $U(f) = U(\lambda/\pi)$, where $U(f)$ is the OFDM signal in the linear spectral domain and $U(\lambda)$ is the NFDM signal in the nonlinear frequency domain. The resulting signal is over-sampled by a factor of 32 for accurate INFT computation. One then generates $u(0, \tau)$ by using Eq.(3.6) to introduce guard time in the virtual time τ domain. If the duration of $u(0, \tau)$ is T_s seconds, two blocks of zeros, each with duration $2.5T_s$, are added to the left and right of $u(0, \tau)$, to obtain $u'(0, \tau)$ with the total burst duration of 12 ns and $U'(0, \tau) = \mathcal{F}(u(0, \tau))$. The transmitted signal in the spectral domain $\hat{q}(0, \lambda)$ is computed using eq.(3.8).

Finally, the INFT maps the $\hat{q}(0, \lambda)$ to the continuous part of the nonlinear spectrum of the output signal $q(0, \tau) = \text{INFT}(\hat{q}(0, \lambda))$, which is then unnormalized to realistic units using Eq.(1.18). Fig.(3.9) illustrates a typical train of NFDM and OFDM temporal domain signals. The NFDM symbols exhibit a decaying tail as the input power increases. Whereas, OFDM symbols retain their shape for any given input signal power.

The TX and RX equipments introduce significant distortions, particularly to the power profile of the signal. The non-uniform amplitude response of the transmitter is partially equalized at this stage via inversion of the magnitude response of the launched optical pulse obtained from the optical spectrum analyzer (OSA) in the digital domain, as shown in Fig.(3.10). The signal is then down-sampled to 64 GSa/s before being loaded into the arbitrary waveform generator (AWG).

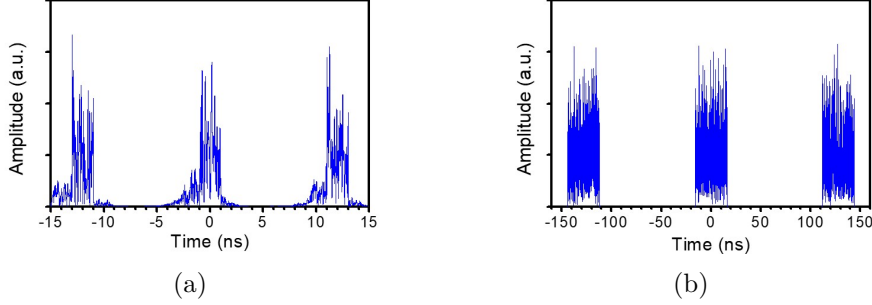


Figure 3.9: A typical sample of (a) NFDM, and (b) OFDM temporal domain waveforms.

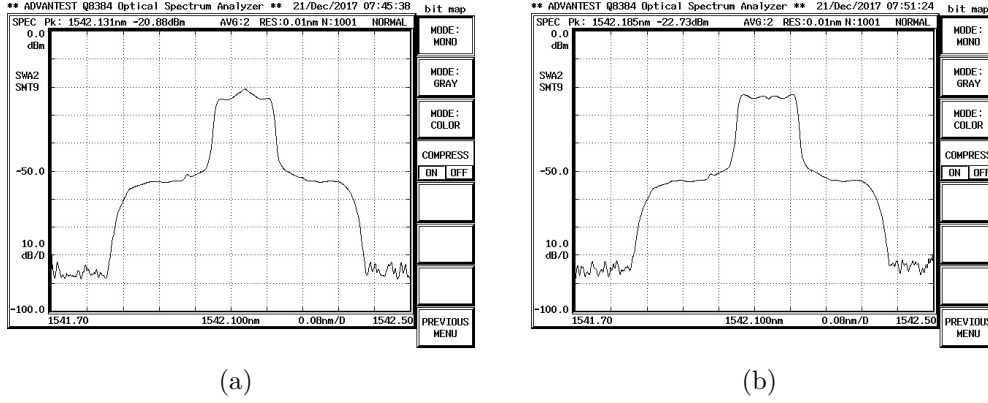


Figure 3.10: Pre-distortion of the NFDM signal (b) in order to compensate for non-uniform amplitude response of transmitter (a).

3.6.1.1 Experimental Setup

In this thesis, we consider an experimental setup with 3 WDM channel with a 50 GHz spacing. The central channel is optically generated by an ECL with 100 kHz linewidth at 1550 nm. Two additional distributed feedback (DFB) lasers are used to generate the WDM dummy channel at the boarder of the multiplexer. The relative channel locations guarantee enough separation between the central NFDM channel and the dummy channels, so that any interference effect is absent. The output I and Q signals from the AWG are amplified by RF-drivers and then modulated onto optical field using nested IQ-Mach-Zehnder modulator (MZM). The transmitted signal propagates inside a re-circulation loop, which is controlled by an acousto-optical modu-

3.6. Experimental Validation

lator (AOM). The recirculating loop in Fig.(3.3) consists of 2 spans of 70 km TrueWave Submarine Reduced Slope (TW-SRS) fiber, with attenuation of 0.2 dB/km, chromatic dispersion $D = -4.66$ ps/(nm-km), and effective area of $A_{eff} = 53.5 \mu m^2$ at 1550 nm. The optical power at the fiber input and output is controlled by two EDFAs with noise figure $NF = 5.5$ dB cascaded with a variable optical attenuator (VOA). A bandwidth-adjustable Finisair waveshaper (WS) is used as gain equalizer filter to equalize the power level in all channels, compensating for loss-gain imperfection of EDFA-amplified optical link. The transmission link consists of 10 loops, for a total 1400 km of transmission length.

At the receiver, the signal is detected by a coherent intradyne receiver using the same ECL laser at the TX as local oscillator (LO), and then sampled by a realtime 50 GSa/s Tektronix digital phosphor oscilloscope (DPO). Here, the optical carrier at the TX and the LO at the Rx are not phase locked even though they are assumed to be frequency locked. The phase drift are resulted from a temperature variation and the fiber path length the ECL signal traversed between TX and RX devices. After timing synchronization and CFO compensation by using the synchronization symbol, amplitude post-correction is carried out in order to compensate for the non-uniform amplitude response of the receiver hardware. This post-correction is done in the frequency domain by using training symbols, so that the received spectrum matches that of the transmitted spectrum, as illustrated in Fig.(3.11). The received signal power is re-scaled to account for power variations in the recirculation loop. Then the signal is normalized before that the NFT of the received signal is taken as $\hat{q}(\lambda, L) = \text{NFT}(q(t, L))$, in order to recover the continuous part of the nonlinear spectrum. The channel effect on the signal is reversed by a single-tap equalizer as given by Eq.3.17. Finally, $U(\lambda, L)$ is computed by using Eq.(3.18), followed by down-sampling and guard interval removal. The residual channel coefficient H_R is estimated for each subcarrier by using training symbols in the λ domain. The laser phase noise, specifically the common phase error, is also estimated and removed by using pilot tones.

3.6.1.2 Experimental Results

Let us compare the Q-factor of NFDm and OFDM transmissions, with the same launch power and bandwidth. The powers reported here correspond to the signal that goes into the fiber, when taking into account the guard intervals and the TX front-end loss.

The Q-factors as a function of the input power are plotted in Fig.(3.12).

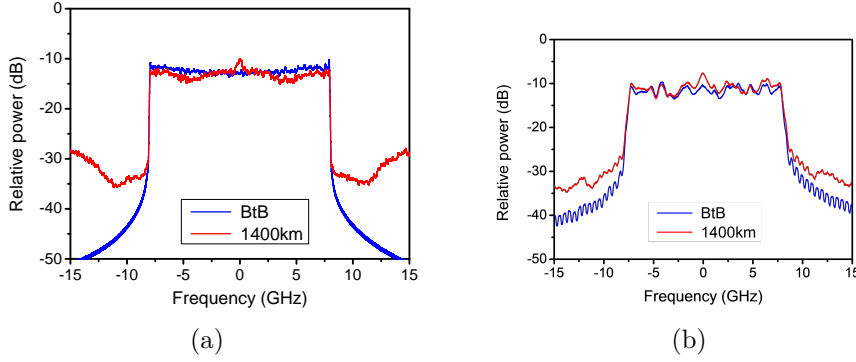


Figure 3.11: The received spectra of OFDM and NFDM after post-correction (a-b). Compared to NFDM, the OFDM spectrum shows significant distortions from four wave mixing (FWM).

Optimal performance for NFDM is obtained at -6 dBm for 8 Gbaud (i.e., only 16 subcarriers are used), and at -3 dBm for 16 Gbaud transmission. As shown in Fig.(3.12), NFDM exhibits 0.7 dB Q-factor gain and 1 dB peak-SNR (or launch power) gain over OFDM at 16 Gbaud.

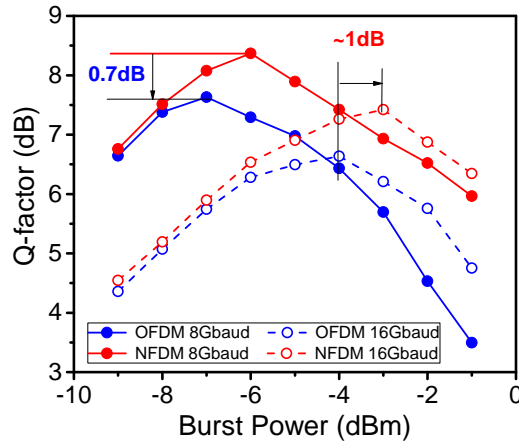


Figure 3.12: Q-factors as a function of burst power for single polarization NFDM and OFDM transmissions.

The relative error in the continuous spectrum is less than 5% in simulations, while in experiments it is of about 18% in back-to-back and 30% after fiber propagation, as illustrated in Fig.(3.13). The gap between simulations and experiment is partly because the experiment is conducted with non-ideal equipment and corresponding sub-optimal DSP. It is expected that NFDM performance can be substantially improved by utilizing advanced DSP, e.g.,

3.6. Experimental Validation

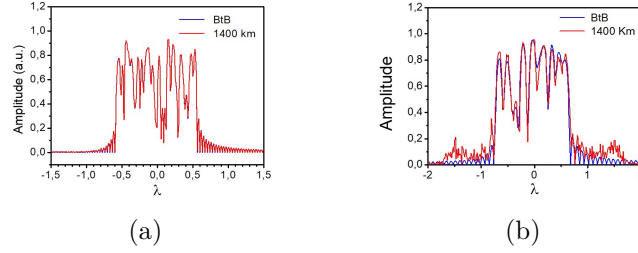


Figure 3.13: A relative error between the input and output in the nonlinear spectral amplitude $\widehat{q}(\lambda, \cdot)$ in (a) simulation, and (b) experiment for 16GHz NFDM transmissions.

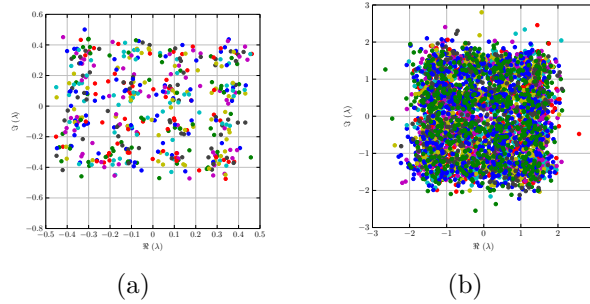


Figure 3.14: The Received constellations at $P = -3$ dBm for 16GHz (a) NFDM and (b) OFDM.

by compensating for the DAC response, IQ-modulator, etc. Indeed, it was shown recently that TX and RX adaptation may improve the peak-SNR gain by as much as 3 dB [105]. We leave harnessing these potentials to future work.

3.6.2 Experimental demonstration of a dual-polarization NFDM transmission

The $32 \times 0.5\text{Gb/s}$ NFDM/OFDM symbols in each polarization consist of 32 orthogonal subcarriers modulated with 16QAM complex symbols at the transmitter as Eq.(3.29). The transmitted symbol blocks include synchronization symbols (SS), polarization separation symbols (PSS), training symbols (TS), and data symbols, as shown in Fig.(3.15). The (PSS) symbols are generated using OFDM with cyclic-prefix for MIMO channel separation. Whereas (TS) and data symbols are defined in the NFT domain, and the prior used for MIMO channel equalization.

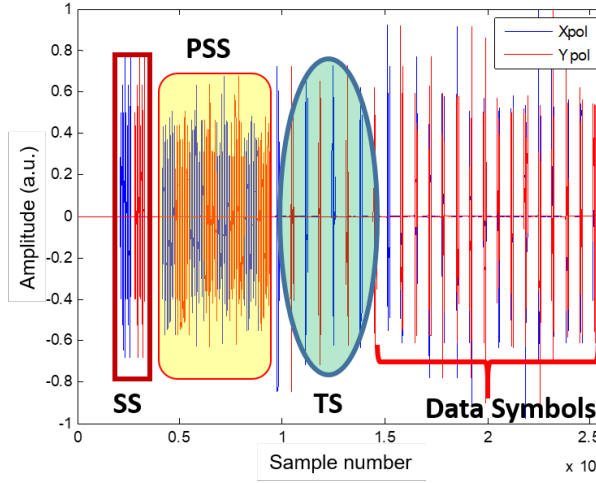


Figure 3.15: Data structure of real part of 16QAM PDM-NFDM/OFDM.

NFDM symbols are oversampled by a factor of 8, thus increasing the sampling frequency from 64 GSa/s to 512 GSa/s, for accurate computation of the nonlinear spectrum. We compute $u = \mathcal{F}^{-1}(U)$ in order to introduce a guard band of 8 ns, to satisfy the vanishing boundary conditions of the Zakharov-Shabat spectral problem [14] in the time domain (i.e., a total symbol duration of ~ 10 ns). Since NFT processing is applied to each data symbol separately, guard bands added to both front and end of NFDM/OFDM symbols prevent inter-burst interference, and accommodate symbol broadening due to the combined action of dispersion and nonlinearity during fiber propagation. Prior to mapping user data into the NFT domain according to Eq.(3.8), we compute $U = \mathcal{F}(u)$. Time domain NFDM symbols are computed by the INFT algorithm. Four of the subcarriers are used as pilot tones for laser phase noise estimation.

To perform dual-polarization transmission, we use a polarization division multiplexing emulator (PDME). In most experiments, a PDM emulator is usually applied when a single transmitter setup is available. As shown in the inset in Fig.(3.16), the single complex I/Q modulator serially generates both X and Y polarization data as follows: $q_y^1, q_x^1, q_y^2, q_x^2, \dots$. Next, the PDME splits the two orthogonal polarization components of the signal, delays the Y component by one symbol, and recombines them. As a result, NFDM symbols not involving the same serial number in the two polarizations (as indicated by red circles in Fig.(3.16)) are discarded at the receiver.

3.6. Experimental Validation

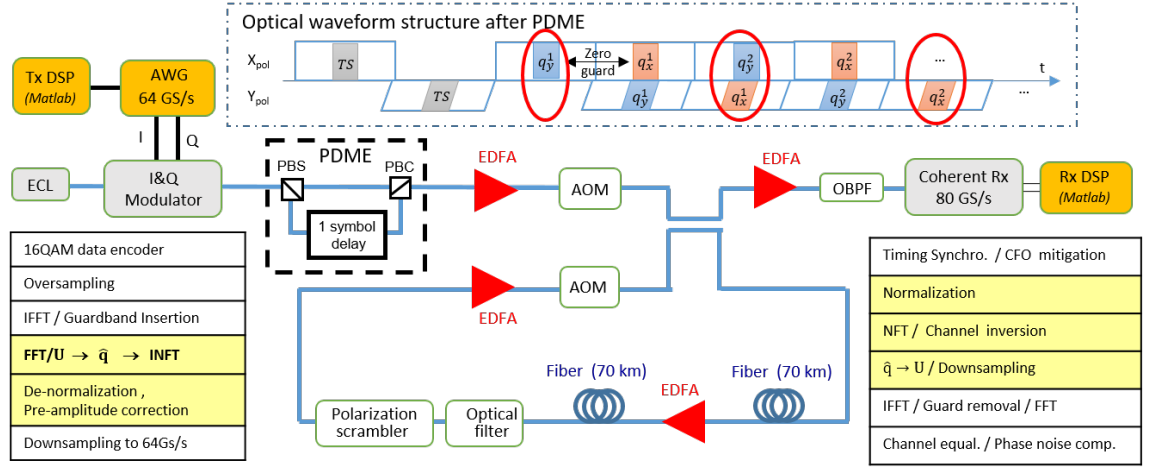


Figure 3.16: Experimental setup, PDM-NFDM data stream structure and of-line Tx/Rx DSP

3.6.2.1 Experimental Setup

Fig.(3.16) above shows the experimental setup of our 16 GHz PDM-NFDM/OFDM transmission system: yellow boxes indicate the additional DSP block for NFDM. The NFDM signal is resampled to 64 GSa/s before being loaded into the arbitrary waveform generator (AWG). The optical signal is generated by using a complex I/Q modulator. Linear adaptation is employed to pre-equalize only the amplitude imperfection of the transmitter and receiver.

The I/Q modulator output passes through the PDME with 1 symbol time delay (~ 10 ns), is amplified and then launched into a negative dispersion fiber designed for submarine transmissions (TW-SRS fiber, $\alpha = 0.2$ dB/km, $D = -4.66$ ps/nm/km and $A_{eff} = 53.5 \mu m^2$). The transmission link within the recirculating loop consists of two 70 – km fiber spans and two EDFAs (NF = 5.5 dB). An optical band-pass filter (OBPF) with a 3–dB bandwidth of 1 nm is used inside the loop, to suppress out-of-band ASE noise. A polarization scrambler is included in the loop, to randomize the polarization state after each loop. Moreover, the scrambler is added in order to prevent any spurious effects due to using the same fiber multiple times. The same ECL ($\Delta f \approx 100$ kHz) is used both as the optical carrier, and the local oscillator at the transmitter and receiver, respectively. The signal is detected by an intradyne coherent receiver, and sampled by a real time 80 GSa/s sampling oscilloscope. The sampled signal is analyzed by offline digital signal processing (DSP), whose structure is also shown in Fig.(3.16).

At the receiver, after timing synchronization and carrier frequency offset

(CFO) compensation by using synchronization symbols, the received samples are separated in time blocks. The (PSS)-symbols are separated, and chromatic dispersion compensation applied to them. The compensated (PSS) symbols are then used to separate the two states of polarization and equalize the amplitude distortion arising from transmission imperfections. NFDM symbols are then normalized for carrying out the NFT operation. Here the wrongly combined symbols are dropped as shown in the inset of Fig.(3.16). Channel inversion on the received $\hat{\mathbf{q}}$ is done by using a single-tap equalizer, to compensate for both dispersion and nonlinearity jointly according to Eq.(3.17), and translated into the U-domain using Eq.(3.18). After removing the guard bands in time domain, and resampling in frequency domain, the received symbols are compensated for residual channel amplitude and phase distortions in the nonlinear frequency domain by using NFT training symbol-aided MIMO channel estimation. The pilot-aided laser phase noise estimation was done in the NFT domain, because any phase variation that affects the time domain signal directly translates into phase noise in the NFT domain. Finally, maximum likelihood detector based symbol decision and bit error rate (BER) calculation were performed.

3.6.2.2 Experimental Results

In Fig.(3.17), typical examples of transmitted PDM-NFDM symbols are presented. Similar to the single polarization, the signal energy in the decaying tails increases with input power, and it is taken into account in INFT processing. The received constellations at -3 dBm optimal launch power are presented in Fig.(3.18). In Fig.(3.19) we compare the Q-factor of single- and dual-polarization NFDM with OFDM, for the same baud-rate and input launch burst power. The Q-factor is calculated from the BER measurements. The BERs values are almost identical for both polarizations. For a fair comparison between NFDM and OFDM, we do not include a cyclic prefix in OFDM data symbols: therefore, chromatic dispersion equalization is applied before the OFDM receiver. The input launch power reported in Fig.(3.19) corresponds to the average launch power in the fiber including guard bands.

We exploit training symbols to correct potential synchronization timing errors. Synchronization timing errors manifest themselves as a frequency dependent phase shift, that can be compensated by using the time shift property of the NFT Eq.(3.13). RX DSP was thus optimized to minimize phase error, which is the key for performance gain in NFDM transmissions. As a result, Fig.(3.19) shows that optimal performance is obtained at -4 dBm

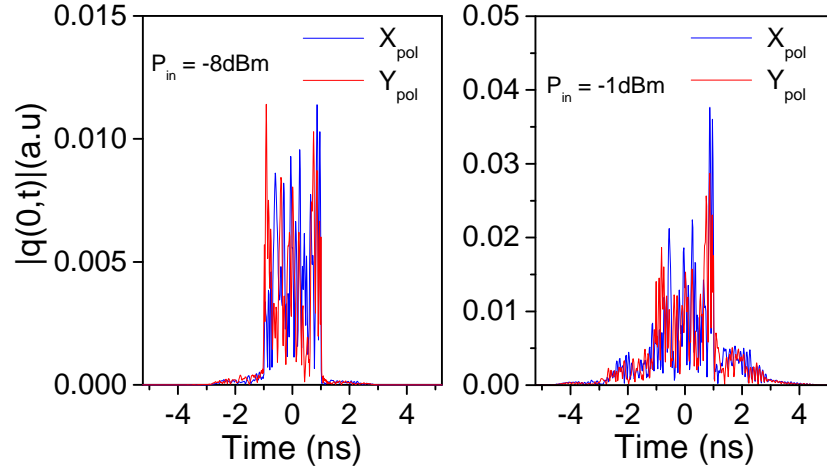


Figure 3.17: Examples of PDM-NFDM time domain symbols.

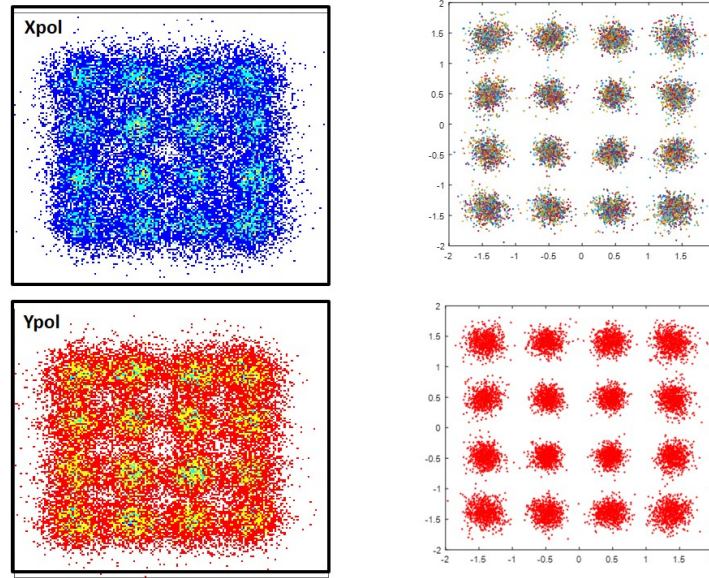


Figure 3.18: Received constellations at $P = -3$ dBm for PDM-NFDM after a transmission and in a back-to-back configuration.

for PDM-OFDM, and -3 dBm for PDM-NFDM, with a peak Q-factor of 6.84 dB and 7.25 dB, respectively. For SP-OFDM and SP-NFDM, optimal Q-factors of 7.1 dB and 7.5 dB are obtained, at launch powers of -5 dBm and -4 dBm, respectively. At low powers, we observe a 2 dB power difference between SP and PDM-NFDM instead of normally expected 3 dB. We can observe that, at lower powers the single polarization transmission is al-

ready entering the nonlinear regime. Furthermore, for the same power in a dual-polarization transmission, the nonlinearity is distributed over the two polarizations, while in a single-polarization transmission it all falls on the single-polarization. In our experiments, polarization impairments such as differential group delay (DGD), polarization mode dispersion (PMD), and polarization dependent loss (PDL) were not compensated for. Also non ideal polarization demultiplexing which induce a penalty.

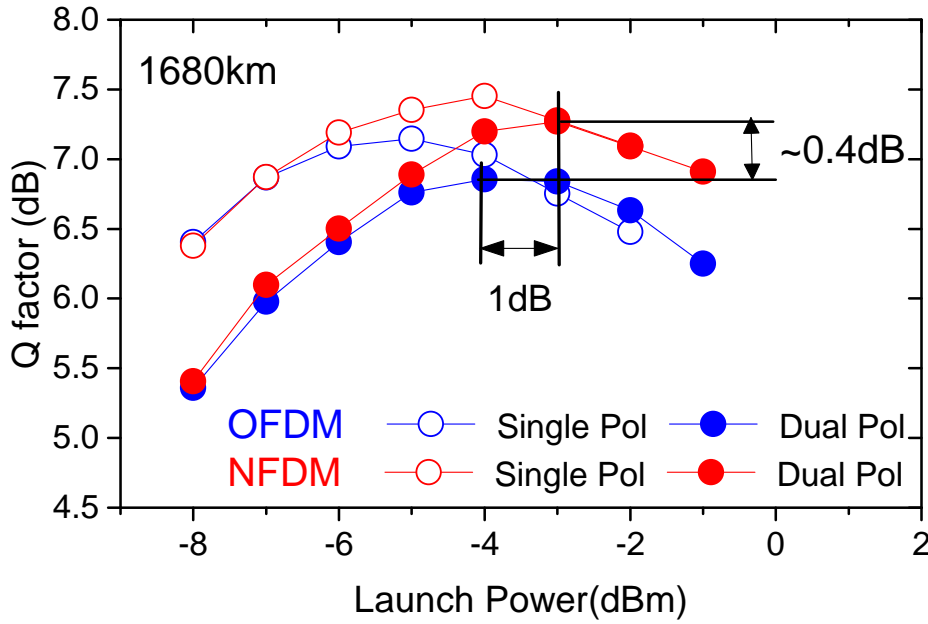


Figure 3.19: NFDM and OFDM results in SP- and PDM-NFDM.

To estimate the effect of DGD on the performance of NFDM and OFDM, we introduce an extra time delay at the AWG between successive symbols. This results in a temporal mismatch between the two polarizations at the PDME output. We reduced the propagation distance to 980 km, in order to increase the Q-factor, thus allowing for more accurate assessment of DGD effects. Fig.(3.20) shows that DGD has a higher impact on the Q-factor for PDM-NFDM than for PDM-OFDM. However, for typical PMD parameters less than $0.1 \text{ ps}/\sqrt{\text{km}}$, the Q-factor penalty caused by DGD is insignificant for the transmission distance of our experiments.

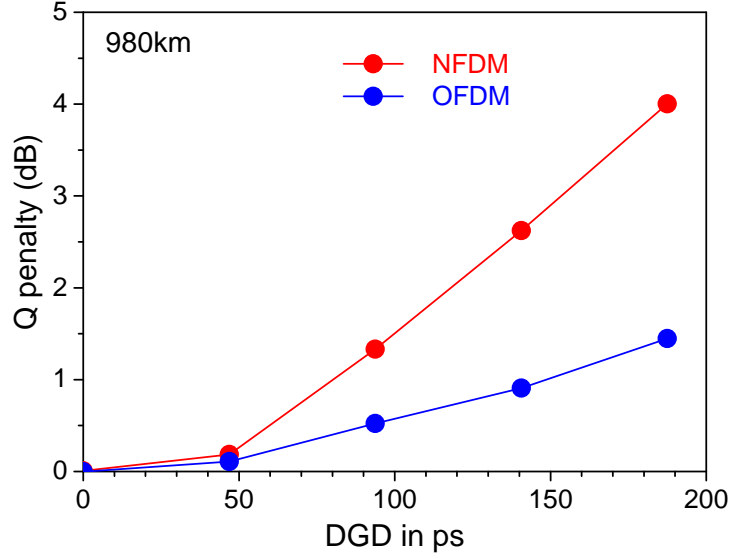


Figure 3.20: Q penalty induced by DGD.

3.6.3 NFD comparison in the normal and anomalous dispersion regime

In this experiment, continuous spectrum modulation has been investigated in both the normal and the anomalous dispersion regime. The experimental setup is similar to that shown in Fig.(3.16). For the anomalous dispersion case, the re-circulation loop, which replaces the TW-SRS fiber ($\alpha = 0.195$ dB/km, $D = -4.66$ ps/nm/km and $S_{\text{eff}} = 53.5 \mu\text{m}^2$), is composed by 11-spans of 75 km SMF-28 fiber with dispersion $D = 17.5$ ps/nm, nonlinear coefficient $\gamma = 1.25 \text{ W}^{-1}\text{km}^{-1}$, effective area $S_{\text{eff}} = 80.0 \mu\text{m}^2$, attenuation $\alpha = 0.195$ dB/km, and PMD coefficient $D_p < 0.1$ ps/ $\sqrt{\text{km}}$.

In the anomalous dispersion regime, the signal energy is strong enough to nucleate solitons [103] on top of the dispersive radiative part. The solitonic and radiative degrees of freedoms remain decoupled, and can be modulated independently. However, in this experiment the continuous spectrum only is modulated, and system performance is compared with the case of normal dispersion regime.

The system performance in terms of Q-factor as a function of the total launch input power is shown in Fig.(3.21). The performance difference in the two experiments, i.e. the normal and anomalous dispersion regimes, is rather small, which suggests that there is no significant interaction between the continuous spectrum and noise induced solitonic components in the NFD

system [126]. As shown in Fig.(3.21), optimal performance is obtained at -2 dBm for PDM-NFDM in the anomalous dispersion regime, and -3 dBm for PDM-NFDM in the normal dispersion regime, with a peak Q-factor of 7.41 dB and 7.27 dB, respectively. For PDM-OFDM, optimal Q-factors of 7.10 dB and 6.85 dB are obtained, at launch powers of -2 dBm and -4 dBm in the anomalous and normal dispersion regimes, respectively. In this experiment, optimal power in the anomalous dispersion regime exhibits a 2 dB power difference when compared with the normal dispersion regime. This performance difference is attributed to the smaller effective area (A_{eff}) of the SSMF, which leads to a lower nonlinearity value when compared with the NZDSF– (TW-SRS) fiber. Moreover, the higher dispersion value of the SSMF when compared with the TW-SRS fiber force the signal to disperse wider in temporal domain thus effectively reducing the peak power of the NFDM signal. As a results, the SSMF shows a better nonlinearity tolerance as the nonlinear effects depend on the pulse peak power.

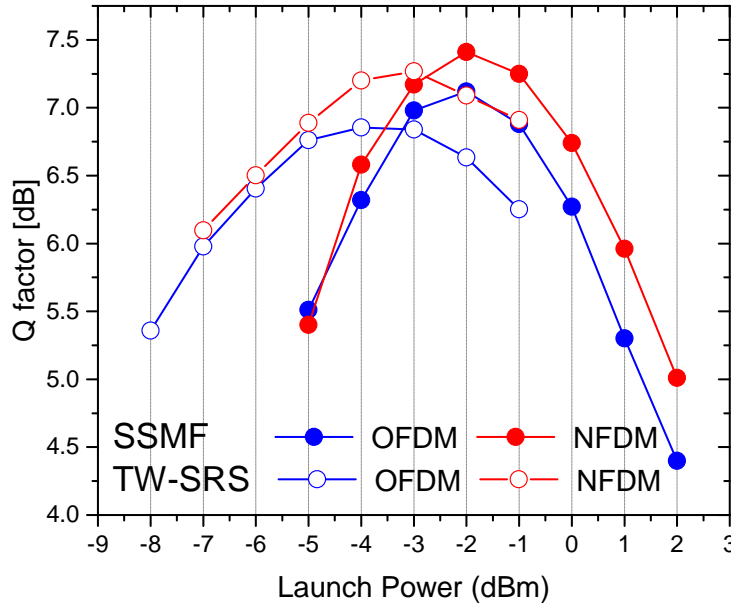


Figure 3.21: The PDM-NFDM experiment in the normal and anomalous dispersion regime using either the TW-SRS or the SSMF fiber, respectively.

3.7 Conclusions

In this chapter, the transmitter and receiver DSP-architecture of the proposed NFDM optical transmission system based on the NFT has been presented in detail. Single and dual-polarization NFDM transmissions using the continuous spectrum in normal dispersion regime have been experimentally validated for the first time. Moreover, when compared with OFDM with the same bandwidth and power, NFDM demonstrated 1 dB of better nonlinear tolerance in a transmission system with 16 Gbaud symbol-rate, 16 QAM modulation and 1400 km transmission reach in single polarization configuration. Similarly, when compared with PDM-OFDM, PDM-NFDM transmission shows a Q-factor gain of 0.4 dB (OSNR gain of 1 dB) over 1680 km by using the continuous spectrum in normal dispersion optical fiber. In the anomalous dispersion regime, NFDM shows similar performance as the normal-dispersion regime. However, NFDM demonstrates better OSNR performance. We believe that these experiments provide a first step in developing the full potential of nonlinear signal multiplexing in optical fibers.

In the next chapter, the discussion will focus on the numerical investigation of some of the NFDM implementation challenges and, along with their proposed solutions.

3.7. Conclusions

Chapter 4

Practical challenges in NFDM implementation

“ I don't know anything, but I do know that everything is interesting if you go into it deeply enough. ”

Richard P. Feynman,

BY using the NFT, the evolution of signal over an ideal optical fiber can be mapped into the nonlinear spectral domain, where the nonlinear spectral amplitudes propagate linearly and independently [64]. NFDM transmission based on the NFT is based on encoding the information on the nonlinear spectrum [93], which in principle allows for interference-free communications, i.e., both the inter- and intra-channel interferences due to the interplay of dispersion and nonlinearity are absent. However, for realistic optical fiber channels, which take impairments such as noise, fiber loss, higher order dispersion and nonlinearity into account, force practical NFDM system to be sub-optimal. Moreover, linear and nonlinear distortion contributions from various optical and electrical transmission components may be considered as bottlenecks for the practical demonstration of performance gain by NFDM as suggested in [75].

NFDM systems that use the continuous spectrum suffer from a temporal broadening upon dispersive propagation. In order to accommodate this temporal broadening, NFDM symbols are designed in the burst-mode, by which successive symbols are separated by a guard intervals with a duration longer than the maximum delay spread of the optical channel. Although the guard

4.1. Simulation setup

interval improves the numerical accuracy of the NFT/INFT algorithms (i.e. more samples are available to discretize the nonlinear frequency), the computational complexity increases while computing nonlinear spectral amplitudes. Moreover, the use of guard intervals reduce the spectral efficiency of the NFDM system.

The ideal channel model of the NLSE neglect the intrinsic fiber loss and noise. The presence of these impairments, however, threatens the integrability of the NLSE given in Eq.(1.17). In the case of NFDM transmissions, noise-signal interactions and the effectiveness of the lossless path averaging (LPA)-model at higher signal powers may be considered as the origins of performance degradation in NFDM transmissions. In addition to the aforementioned intrinsic challenges, the laser introduces a nonlinear phase noise (NPN) and a carrier frequency offset (CFO) that further degrade the NFDM system performance.

In this chapter, to corroborate the experimental results, a numerical investigation of the implementation challenges of a single polarization NFDM systems is presented. The organization of this chapter is as follows: section 4.1 describes the simulation model used for the numerical investigation of a single polarization NFDM system challenges. The physical challenges associated with the fiber channel will be analyzed in section 4.2, starting from the perturbation analysis model of the NLSE. The perturbation analysis is used to demonstrate NFDM transmission performance in a noisy and lossy optical fiber channel model, which can be considered as integrability breaking effects. In section 4.3, the optical challenge due to nonlinear laser phase noise is discussed. Moreover, a detailed analysis and simulation of performance penalty due to a variable guard interval and the oversampling factor is presented in section 4.4. Finally, in section 4.5 the transmitter and receiver device penalties on NFDM are discussed before drawing our conclusions.

4.1 Simulation setup

The NFDM system is simulated and studied in a single polarization configuration by using a MATLAB[®] model. The simulation diagram is shown in Fig.(4.1). The design consists of three main parts: the NFDM transmitter (TX DSP), the amplified optical fiber link and the NFDM receiver (RX DSP).

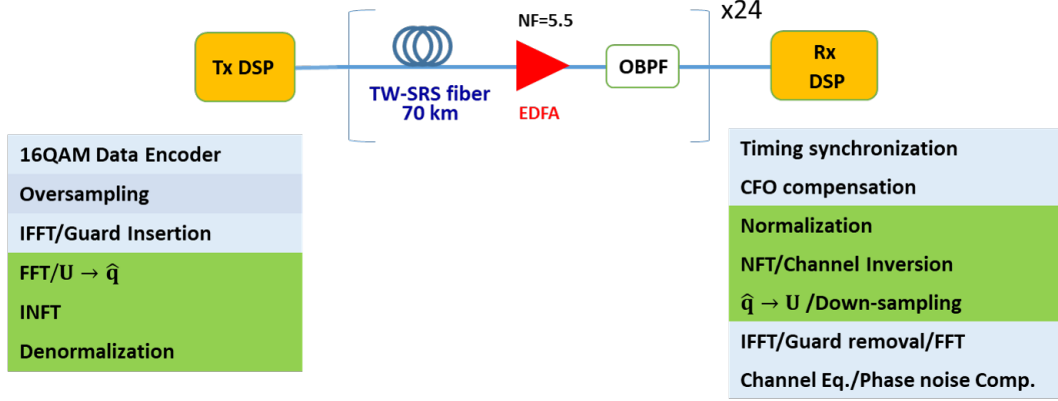


Figure 4.1: Simulation setup.

The simulation set-up is based on an optical 16-QAM NFDM transmitter with a bandwidth of 16 GHz, corresponding to an aggregate bit rate of 128 Gb/s. At the NFDM transmitter, a pseudo-random binary sequence (PRBS) stream is mapped to the 16-QAM format and oversampling is performed. Here, the NFT size is 128, and the useful symbol duration is $T_s = 2$ ns. The middle 64 subcarriers (out of 128) are filled, from which 4 pilot subcarriers are used for phase estimation. A number of training symbols is included for channel estimation prior to the oversampling (OS) stage. After oversampling, the frequency domain signal is converted into a time domain signal $u(0, \tau)$ by using the IFFT. The NFDM signal can be mathematically written as

$$u(0, \tau) = \sum_{k=1}^{N_{sc}} c_k(\tau) \cdot e^{i2\pi\lambda_k\tau} \quad (4.1)$$

where c_k is the pulse shaped symbol corresponding to the k^{th} subcarrier and N_{sc} is the total number of digital subcarriers.

As far as the guard interval (GI) is concerned, it is applied to prevent system degradation by inter symbol interference (ISI) and inter carrier interference (ICI). Basically, the GI consists of a number of zeros signals used in order to separate the successive NFDM symbols. By increasing the GI, the NFDM system is more robust toward CD induced pulse broadening, but on the other hand it suffers from a non-negligible data rate overhead. Since the NFDM symbols are (see Eq.(4.1)) in the temporal domain, a FFT is applied before mapping the burst-mode NFDM symbols into the continuous part of the nonlinear spectrum $\hat{q}(0, \lambda)$ by using Eq.(3.8). Then, an INFT is performed to obtain the time domain NFDM signal $q(0, \tau)$ in the normalized NFT domain before de-normalizing it according to Eq.(1.18). Time synchronization

4.1. Simulation setup

symbols are added before the NFDM frame. Finally, the de-normalized data $q(0, t)$ is serialized by using the parallel-to-serial (P/S) converted before that the signal is transmitted over an optical fiber channel.

In simulations, optical loop consists of 24-spans of TW-SRS fiber; each span was 70 km long. The TW-SRS fiber parameters are shown in Table 4.2. The signal evolution inside the dispersive and nonlinear channel, i.e., optical fiber, is numerically simulated by using the split-step Fourier method (SSFM). Accumulated power loss from the fiber span was ~ 14 dB for each span. Power losses in each span were compensated by EDFAs with noise figure $NF = 5.5$ dB. The accumulated ASE noise was filtered out by using a Gaussian optical band-pass filter (OBPF) with $\Delta v = 0.4$ nm bandwidth.

At the NFDM receiver, timing synchronization is performed to accurately detect the NFT-processing window, which is followed by CFO estimation and compensation. The synchronization symbol is separated from the rest of the NFDM symbols, and then serial-to-parallel converted using the serial-to-parallel (S/P) converter. Next the signal is normalized according to Eq.(1.18) before that the NFT is performed to compute the nonlinear spectral amplitude $\hat{q}(L, \lambda)$, and we apply a 1-tap channel equalizer $H = e^{-i4\lambda^2 L}$ in order to remove the propagation effect. The NFDM symbols are applied to the inverse mapping, in order to convert the continuous spectrum to the NFT domain signal $U(z, \lambda)$ by using Eq.(3.18). In order to recover the original NFDM signal, the guard interval, which was inserted at the transmitter side, should be removed in the temporal domain. The FFT is then performed to recover the sub-carriers, which facilitates a frequency domain down-sampling of the NFDM symbols. After down sampling, residual channel estimation and compensation using a zero-forcing equalizer is done in the NFT domain. Then laser phase noise estimation and compensation, demodulation and BER estimation follow, before that parallel-to-serial conversion retrieves the data. The implementation challenges of the NFDM system are investigated on the basis of the above configuration.

Table 4.1: NFDM parameters.

Parameter	Value	Parameter	Value	Parameter	Value
Bandwidth	16 GHz	Sampling rate	64 G Sa/s	NFT size	128
OS factor	8	GI factor	6	T_s	2 ns
Modulation	16-QAM	Pilots	4	TS	4
N_{sc}	64	NFDM frame size	100		

Table 4.2: TW-SRS parameters.

Parameter	Value	Parameter	Value
A_{eff}	$53.5 \mu\text{m}^2$	PMD	$0.1 \text{ ps}/\sqrt{\text{km}}$
α	0.2 dB/km	D	-4.66 ps/nm/km

Table 4.3: System parameters.

Parameter	Value	Parameter	Value
Span length	70km	No. fiber span	24
Laser linewidth	100 kHz	ENoB	5.5
NF	5.5 dB	Polarization	single

4.1.1 Physical constraints

The simulation were performed taking the device constraint into consideration. The bandwidth and the sampling frequency for this simulation were set to $B = 16 \text{ GHz}$ and $f_s = 64 \text{ GHz}$, respectively. These values are largely related to the sampling frequency and bandwidth of the available ADC at the transmitter. In addition, the linewidth of the laser were set to 1 kHz and the resolution of the DAC and ADC to 5.5 bits . The NFDM signal are designed according material constraints presented above, and the dimensioning is described in the following sun-section.

4.1.2 NFDM signal dimensioning

The linear and independent evolution of the nonlinear spectral amplitude, $\widehat{q}(\lambda)$, for each nonlinear frequency λ motivates a modulation of individual subcarriers as it is done by the OFDM. Therefore, the NFDM signal is designed and dimensioned in a similar manner as of the OFDM.

From the time duration of NFDM signal $T_s = 2 \text{ ns}$ and the sampling frequency of the AWG, $f_s = 64 \text{ GHz}$, the NFT size is calculated as:

$$\text{NFT-size} = T_s \cdot f_s = 2 \text{ ns} \cdot 64 \text{ GHz} = 128$$

In the NFDM signal, the zero-padded guard between the baseband signal and the aliasing product can be generated directly in the nonlinear frequency domain by setting the highest subcarriers to zero. The remaining subcarriers, the data subcarriers N_{sc} , are related to the total useful bandwidth, B , by:

$$N_{sc} = T_s \cdot B = 2 \text{ ns} \cdot 16 \text{ GHz} = 32.$$

4.2. Intrinsic physical challenges

The nominal data rate carried out per polarization taking into account the possible overheads can be expressed as:

$$R_{\text{nom}} = \frac{N_{sc} \cdot \log_2(M)}{T_s} = \frac{32 \cdot \log_2(16)}{2 \text{ ns}} = 64 \text{ Gbps}$$

The guard-interval (GI) between the NFDM symbols is estimated by

$$T_{\text{GI}} \approx 2\pi B\beta_2 L + 3D_p\sqrt{L} \approx 3.6435 \text{ ns} \rightarrow 4 \text{ ns}$$

The total pulse duration is $T_0 = T_s + T_{\text{GI}} = 10 \text{ ns}$. Finally, each NFDM frame has 100 successive NFDM symbols that results a data structure of a 32×100 matrix.

4.2 Intrinsic physical challenges

The NLS equation (1.17) governing the evolution of an optical pulse in a fiber link is fully integrable in the absence of loss, noise, and high-order dispersion and nonlinear terms. However, the real fiber-optic channel is perturbed both by fiber loss and noise added by an optical amplifiers. In the following section, the analysis of noise and loss dominated channel models will be analyzed separately.

4.2.1 Noisy channel

The propagation of the noisy optical signal over a lossless fiber channel is modeled using the stochastic NLS equation that reads [60],[1]:

$$i \frac{\partial q(z, \tau)}{\partial z} = \frac{\partial^2 q(z, \tau)}{\partial \tau^2} - 2s|q(z, t)|^2 q(z, \tau) + n(z, \tau) \quad (4.2)$$

where $n(z, \tau)$ represents ASE noise added by the amplifier stage. The ASE noise is generated by spontaneous decay of electrons from the upper energy levels to lower energy levels in the EDFA. This results in the emission of photons in a wide frequency range. ASE noise with power spectral density of N_{ASE} is accumulated over a fiber span length of L_s . Here, Eq.(4.2) is considered as a weak perturbation of the NLSE, and it breaks the integrability of Eq.(1.17). To study the influence of noise on the evolution of the nonlinear spectral amplitudes, one can model the field evolution as proposed in [120], [121]:

$$\tilde{q}(z, \lambda) = \tilde{q}(0, \lambda) \cdot \exp(4i\lambda^2 z) + \eta(z, \lambda) \quad (4.3)$$

where $\eta(z, \lambda)$ is noise added to the continuous spectrum in the NFT domain, and it is assumed as circularly symmetric Gaussian process. Based on a perturbation analysis, Iman Tavakkolnia *et al.* have shown that ASE noise has a zero-mean value, i.e. $\mathbb{E}\{\widehat{q}(z, \lambda)\} = \widehat{q}(0, \lambda) \cdot \exp(4i\lambda^2 z)$, that translates simply into $\mathbb{E}\{n(z, t)\} = 0$ [120] (i.e., here $\mathbb{E}\{\cdot\}$ stand for the expectation operator). Moreover, the second-order statistics of the noise suggest that the noise in the NFT domain depends on the initial spectral amplitude value, $\mathbb{E}\{|\eta(z, \lambda)|^2\} = f[|\widehat{q}(0, \lambda)|]$, with order of $2 + 8\pi z/c$ and the power spectral density of noise grows nonlinearly with the power of the input spectral amplitude (see Eq.(6)[121] and Eq.(17)[120]). Therefore, noise in the nonlinear spectral domain is regarded as being non-Gaussian in distribution and dependent on signal in order of larger than 2.

4.2.2 Gaussian pulse propagation in a noisy fiber channel

Let us investigate the input spectral amplitude dependence of noise in the NFT domain. Here, the continuous spectrum of an isolated Gaussian pulse is transmitted over an amplified optical channel either with a noise or noise-free setting, as shown in Fig.(4.2). In noisy transmission, Gaussian pulses with different amplitude values are added to a broad-band optical noise, i.e., ASE noise. The continuous spectrum of the Gaussian pulse at the receiver is compared before and after transmission for the case of either noisy or noise-free fiber transmissions.

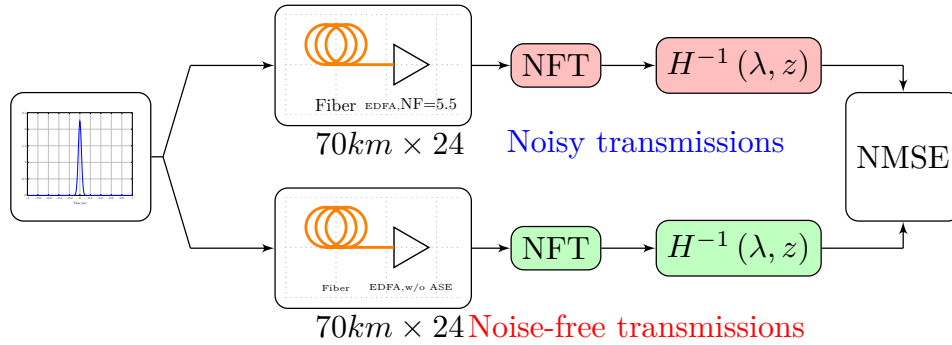


Figure 4.2: The numerical study schematic diagram of an noiseless and noisy evolution of the continuous spectrum over fiber channel.

The simulation results show that the continuous spectrum of the Gaussian pulse at a higher amplitudes is affected more by noise, when compared with the case of lower power values. Fig.(4.3) demonstrates that the continuous

4.2. Intrinsic physical challenges

spectral amplitude is distorted, as more noise is added in the NFT domain, when compared with noiseless B2B spectral shape.

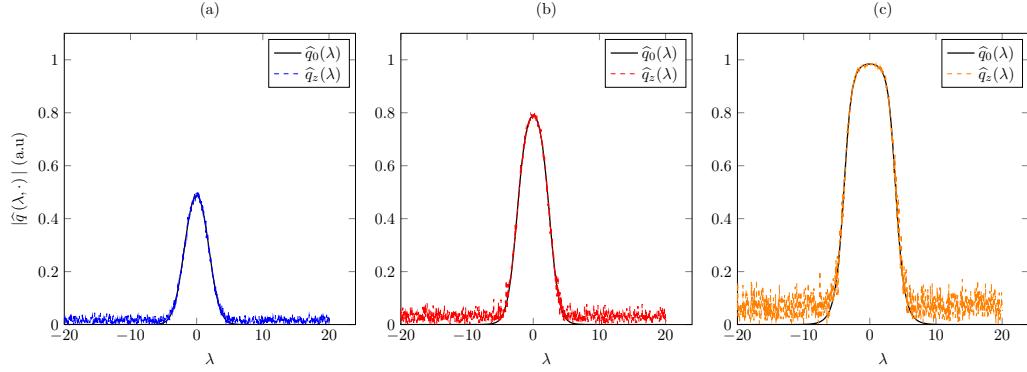


Figure 4.3: The ideal and noise loaded nonlinear spectrum of a Gaussian input with launch power $P_0 = -8, -5$, & -2 dBm. The amount of noise in the nonlinear spectral domain is proportional to the initial spectral amplitude.

4.2.3 Transmission of a 16QAM NFDM signal

4.2.3.1 Back-to-back performance NFDM in the presence of noise

A back-to-back (B2B) performance analysis was first conducted by connecting the transmitter to the receiver, based on the simulation model shown in Fig.(4.1). A 16 GHz NFDM signal modulated by a 16-QAM format is transmitted over a fiber channel with added ASE noise from EDFAs with a NF of 5.5 dB. The difference between the continuous spectrum of NFDM symbols before and after transmission is measured as a function of the optical signal-to-noise ratio (OSNR) by using the NMSE, and which is defined as

$$\text{NMSE} = \frac{\langle |\widehat{q}_{int}(\lambda) - \widehat{q}_{est}(\lambda)|^2 \rangle}{\langle |\widehat{q}_{int}(\lambda)|^2 \rangle} \quad (4.4)$$

where \widehat{q}_{int} and $\widehat{q}_{est}(\lambda)$ stand for the initial and the noise loaded nonlinear spectrum, respectively. The averaging ($\langle \cdot \rangle$) is performed over the entire nonlinear frequency (λ) grid. Here, the OSNR value of the NFDM signal is computed as the ASE noise power is varied from 10 dB to 40 dB, while keeping the power of the NFDM signal fixed, e.g. -8 dBm, -5 dBm and -2 dBm.

The B2B NMSE versus the OSNR curves of the continuous spectrum for NFDM symbols with different input launch powers is shown in Fig.(4.4). The results show that the accumulated noise-induced performance degradation becomes significant for relatively high-power NFDM signals, when compared

with lower power NFDM signals. In the low power regime, the nonlinear spectral amplitude matching increase with the signal power increment, i.e., higher OSNR value deliver better spectral matching as shown in Fig.(4.4) for NFDM signal with a signal power of $P_0 = -8$ dBm and $P_0 = -8$ dBm. For higher power signal, the spectral matching worsens as the LPA approximation becomes less accurate. Moreover, such penalties are a result of error introduced during the computation of the nonlinear spectral amplitude by using the NFT in the NFDM receiver. The ZSSP solution of the noisy received signal by using the NFT results a propagating noise in each discretization step. Therefore, the accumulated noise in the NFT block results a corrupted information decoding at the NFDM decoder. Furthermore, the higher amplitude nonlinear spectrum will be affected more by an increased signal-noise interaction. Therefore, it is quite straight forward to draw a comparison between the analytic asymptotic expression Eq.(4.3) which suggest that the noise is input signal dependent, and the simulation result in Fig.(4.4) (for more informations, refer to [121] and [120]).

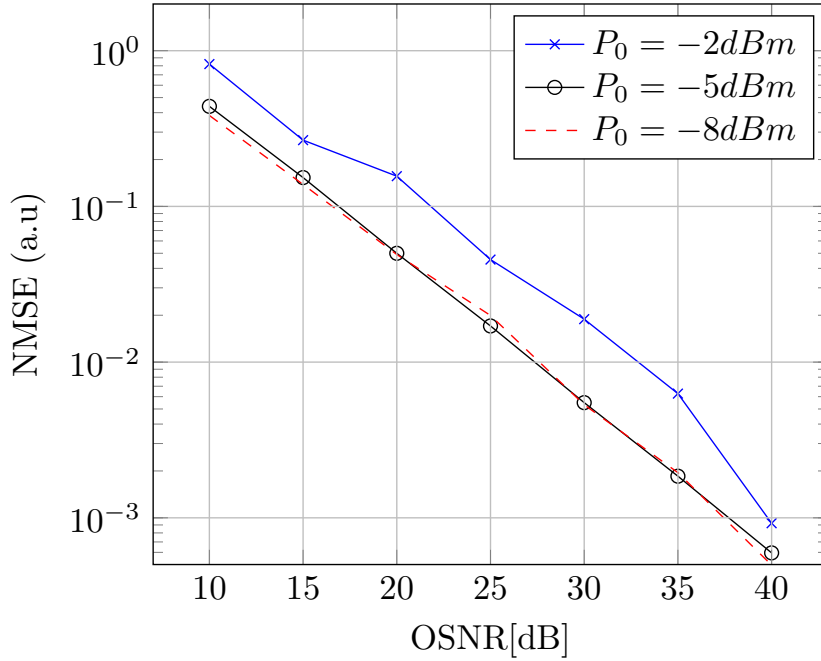


Figure 4.4: NMSE between different nonlinear spectral amplitude $\hat{q}(\lambda)$ with an input power of $P_0 = -8, -5$, & -2 dB as a function of the OSNR with $B_{opt}=0.1$ nm.

4.2. Intrinsic physical challenges

4.2.3.2 Transmission analysis

In this simulation, the NFDM signal is designed according to the simulation setup with parameters given in Table (4.1). The NFDM optical signal with a temporal duration of 12 ns is transmitted over a 1680 km TW-SRS fiber with parameters given in Table 4.2, and an EDFA which is required to exactly compensate for the fiber span loss.

In Fig.(4.5) the input and the output continuous spectral amplitude of a single NFDM symbol in the cases of either noise-free, Fig.(4.5(a)), or noisy, Fig.(4.5(b)), fiber transmission, is presented. The simulation results suggest that the noise effect in the NFT domain is not simply that of an additive noise. As a result, the NFDM signal turns out to be very sensitive to noise when compared with its linear counterpart, i.e., OFDM signal. Similarly, Fig.(4.6) shows the constellation diagram after a fiber propagation in the case of a noise-free and noisy channel.

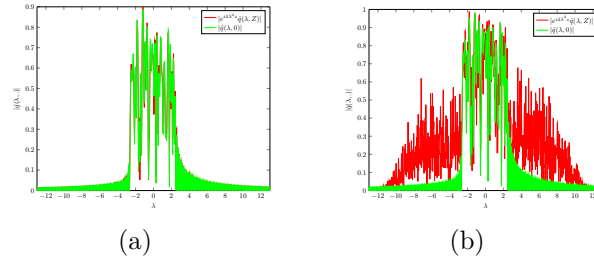


Figure 4.5: Illustration of the NFDM transmission performance in a noisy and noise free transmissions. The input and output continuous spectral amplitude $\tilde{q}(\cdot, \lambda)$ is shown here in the case of: (a) a noise free, and (b) a noisy optical link,

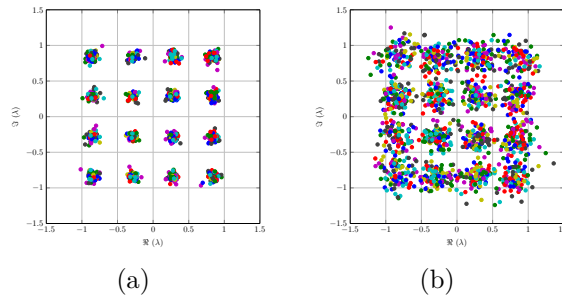


Figure 4.6: Constellation of NFDM transmission (a) without ASE noise, (b) with ASE noise.

This observation is supported by computing the Q-factor performance as a function of the input launch power, as shown in Fig.(4.7). Note that, because of ASE and numerical noise, in the computation of the NFT/INFT it may occur that $|\hat{q}(\lambda)| > 1$ [127]. This phenomenon are generally attributed to a solitonic component generation by noise [126]. Fig.(4.7) shows the Q-factor from a noise-free (red) and noisy (blue), from guard interval of 4 ns. The Authors of [127] have observed, in the lower input power region, the performance of the noise-free curve present a huge gap when compared with the noisy transmission curve. The noise-free curve falls sharply at the highest end of the power scale. This is because of the following few reasons:

- * The INFT is intrinsically a solution to ill-posed problem, which is a general property of all inverse scattering problems. The inverse NFT attempts at recovering the potential that has generated a given non-linear spectrum. Physically, one can see the origin of this ill-posed problem by considering that the Zakharov-Shabat problem describes a linear chirped fiber Bragg grating. In this case, solving the INFT leads to the synthesis of the chirp profile (potential) that generates a target complex grating transmission (nonlinear spectrum) [128]-[131].

Now, as the grating transmission amplitude approaches unity, this means that light is fully reflected by the grating. Then, there is not sufficient information in the grating transmission to uniquely determine the chirp profile inside the grating, since no light penetrates in it. In the context of the NFDM technique for communications, at the non-linearity gets larger, any numerical solution to this ill-posed problem will be subject to the growth of spurious solutions which unavoidably mask the true solution. Therefore, appropriate regularization procedures should be developed in the future, if one want to increase the range of stability of digital signal processing techniques implementing the INFT.

- * The extra Q-factor penalty in the fiber transmission is attributed to the error in the lossless path averaging (LPA) approximation model.
- * Due to inherit property of the numerical method used to compute the NFT/INFT, the NFDM signal generated have undesirable tail at a high power values. An appropriate amount of GI is used to accommodate the broadening. The longer GI, the more ASE noise added to the NFT process. Therefore, a signal-noise interaction also linked to such performance degradation.

4.2. Intrinsic physical challenges

On the other hand, the performance of the noisy NFDM transmission increase as a function of the input power as one might expect. However, after reaching an optimal performance value, the performance fall down as the contribution from ASE noise increase with input power [127]. The performance penalty demonstrate the impact of numerical accuracy, boundary conditions, discretizations, accuracy of the LPA model, etc. [127].

It is also shown in Fig.(4.7) the performance a noise-free NFDM transmission with a reduced guard interval, i.e., 2 ns. Here, a reduced value of a guard interval is used to speed up the NFT computation. The Q-factor performance remains constant in the lower input power region as the numerical accuracy is sufficient, i.e., at a lower power value the NFDM do not have a tail. However, once past the optimal power, the Q-factor performance curve fall down for the same reason mentioned above.

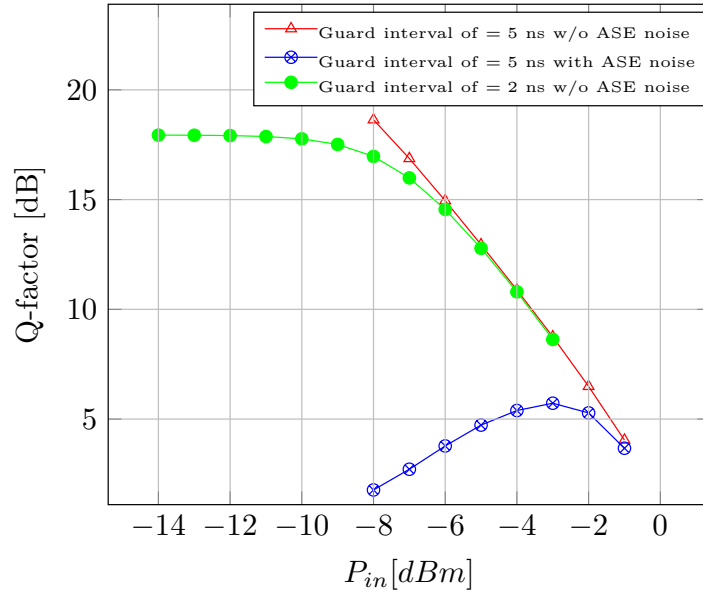


Figure 4.7: Q-factor performance as a function of input launch power for NFDM transmission system with and without ASE noise.

It is clear that noise is limiting the performance of the NFDM transmission. So, to improve the NFDM system performance understanding the noise behavior and modeling it is crucial. Such understanding should help mitigate the noise, evaluate the NFDM channel capacity, and optimize the performance of the NFDM transmissions.

4.2.4 Lossy channel

In long-haul optical communications, in order to overcome the fiber loss the optical signals need to be amplified periodically so that the signal amplitude is restored to the initial value. Two different approaches exist: the so called lumped and distributed amplification schemes have been used as it was pointed out in chapter 1. Let us consider a periodically amplified noise-free transmission system in which the optical link is divided among N -number of fiber spans with a length of $L_s[km]$, and all amplifiers have a constant gain. The master evolution equation with a gain-loss profile $\Gamma(z)$ term is defined as [122]:

$$i \frac{\partial q(z, t)}{\partial z} = \frac{\beta_2}{2} \frac{\partial^2 q(z, t)}{\partial \tau^2} - \gamma |q(z, t)|^2 q(z, t) + i \Gamma(z) q(z, t) \quad (4.5)$$

where

$$\Gamma(z) = i\alpha + i(e^{\alpha L_s} - 1) \times \sum_{n=1}^N \delta(z - nL_s) \quad (4.6)$$

and N is the total number of amplifiers. Eq.(4.5) is non-integrable equation, i.e., the NFT cannot provide an exact analytic solution. Integrability can be restored by introducing a simple change of variables:

$$q(z, t) = \exp\left(-\frac{\alpha}{2}z\right) Q(z, t). \quad (4.7)$$

which is common in the guiding-center soliton theory [123]. The Eq.(4.5) can be expressed in the following way:

$$i \frac{\partial Q(z, t)}{\partial z} - \frac{\beta_2}{2} \frac{\partial^2 Q(z, t)}{\partial \tau^2} + \gamma(z) \exp(-\alpha z) |Q(z, t)|^2 Q(z, t) = 0. \quad (4.8)$$

where the distance dependent nonlinear parameter can be replaced with its average equivalent $\bar{\gamma}$ evaluated over the span length (L_s) as

$$\bar{\gamma} = \frac{1}{L_s} \int_0^{L_s} \gamma \exp(-\alpha z) dz = \gamma \frac{G - 1}{G \ln(G)} \quad (4.9)$$

Here, $G = \exp(\alpha L_s)$ is the gain parameter [1]. It is convenient to rewrite Eq.(4.5) as an equation that closely approximates the lossless NLSE (1.17). This is known as the lossless path averaging (**LPA**) model of the NLSE, which reads as

$$i \frac{\partial Q(z, t)}{\partial z} - \frac{\beta_2}{2} \frac{\partial^2 Q(z, t)}{\partial \tau^2} - \bar{\gamma} |Q(z, t)|^2 Q(z, t) = 0 \quad (4.10)$$

Note that Eq.(4.10) is a lossless approximation of a lossy system with variable gain-loss profile, and the NFT solution is closer to the ideal solution of (4.10) asymptotically.

4.2. Intrinsic physical challenges

4.2.4.1 Transmission performance of loss for Gaussian pulse

Fig.(4.8) depicts the transmission numerical simulation the influence that fiber losses have on the continuous spectrum by using a 1680 km fiber transmission link. The transmitter generated an isolated Gaussian pulse with the full-width half-maximum (FWHM) duration of 50 ps and the total duration of 8 ns. The loop consist of a 24×70 km TW-SRS fiber with either $\alpha = 0$ dB/km or $\alpha = 0.2$ dB/km fiber loss coefficient. The link is amplified periodically after each span by using the EDFAs, and ASE noise is neglected. The fiber is assumed to have dispersion $D = 4.06\text{ps/nm-km}$ and nonlinear coefficient $\gamma = 1.27\text{W}^{-1}\text{km}^{-1}$.

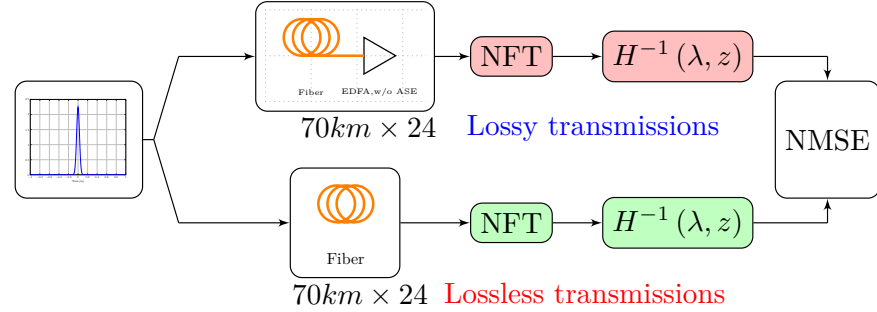


Figure 4.8: Numerical simulation model of a periodically amplified lossy channel and an ideal lossless channel.

The continuous spectrum $\widehat{q}_{in}(\lambda)$ and $\widehat{q}_{est}(\lambda)$ are computed by using the NFT of the input $q_0(t)$ and output $q_z(t)$ after the fiber link, respectively. In the case of a lossy channel, the signal is amplified by using EDFAs in order to compute the NFT with the LPA approach. The channel effect is reversed by using a one-tap equalizer, and the NMSE value is computed between $\widehat{q}_{in}(\lambda)$ and $\widehat{q}_{est}(\lambda)$. In the lossless case, the NFT continuous spectrum shape is preserved, unlike the lossy transmission case, as shown in Fig.(4.9). Therefore, the NFT performs worse in the lossy case when compared with the lossless case, due to the approximation error in the LPA model used to compute the NFT when the channel is lossy and non-integrable.

4.2.4.2 Transmission performance of loss for NFDM transmission

In this simulation, the NFDM signal is transmitted over 1680km noise-free optical channel either with a loss or lossless setting. For the lossy channel, the transmission loss is compensated by using a noise-free EDFAs after each span and the LPA model is used. At the fiber output, the coherent NFDM receiver decodes the information and computes the Q-factor performance.

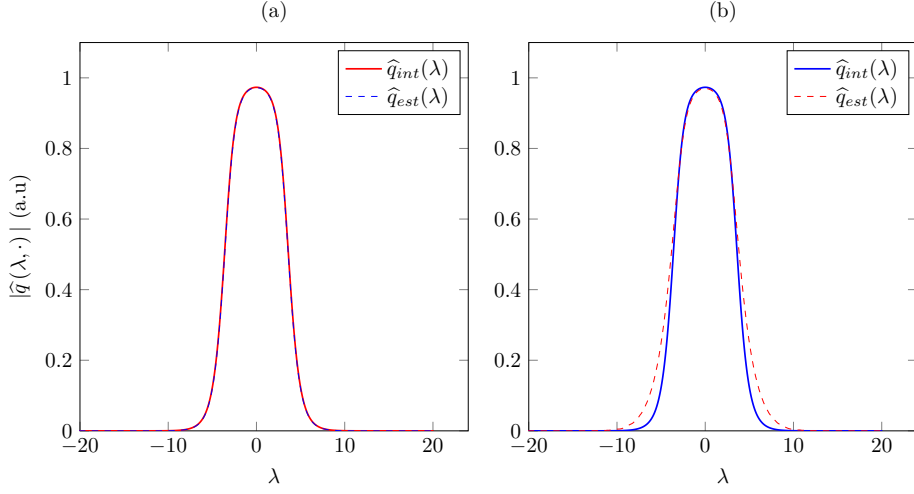


Figure 4.9: The NFT continuous spectrum of a lossless and lossy transmission where the later approximated by the LPA method.

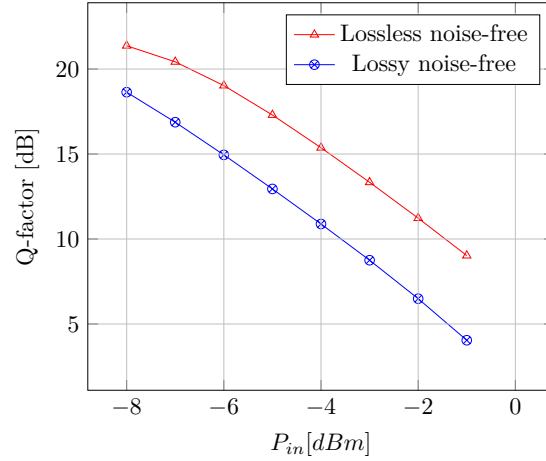


Figure 4.10: Q-factor performance vs an input power for a lossless and a lossy noise-free fiber transmission over 1680km.

In Fig.(4.10) the Q-factor performance as a function of the launched input signal power is shown. The simulation result demonstrates that at low input power the lossy transmission with approximated integrable model, i.e., the LPA model, shows ~ 3 dB penalty, while at high input power the penalty becomes in the order of ~ 5 dB. Such deviation is because of the fact that the LPA model break down at high powers and the channel is non-integrable. The Q-factor performance penalty increases with the power, consistently with the B2B results.

4.3 Optical challenges

4.3.1 Frequency Offset and Laser Phase Noise

The impact of carrier frequency offset and laser phase noise on the NFDM system is investigated using a similar setup as shown in Fig.(4.1). From the frequency and phase shift property of NFT:

$$\begin{aligned} q(t) e^{-2i\omega t} &\xrightarrow{\text{NFT}} \widehat{q}(\lambda - \omega) \\ q(t) e^{i\phi} &\xrightarrow{\text{NFT}} e^{-i\phi} \widehat{q}(\lambda) \end{aligned} \quad (4.11)$$

a carrier frequency shift between the optical carrier and the local oscillator (LO) induces a frequency shift on the eigenvalues, and a constant phase rotation ϕ in time domain will introduce a negative phase rotation on the received nonlinear spectrum.

The NFDM symbol at the receiver can be expressed as follows:

$$R(t) = [q(z = L, t) e^{i\Delta\omega t}] e^{i\phi_n}. \quad (4.12)$$

Assuming a perfect synchronization and supposing that the NFT block processes the received signal, the continuous spectral amplitude after 1-tap channel equalizer is expressed as

$$\widehat{q}_{eq}(z, \lambda) = \widehat{q}(0, \lambda - \omega) e^{-i4\lambda z} e^{-i\phi_n} \quad (4.13)$$

Eq.(4.13) shows that the nonlinear spectral amplitude with a frequency offset ω exhibits a common phase rotation ϕ_0 and irreducible phase noise $\Delta\phi_n$ due to the nonlinear phase noise ϕ_n . The following transmission performance analysis demonstrates this.

4.3.2 Transmission analysis of laser phase noise penalty

In the simulation architecture presented in Fig.(4.1), an ECL with variable linewidth from 0 k Hz to 1 MHz is introduced for NFDM transmission over an optical link of either 840 km or 1680 km, respectively. Pilot sub-carriers/tones are widely used to characterize the laser phase noise at the RX. In this thesis work, pilot tones are embedded in the nonlinear frequency domain and retrieved after transmission. This means that the phase drift between the optical carrier and the LO laser can be tracked over a number of NFDM symbols.

To investigate the impact of laser phase noise, at the transmitter signal passes through a filter $s(t) = q(0, t) \cdot \exp(i\phi(t))$, where $\phi(t)$ is the enhanced laser phase noise. The signal propagates over amplified optical links of $L = 840$ km or $L = 1680$ km reach. At the receiver, synchronization was performed, and the received signal was separated into a block of NFDM symbols before being processed by the NFT. The continuous spectrum was equalized by a 1-tap channel equalizer, and processed by using the OFDM decoder. 4-pilot tones are used to track the phase evolution before the decoder detects the symbols and computes the Q-factor values.

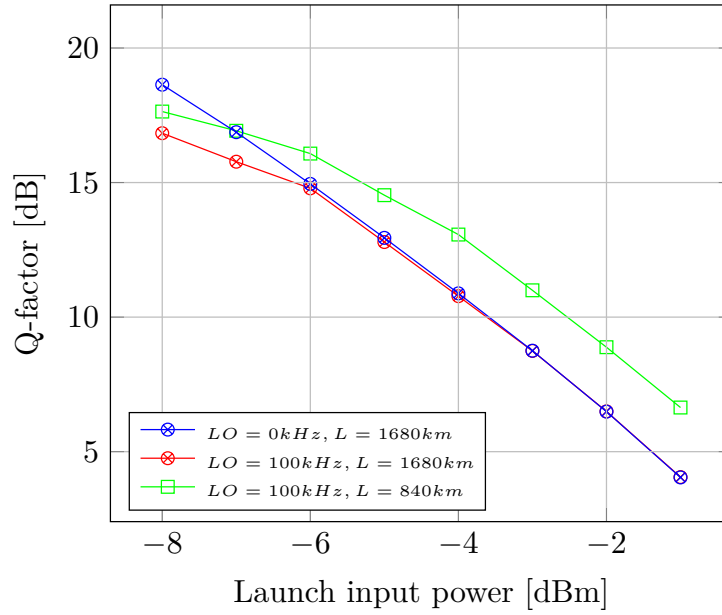


Figure 4.11: Q-factor performance of NFDM transmission over $L = 840$ km and $L = 1680$ km using laser line width of $\Delta\nu = 100$ kHz and $\Delta\nu = 0$ kHz.

The comparison of Q-factor performance (derived from the EVM value) vs the launch input power for $L = 840$ km and $L = 1680$ km optical links is shown in Fig.(4.11). At lower input powers, the performance of the two systems differ by only 0.8 dB. However, as the launch power increase, the enhanced phase noise penalty increases for long distance transmission, i.e., almost 2.6 dB penalty is observed at the launch input power of -1 dBm.

The laser phase noise (LPN)-induced performance penalties as a function of laser linewidth (LO) and for a transmission distance of 1680 km for a NFDM transmission system with a 16QAM is shown in Fig.(4.12). In Fig.(4.12), different linewidths were used in the simulation. The penalty was only 0.11,

4.3. Optical challenges

0.34 and 0.55 dB as LO linewidth changed from 1 kHz to 1 MHz for the launch input power of -1 dBm, -5 dBm and -8 dBm, respectively. With linewidths larger than 1 MHz, the performance degradation starts to be significant (> 0.5 dB). This penalty suggest that, in NFDM systems the time domain laser phase noise impacts both amplitude and phase of the nonlinear spectral amplitude $\widehat{q}(\lambda)$. Moreover, similarity can be drawn between Fig.(4.12) and Fig.(4.11) in terms of a performance penalty when using the same transmission distance for a different laser linewidth. The simulation result in Fig.(4.12) and Fig.(4.11) demonstrates that at high power the laser linewidth-induced penalty are insignificant when compared with low power inputs.

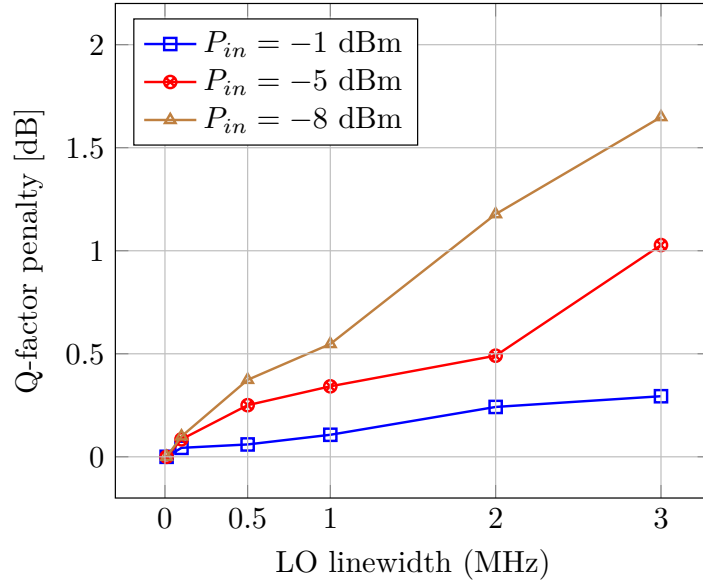


Figure 4.12: A B2B Q-factor penalties as functions of a laser linewidth for a burst launch input power of 1, -1 and -3 dBm over a 1680 km link.

Finally, the LPN penalty increase with transmission distance is shown in Fig.(4.13). The Q-factor performance significantly decreases as the distance increases: a 5 dB penalty at the transmission reach of 1960 km, when compared with the 840 km link is observed for the LO linewidth of $\Delta\nu = 100$ kHz. Moreover, compared with linewidth of $LO = 0$ kHz, the $LO = 100$ kHz shows penalty of 1 dB at 840km while this penalty decreases to only 0.2 dB at a transmission reach of 1960km. On the other hand, a significant performance degradation for the LO linewidth of 1 MHz is observed when compared with both the LO linewidth of $LO = 0$ kHz and $LO = 100$ kHz. It is apparent that,

in short range transmissions reach, the LPN penalty for the LO linewidth of 1 MHz is ~ 3.5 dB and ~ 3 dB when compared with the LO linewidth of $LO = 0$ kHz and $LO = 100$ kHz, respectively. However, the performance degradation in all cases are nearly equal when the link distance reaches the value of 1960 kms.

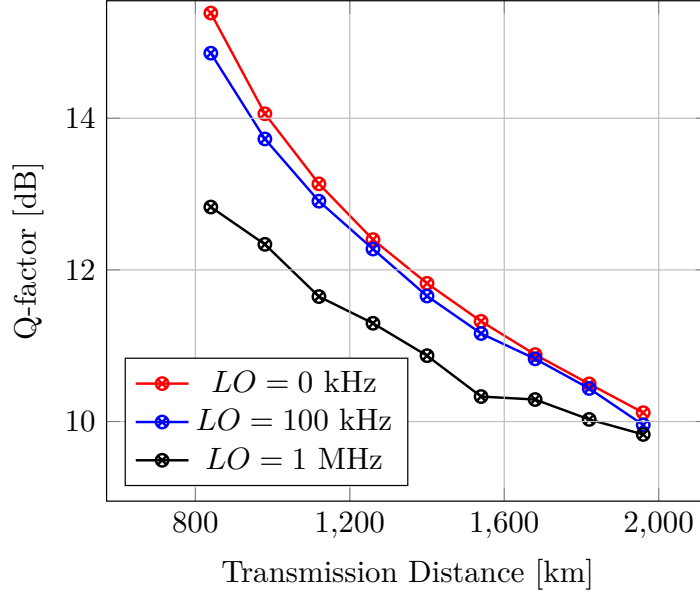


Figure 4.13: Q-factor performance versus transmission distance (no ASE noise is considered).

4.4 DSP implementation and transmission device issues

4.4.1 Guard interval and spectral efficiency

The burst-mode NFDM system is resilient to the dispersion effects by inserting a very long guard interval (GI), to prevent the inter-symbol interference (ISI). However, the large GI overhead compromises the spectral efficiency benefit of NFDM transmission, and also leads to an increased complexity in the computation of the NFFT and INFFT of the signal. In NFDM systems, dispersion effects can only be removed at the receiver in the NFFT domain, while the pulse is still broadens in the temporal-domain upon propagation. The Authors of [124] have evaluated both in a numerical study and in its experimental validation, the spectral efficiency gain in pre-compensated NFDM

as a function of a variable size GI. As per [124], the normalized spectral efficiency in symbol/s/Hz as a function of the guard interval size, taking both CD and PMD into account [124], is given as:

$$SE = \frac{T_s}{T_s + 2\pi B\beta_2 L + 3 \cdot D_p \sqrt{L}} \quad (4.14)$$

Neglecting the PMD term and using the relation $T_s = N_{sc}/B$, where N_{sc} is the number of useful subcarriers, T_s is the useful NFDM symbol duration and B is the bandwidth of the transmitted signal, Eq.(4.14) is reduced to:

$$SE = \frac{1}{1 + 2\pi B^2 \beta_2 L / N_{sc}} \quad (4.15)$$

In this section, the effect of variable GI size on NFDM systems is investigated numerically.

4.4.1.1 B2B Performance

To analyze the impact of the GI, the NFDM signal is designed with a variable GI size in a B2B configuration. At the receiver, it is essential to minimize the error associated with synchronization, CFO and the split-step Fourier method. Fig.(4.14) shows the optimal Q-factor performance of the NFDM system for different sizes of the normalized guard interval GI/T_0 , i.e. the guard interval length is normalized to the symbol duration. It can be observed that high-power NFDM symbols perform as good as low power symbols, for normalized guard intervals (NGI) from 2 to 3. However, the high power symbols performance decreases sharply for NGIs less than 1.5. This is due to the fact that, at high power, the NFDM symbol exhibits longer tails, due to its increasing energy leakage towards the decaying tails, when compared with lower power symbols. Moreover, a reduced guard interval also induces a performance penalty as a result of increasing numerical errors in the NFT-INFT computation, due to increased sample size in the nonlinear frequency domain.

4.4.1.2 Transmission Performance

The transmission performance of NFDM systems subject to variable NGI size is presented in Fig.(4.15). Here, the simulation was done for both a noise-free and a noisy amplified optical fiber channel. Fig.(4.15) shows the Q-factor performance as a function of the input launch burst power for different sizes of NGI in noise-free (thick lines) and noisy (dashed lines) transmissions.

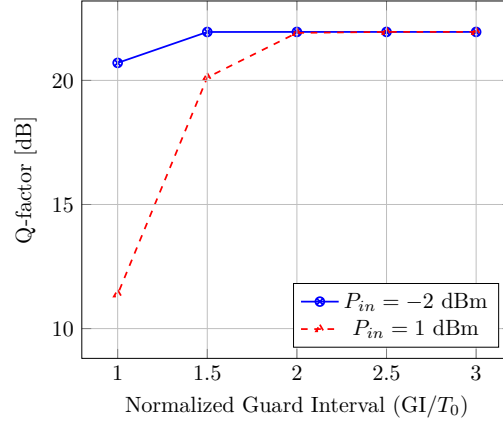


Figure 4.14: Simulation result of a B2B Q-factor performance as a function of NGI for NFDM transmissions with input power of -4 dBm and -1 dBm.

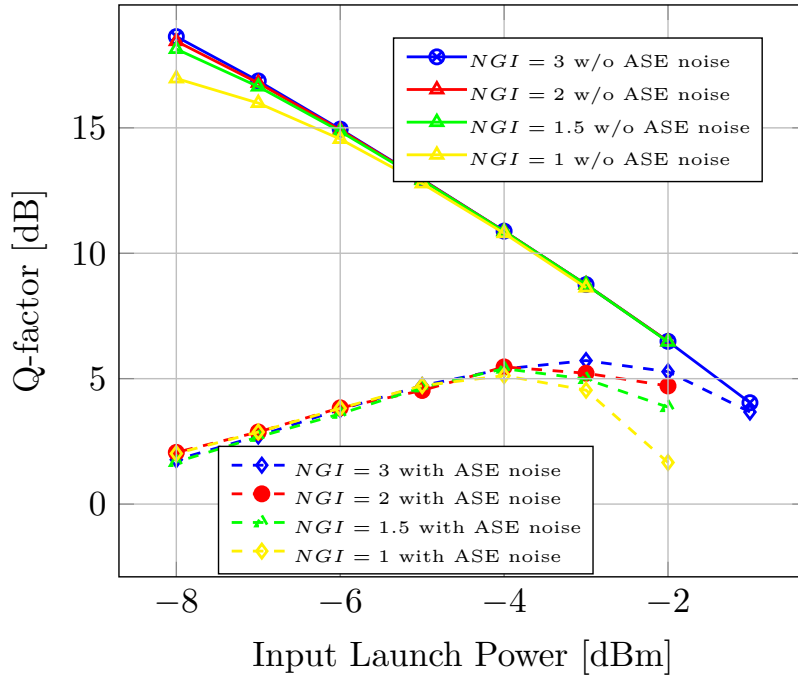


Figure 4.15: Q-factor vs burst input power for NFDM transmissions with different NGIs in a noise-free (solid lines) and noisy (dashed lines) fiber transmissions.

In Fig.(4.15), the noise-free transmission performance of a NFDM system with a short guard interval perform slightly worse when compared with a NFDM system with a longer guard intervals. This penalty is attributed

to the growth of the signal-noise interaction in the region near the lower end of the input power; moreover, the noisy performance curve fall down as the impact of ASE noise increase. The noisy transmission performance demonstrates that noise has significant impact on the NFDM transmission with a shorter NGI. Compared with NFDM transmission with $NGI = 3$, the NFDM system with $NGI = 1$ exhibits a Q-factor penalty of 3.4 dB at input burst power of -2 dBm, and a comparable performance for an input burst power lower than -4 dBm and. However, spectral efficiency will increase by a factor of 2 when compared with the NFDM transmissions with $NGI = 1$.

4.4.2 Oversampling and numerical accuracy

While the idea of using the continuous spectrum for NFDM transmissions is attractive due to analogies with OFDM, errors in the generated continuous spectrum and run-time of the NFT/INFT algorithms, make the NFDM more complex in practical implementations. This sub-section investigates the dependence of the accuracy of a NFDM system on the oversampling factor and signal power.

4.4.2.1 B2B performance

For the oversampling investigation, a NFDM system with variable oversampling factor is used. NFDM symbols in the linear spectrum are over-sampled, before mapping them to the continuous part of the nonlinear spectrum. Since the NLSE is solved by using the INFT numerically, oversampling is essential for minimizing the numerical errors associated with the information-bearing signal at the output of the INFT block, $q(0, \tau)$. The B2B noise-free performance is illustrated in the Fig.(4.16).

The performance of the NFDM transmission in Fig.(4.16) shows a significant Q-factor gain as the oversampling factor is increased from a value of 4 to a value of 32. This gain can be attributed to improved accuracy in the computation of the nonlinear spectral amplitude, as illustrated in inset of Fig.(4.16).

4.4.2.2 Transmission performance

For transmission performance investigation of the oversampling factor, an oversampling factor of 4 and 8 was used. Here, the simulation was done for both a noise-free and a noisy amplified optical fiber channel. Fig.(4.17) shows the Q-factor performance remain similar for the oversampling factor of 4 and 8. This is the main reason behind our decision to reduce the oversampling

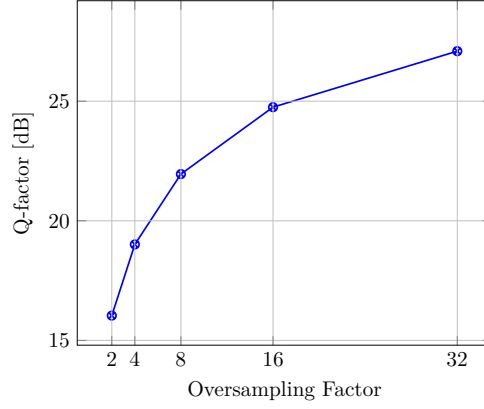


Figure 4.16: Illustration of B2B performance of the oversampling factor.

factor from 32, in single polarization first experiment, to factor of 8, in a dual polarization experimental validation.

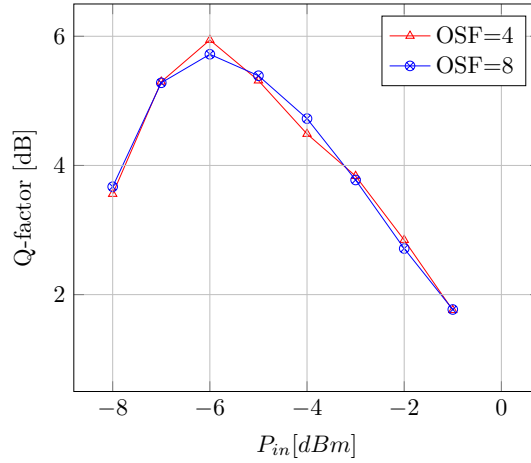


Figure 4.17: Q-factor performance as function of input launch power for the oversampling factor of 4 and 8.

4.5 Transmitter and receiver limitations

Transmitter and receiver front-end electrical components put a major limitation on the achievable performance of NFDM when compared with OFDM [105]. Commercial DACs/ADCs have very limited bandwidth and bit-resolution. As a result, there is a limit on the maximum symbol-rate which can be generated by the transmitter, since the symbol-rate and the signal bandwidth lin-

4.5. Transmitter and receiver limitations

early proportional. Moreover, the DAC also introduces a quantization noise to the digital waveform while converting it into an analog electrical signal. The quantization noise power variance, $\sigma^2 = \Delta^2/12$, depends on the step-size of DAC/ADC (Δ), which in turn depends on the number of bits supported by the device in its operational voltage range. In practice, quantization noise is further enhanced by other noise sources in the transmitter-receiver chain, ultimately leading to substantially reduced SNR values.

In practice, DACs/ADCs can be characterized in terms of their effective number of bits (ENoB) as [125]:

$$\text{ENoB} = \frac{\text{SNDR}[\text{dB}] - 1.76[\text{dB}]}{6.02} \quad (4.16)$$

where SDNR is signal to noise plus distortion ratio, which includes noise and any additional distortions to the system. In this thesis, a Keysight arbitrary-waveform generator (AWG) with sampling frequency of $f_s = 64$ GSa/s and 50 GSa/s Tektronix digital sampling oscilloscope were used at the transmitter and receiver, respectively. Although the bit resolution of the AWG is 8 bits, the maximum value of ENoB is only ~ 5.5 bits. As a result of the low ENoB, the DAC output signal has a frequency dependent distortion noise added to it. Consequently, the SNR of the NFDm signal is limited, which untimely translates into low OSNR and a limited transmission reach. In this thesis, the generation and transmission of signals with higher order multi-level modulation proved to be extremely challenging when compared to e.g. QPSK, due to their higher SNR requirements, for the same level of BER performance.

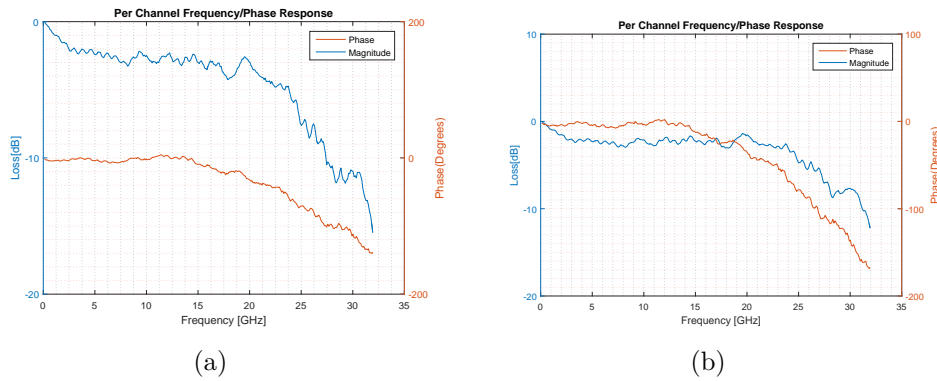


Figure 4.18: Experimentally measured DAC frequency/Phase response for the (a) I- and (b) Q-channels.

Experimental measurements of the magnitude and phase response of the DAC are presented in Fig.(4.18). Ideally, the channel response should be flat over the entire bandwidth of the signal, in order to avoid any device-induced performance degradations. Here it should be noted that, while the half power bandwidth of the amplitude spectrum is limited up to only about ~ 24 GHz, the phase response already shows a loss of -10 dB in the I-channel, while it shows negligible decay in the Q-channel. Due to this decaying response, the NFDM signal was designed to reside in the flat section of the phase response curve, i.e. ~ 16 GHz. The bandwidth limitation of DACs restricted NFDM symbol-rate around ~ 25 Gbaud.

Mitigating distortion from the transmitter-receiver chain has may increase the spectral efficiency and transmission reach. Due to the unavailability of a measurement method to effectively estimate the transfer function of each electrical component, only an amplitude pre-distortion equalization was used at the transmitter side DSP stage as shown in Fig.(4.19). Using a naive assumption that the phase response is constant over the signal bandwidth, amplitude equalization is still necessary, since high-frequency components of the NFDM signal are attenuated, due to the bandwidth narrowing of the DAC, thus leading to enhanced ISI. A full equalization should also, in addition to the DACs, take into account driver amplifiers and MZMs induced amplitude distortion.

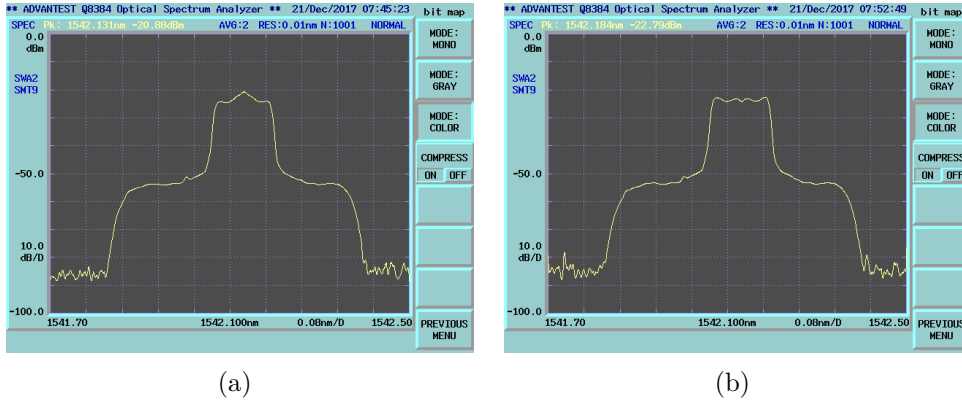


Figure 4.19: Signal spectra of the NFDM signal, (a) before and (b) after the amplitude pre-emphasis equalizer compensating for the transmitter electronics induced amplitude distortion.

4.5.1 TX and RX limitation in B2B performance

In this section, we evaluate the impact on the NFDN transmission of a limited number of bits of DACs/ADCs. Performance penalties due to a finite DAC/ADC resolution are shown in Fig.(4.20). In a B2B configuration, increasing the signal power leads to a performance degradation, due to the longer decaying tails of the NFDN signal burst. This suggest that higher DAC resolutions are required to preserve the long tails in NFDN symbols, i.e., the flat-gain region (refer to [94] for similar observations).

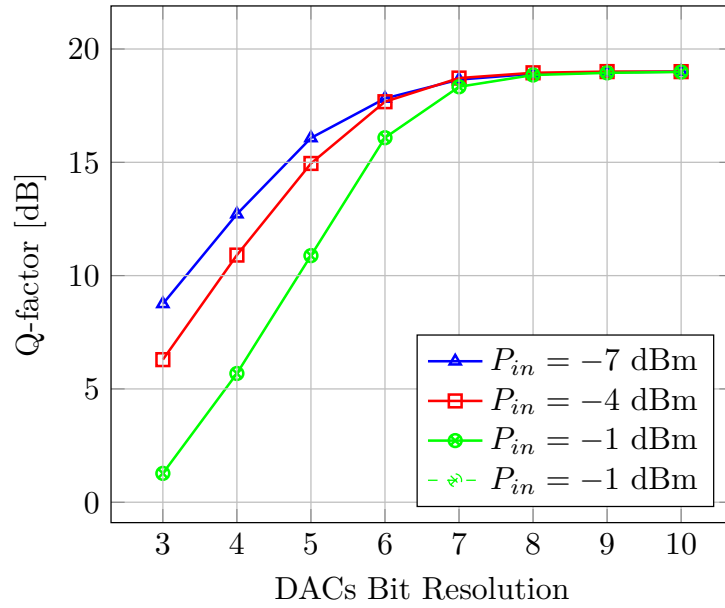


Figure 4.20: ENoB vs OSNR

4.5.2 TX and RX limitation in transmission performance

In this sub-section a simulation was performed to investigate the impact of a DAC resolution on the NFDN transmission systems. The NFDN signal was then transmitted over 70km span of TW-SRS fiber which amplified by EDFAs with NF=5.5 dB, resulting in a total distance of 1680km. In the simulation, a bit resolutions of ENoB = 3, ENoB = 5, ENoB = 6, and ENoB = 7 were used.

Fig.(4.21) show Q-factor performance versus the burst input powers, for 3-bit, 5-bits, 6-bits, and 7-bit DAC, respectively. When 5- to 7-bit DAC is

used, only slight performance improvement is observed. For a 3-bit DAC, however, the performance penalty is ~ 3.8 dB. This is expected since with a low-bit DAC, there is not enough resolution to accurately sample the non-linear spectral amplitude at the transmitter.

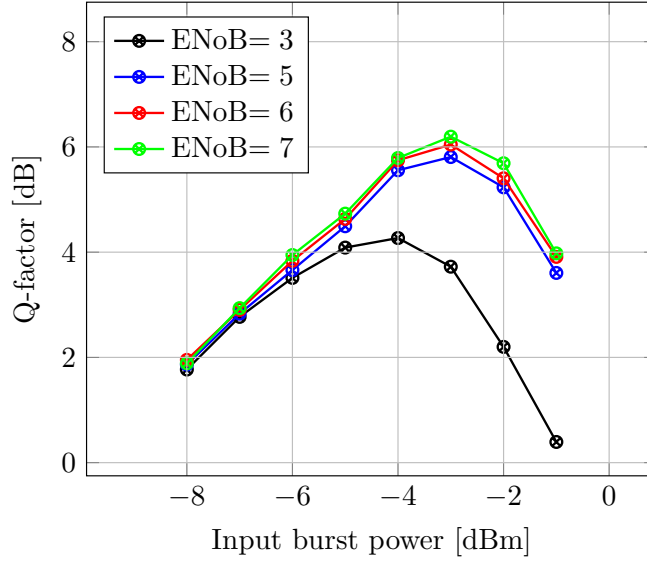


Figure 4.21: Q-factor performance as a function of the burst input power after 1680km. The DAC resolutions are 3,5,6 and 7 bits, ASE noise was added.

4.6 Summary

In this chapter, the implementation challenges of NFDM transmissions have been investigated numerically. NFDM systems suffer from significant distortions due to signal perturbations by noise and loss. Moreover, the integrable model assumption of the ideal NLSE channel is invalid in a practical scenario, which needs to be properly taken into account for NFDM to be viable system for real world implementations. Our comprehensive study of the impact of guard interval size and oversampling factor suggest the following. First, the spectral efficiency of NFDM systems can be increased by means of a suitable reduction of the guard interval [105]. Second, reducing either the guard interval or the oversampling factor results increased numerical errors in the numerical computation of the spectral amplitude by using the NFT. Unlike OFDM, NFDM symbols are uniquely characterized by a significant decaying tail as the signal power is increased which puts a tremendous pressure on the high resolution requirement of DACs/ADCs. Finally, the overall performance of NFDM systems relies on the compensation of any phase error which may arise in the transmission system, including laser phase noise. As a result, lasers with linewidth values of ≤ 1 kHz may lead to a significant performance gain in the NFDM system, compared to its linear counter part, OFDM.

4.6. Summary

Chapter 5

Conclusions and Future Work

“ You cannot hope to build a better world without improving the individuals. To that end, each of us must work for our own improvement. ”

Marie Curie,

THE motivation of this thesis is that the capacity of present single-mode fiber (SMF) coherent optical communication systems is fast getting saturated by fundamental limits. With the global data traffic increasing at an astounding 26% Compound Annual Growth Rate (CAGR), and the new machine-learning and Internet-of-Things (IoT) technologies, the research for new ways to approach the fiber capacity growth is actively being pursued in order to surpass the transmission capacity crunch. As of today, a major limitation to fiber capacity is set by the nonlinear response of the fiber channel. However, the high computational complexity imposed by state-of-the-art nonlinear equalization techniques remains a major challenge for their practical deployment. With the advent of coherent detection and high-speed digital-signal processing (DSP), novel equalization methods have been numerically analyzed and experimentally validated in the framework of this thesis for the compensation of nonlinear fiber impairments in long-haul optical transmission systems.

5.1 Conclusion

The thesis started with an overview of the optical fiber communication systems evolution, explaining its history from its beginning until present time.

5.1. Conclusion

The architectures of optical networks and their capacity evolution has also presented. Next, linear and nonlinear processes that affect signal propagation in optical fibers were described rigorously. Moreover, a detailed literature review of the methods being studied to mitigate nonlinear effects was discussed in chapter 1.

In Chapter 2, the scattering transform based on the Zakharov-Shabat spectral problem is reviewed, based on the scalar- or vector integrable nonlinear Schrödinger equation (NLSE). Using the continuous spectrum and operating in the normal dispersion regime, it was found that the numerical accuracy of the NFT-INFT algorithms increase linearly with the signal discretization sample size. Finally, a brief introduction of optical communication systems based on the NFT is presented.

The first major contribution of this thesis is presented in Chapter 3, where the NFDM system transmitter and receiver DSP architecture is proposed and described in great details. An NFDM transmission system in the normal dispersion regime and using the continuous spectrum is experimentally demonstrated for single-polarization transmission. The NFDM is then extended to polarization-division multiplexing (PDM) optical systems, and experimentally demonstrated for 16 GHz transmission systems based on 16 – QAM modulation. By these means, the NFDM method is shown to enable high performance nonlinear equalization with the same bandwidth and transmission reach, in comparison with the benchmark OFDM system. Although the normal dispersion regime allow only modulation of the continuous spectrum, the anomalous dispersion experiment has demonstrated better nonlinearity tolerance and increased the OSNR value.

Chapter Four. Using the insight from the numerical simulations and experimental validation of NFDM transmission, numerical investigation are performed, aiming at identifying the main challenges in a practical NFDM implementation. The limit of using NFDM arises from several aspects. Firstly, the non-ideal NLSE channel, which includes loss and noise, leads to significant distortion on the NFDM communication system. The channel power dependence of noise in the NFT domain sets a limitation on the achievable spectral efficiency, and by the same token also limits the transmission reach. Secondly, other sources of penalty come from the guard interval size, oversampling factor, the DAC/ADC resolution and effective number of bits (ENoBs).

5.2 Future Work

Following the research undertaken in this thesis, certain issues and challenges require further research and development. Among these we may cite:

1. Numerical implementation and optimization of emerging fast-NFT/INFT algorithms.
2. Design NFDM systems based on $b(\lambda)$ -modulation in dual-polarization configuration and perform their experimental validation.
3. Effective DSP techniques to address the complexity limitations of NFDM systems.
4. Optimize modulation formats by using techniques such as geometric or probabilistic shaping of constellations.
5. Analytical and numerical study of noise models in the NFT domain.
6. Investigate NFT based WDM transmissions based on reconfigurable optical add-and-drop multiplexer (ROADM).

5.2. Future Work

Bibliography

- [1] Govind Agrawal, *Fiber-Optic communication Systems*, John Wiley and Sons, Inc.; 3rd edition, New York (2002).
- [2] G. P. Agrawal, *Nonlinear Fiber Optics*, University of Rochester, 3rd edition, New York: Academic Press, 2001.
- [3] Chappe I. *Histoire de la télégraphie (in French)*, University of Michigan Library (1824).
- [4] T. H. Maiman, *Stimulated Optical Radiation in Ruby*, Nature, Volume 187, Issue 4736, pp. 493-494, Aug. 6, 1960.
- [5] Hecht J., *City of light: the story of fiber optics*, Oxford University Press, New York (1999).
- [6] K. C. Kao and G. A. Hockham, *Dielectric-fiber surface waveguides for optical frequencies*, Proc IEE Optoelectronics, Volume 133, Issue 3, pp. 191-198, June, 1986.
- [7] F. P. Kapron, D. B. Keck, and R. D. Maurer, *Radiation losses in glass optical waveguides*, Appl. Phys. Lett. Volume 17, Issue 423, (1970).
- [8] T. Miya, Y. Terunume, T. Hosaka, and T. Miyashita, *An ultimate low-loss single-mode fiber at 1.55 μm* , Elec. Lett., Volume 15, pp. 106108, (1979).
- [9] K. Ogawa, E. L. Chinnock, D. Gloge, P. Kaiser, S. R. Nagel, and S. J. Jang, *System experiments using 1.3 μm LEDs*, Elec. Lett., Volume 17, Issue 2, pp. 71 -72, 22 January, 1981.
- [10] R. J. S. Bates, J. D. Spalink, S. J. Butterfield, J. Lipson, C. A. Burrus, T. P. Lee and R. A. Logan, *1.3 μm /1.5 μm bidirectional WDM optical-fibre transmission system experiment at 144 Mbit/s* Elec. Lett., Volume 19, Issue 13, pp. 458-459, June 23, 1983.
- [11] J. I. Yamada, S. Machida and T. Kimura, *2 Gbit/s optical transmission experiments at 1.3 μm with 44 km single-mode fibre*, Elec. Lett., Volume 17, Issue 13, pp.479 - 480, June 25, 1981.

- [12] B. L. Kasper, R. A. Linke, K. L. Walker, L. G. Cohen, T. L. Koch, T. J. Bridges, E. G. Burkhardt, R. A. Logan, R. W. Dawson, and J. C. Campbell, *A 130-km transmission experiment at 2 Gb/s using silica-core fiber and a vapor phase transported DFB laser*, ECOC, Stuttgart, W. Germany, Sept. 1984.
- [13] J. Hecht, *The Evolution of Optical Amplifiers*, Optics & Photonics News, Volume 13, Issue 8, pp.36-39, August 2002.
- [14] E. Desurvire, J. R. Simpson, and P. C. Becker, *High-gain erbium-doped traveling-wave fiber amplifier*, Opt. Lett., Volume 12, Issue 11, pp. 888-890 (1987)
- [15] R. J. Mears, L. Reekie, I. M. Jauncey, and D. N. Payne, *Low-noise erbium-doped fibre amplifier operating at 1.54 μ m*, Elec. Lett., Volume 23, Issue 19, pp.1026-1028 (1987).
- [16] A. Durécu-Legrand, C. Simonneau, D. Bayart, A. Mussot, T. Sylvestre, E. Lantz, and H. Maillotte, *Impact of Pump OSNR on Noise Figure for Fiber-Optical Parametric Amplifiers*, IEEE Photonics Technol. Lett., Volume 17, Issue 6, pp.1178-1180, June, 2005.
- [17] F. Forghieri, R. W. Tkach, and A. R. Chraplyvy, *Fiber nonlinearities and their impact on transmission systems*, Optical Fiber Telecommunications IIIA, I. Kaminow and T. Koch (eds.), Academic Press, ch. 7, pp. 196-264 (1997).
- [18] A. R. Chraplyvy, R. W. Tkach, and K. L. Walker, *Optical fiber for wavelength division multiplexing*, U. S. Patent 5,327,516 (1994).
- [19] A. R. Chraplyvy, A. H. Gnauck, R. W. Tkach, and R. M. Derosier, *8 \times 10 Gb/s transmission through 280 km of dispersion-managed fiber*, IEEE Photonics Technol. Lett., Volume 5, Issue 10, pp.1233-1235 (1993).
- [20] R. W. Tkach, R. M. Derosier, A. H. Gnauck, A. M. Vengsarkar, D. W. Peckham, J. L. Zyskind, J. W. Sulhoff, and A. R. Chraplyvy, *Transmission of eight 20-Gb/s channels over 232 km of conventional singlemode fiber*, IEEE Photonics Technol. Lett., Volume 7, Issue 11, pp.1369-1371 (1995).
- [21] R.-J. Essiambre, P. J. Winzer, and D. F. Grosz, *Impact of DCF properties in system design in Fiber Based Dispersion Compensation*, S. Ramachandran (ed.), Springer, ch. 12, pp.425-496 (2007).
- [22] A. M. Vengsarkar, A. E. Miler, and W. A. Reed, *Highly efficient single-mode fiber for broadband dispersion compensation*, Proc. Optical Fiber Comm. Conf. (OFC), PD-13 (1993).

-
- [23] A. M. Vengsarkar, A. E. Miller, M. Haner, A. H. Gnauck, W. A. Reed, and K. L. Walker, *Fundamental-mode dispersion-compensating fibers: Design considerations and experiments*, Proc. Optical Fiber Comm. Conf. (OFC), ThK2 (1994).
- [24] Nortel launches first 10 Gbit/s transmission system in Asia, On-line: <https://www.hpcwire.com/1997/06/13/nortel-launches-first-10-gbits-transmission-system-in-asia/> (1997).
- [25] P. Trischitta, M. Colas, M. Green, G. Wuzniak, and J. Arena, *The TAT-12/13 cable network*, IEEE Commun. Mag., Volume 34, Issue 2, pp.2428 (1996).
- [26] A. H. Gnauck, R. W. Tkach, A. R. Chraplyvy, and T. Li, *High-capacity optical transmission systems*, J. Lightwave Technol., Volume 26, Issue 9, pp.10321045 (2008).
- [27] C. E. Shannon, *A mathematical theory of communication*, Bell Syst. Tech. J., vol. 27, pp. 379-423 and 623-656, (1948).
- [28] R.-J. Essiambre, G. Kramer, P. J. Winzer, G. J. Foschini, and B. Goebel, *Capacity limits of optical fiber networks*, J. Lightwave Technol., Volume 28, Issue 4, pp.662701 (2010).
- [29] R.-J. Essiambre and R. W. Tkach, *Capacity Trends and Limits of Optical Communication Networks*, Proc. IEEE, Volume 100, Issue 5, pp.10351055 (2012).
- [30] N. J. Frigo, P. P. Iannone, and K. C. Reichmann, *A View of Fiber to the Home Economics*, IEEE Commun. Mag., Volume. 42, Issue 8, pp. S16S23, Aug. 2004.
- [31] T. Koonen, *Fiber to the Home/Fiber to the Premesis: What, Where and When?* Proc. IEEE, Volume 94, Issue 5, pp. 911934, May 2006.
- [32] Cisco, *Cisco Visual Networking Index: Forecast and Methodology, 20162021*, September 15, 2017.
- [33] K. Hill and G. Meltz, *Fiber Bragg grating technology fundamentals and overview*, J. of Lightwave Tech., Volume 15, Issue 8, pp.12631276, 1997.
- [34] I. P. Kaminov, T. Li, and A. E. Willner, *Optical fiber telecommunications V A: Components and subsystems*, Academic Press, San Diego, 2008.
- [35] K. P. Ho, *Phase-Modulated Optical Communication Systems*, Springer; 1st edition, 2005.

Bibliography

- [36] S. J. Savory, *Compensation of fiber impairments in digital coherent systems*, 34th European Conference on Optical Communication, 2008.
- [37] A. H. Gnauck, R. W. Tkach, A. R. Chraplyvy, and T. Li, *High-capacity optical transmission systems*, J. of Lightwave Tech., Volume 26, Issue 9, pp.10321045, 2008.
- [38] R. Olshansky, *Noise figure for erbium-doped optical fibre amplifiers*, Electronics Letters, Volume 24, Issue 22, pp.13631365, 1988.
- [39] I. T. Lima, Jr., A. O. Lima, Y. Sun, H. Jiao, J. Zweck, C. R. Menyuk, and G. M. Carte, *A Receiver Model for Optical Fiber Communication Systems With Arbitrarily Polarized Noise*, J. of Lightwave Tech., Volume 23, Issue 3, pp.14781490, 2005.
- [40] Alper Demir, *Noise Analysis for Optical Fiber Communication Systems*, IC-CAD03, November 11-13, 2003, San Jose, California, USA.
- [41] A. Hasegawa, *Numerical study of optical soliton transmission amplified periodically by the stimulated Raman process*, Appl. Opt., Volume 23, Issue 19, pp. 3302, 1984.
- [42] C. R. Menyuk, *Application of multiple-length-scale methods to the study of optical fiber transmission*, Journal of Engineering Mathematics, Volume 36, pp. 113-136, 1999.
- [43] S. V. Manakov, *On the theory of two-dimensional stationary self-focusing of electromagnetic waves*, Soviet Physics-JETP, Volume 38, Issue 2, pp. 248253, Aug. 1974.
- [44] R. Dar and P.-J. Winzer, *Nonlinear interference mitigation: Methods and potential gain*, J. Lightwave Tech., Volume 35, Issue 4, pp. 903930, Feb. 2017.
- [45] P.-J. Winzer, D. T. Neilson, and A. R. Chraplyvy, *Fiber-optic transmission and networking: the previous 20 and the next 20 years*, Opt. Express 26, Issue 18, pp.2419024239, Sept. 3, 2018.
- [46] T. Fehenberger, A. Alvarado, G. Böcherer, and N. Hanik, *On Probabilistic Shaping of Quadrature Amplitude Modulation for the Nonlinear Fiber Channel*, arXiv:1606.04073v2 [cs.IT], 28 Jul 2016.
- [47] P. P. Mitra and J. B. Stark, *Nonlinear limits to the information capacity of optical fiber communications*, Nature, Volume 411, Issue 6841, pp.10271030 (2001).

-
- [48] P. Poggiolini, G. Bosco, A. Carena, V. Curri, Y. Jiang, F. Forghieri, *The GN-Model of Fiber Non-Linear Propagation and its Applications*, J. Lightw. Tech., Volume 32, Issue 4, pp. 694-721, Feb.15, 2014.
- [49] D. Rafique, *Fiber nonlinearity compensation: commercial applications and complexity analysis*, J. of Lightwave Tech., Volume 34, Issue 2, pp. 544-553, 2016.
- [50] A. Yariv, D. Fekete, and D. M. Pepper, *Compensation for channel dispersion by nonlinear optical phase conjugation*, Optics Letters, Volume 4, Issue 2, pp.525-4, 1979.
- [51] S. Kumar and D. Yang, *Optical backpropagation for fiber-optic communications using highly nonlinear fibers*, Optics Letters, Volume 36, Issue 7, pp.1038-1040, 2011.
- [52] K. V. Peddanarappagari and M. Brandt-Pearce, *Volterra series transfer function of single-mode fibers*, J. of Lightwave Tech., Volume 15, Issue 12, pp.2232-2241, 1997.
- [53] E. Ip and J. M. Kahn, *Compensation of Dispersion and Nonlinear Impairments Using Digital Backpropagation*, J. of Lightwave Tech., Volume 26 , Issue 20, pp.3416-3425, Oct.15, 2008.
- [54] D. Rafique, M. Mussolin, M. Forzati, J. Martensson, M. N. Chughtai, and A. D. Ellis, *Compensation of intra-channel nonlinear fiber impairments using simplified digital back-propagation algorithm*, Optics Express, Volume 19, Issue 10, pp.9453-9460, may 2011.
- [55] L. Beygi, N. V. Irukulapati, E. Agrell, P. Johannisson, M. Karlsson, H. Wymeersch, P. Serena, and A. Bononi, *On nonlinearly-induced noise in single-channel optical links with digital backpropagation*, Opt. Express, Volume 21, Issue 22, pp.26376-26386, Nov 2013.
- [56] X. Li, X. Chen, G. Goldfarb, E. Mateo, I. Kim, F. Yaman, and G. Li, *Electronic post-compensation of WDM transmission impairments using coherent detection and digital signal processing*, Optics Express, Volume 16, Issue 2, pp. 8808-888, 2008.
- [57] A. Amari, O. A. Dobre, R. Venkatesan, O. S. Kumar, P. Ciblat and Y. Jaouën, *A survey on fiber nonlinearity compensation for 400 Gbps and beyond optical communication systems*, IEEE Commun. Surv. Tutorials, Volume 19, Issue 4, pp.3097-9113, Nov. 2017.
- [58] L. Liu, L. Li, Y. Huang, K. Cui, Q. Xiong, F. N. Hauske, C. Xie, and Y. Cai, *Intrachannel nonlinearity compensation by inverse Volterra series transfer function* J. of Lightwave Tech., Volume 30,3103-16 (2012).

- [59] V. Vgenopoulou, A. Amari, M. Song, E. Pincemin, I. Roudas, and Y. Jaouën, *Volterra-based Nonlinear Compensation in 400 Gb/s WDM Multiband Coherent Optical OFDM Systems*, Asia Communications and Photonics Conference, Nov. 2014.
- [60] V. E. Zakharov and A. B. Shabat, *Exact theory of two-dimensional self-focusing and one-dimensional self-modulation of waves in nonlinear media*, Soviet Physics-JETP, Volume 34, pp.6269, 1972.
- [61] A. Hasegawa and T. Nyu, *Eigenvalue communication*, J. of Lightwave Tech., Volume 11, Issue 3, pp.395-399, 1993.
- [62] V. E. Zakharov and Stefan Wabnitz. (eds.), *Optical Solitons: Theoretical Challenges and Industrial Perspectives*, Springer-Verlag Berlin Heidelberg (1999).
- [63] M. Nakazawa, E. Yamada, H. Kubota and K. Suzuki, *10 Gbit/s soliton data transmission over one million kilometres*, Electronics Letters, Volume 27 , Issue 14, pp. 1270-1272, 1991.
- [64] Mansoor I. Yousefi and Frank R. Kschischang, *Information Transmission using the Nonlinear Fourier Transform, Part I-III*, IEEE Trans. Inf. Theory, vol. 60 (2014).
- [65] S. T. Le, J. E. Prilepsky, and S. K. Turitsyn, *Nonlinear inverse synthesis for high spectral efficiency transmission in optical fibers*, hskip 1em plus 0.5em minus 0.4emOptics Express, Volume 22, Issue 22, pp. 26720-26741, 2014.
- [66] P. Lax, *Integrals of nonlinear equations of evolution and solitary waves*, Commun. Pure Appl. Math. 21, 467490 (1968).
- [67] M. J. Ablowitz, D. J. Kaup, A. C. Newell and H. Segur, *The Inverse Scattering Transform-Fourier Analysis for Nonlinear Problems*, Studies in Applied Mathematics 53, pp. 249-315, 1974.
- [68] M. J. Ablowitz and H. Segur, *Solitons and the Inverse Scattering Transform*, Studies in Applied Mathematics, 1981.
- [69] M. J. Ablowitz and J. F. Ladik, *Nonlinear differential-difference equations and Fourier analysis*, J. Math. Phys., Volume 17, Issue 6, pp.10111018, Jun. 1976.
- [70] G. Boffetta and A. Osborne, *Computation of the direct scattering transform for the nonlinear schroedinger equation*, J. Comput. Phys. 102, pp.252-264, 1992.

- [71] O. V. Belai, L. L. Frumin, E. V. Podivilov, and D. A. Shapiro, *Efficient numerical method of fiber bragg grating synthesis*, J. Opt. Soc. Am. B, Volume 24, Issue 7, pp.1451-1457, 2007.
- [72] A. Buryak, J. Bland-Hawthorn, and V. Steblina, *Comparison of inverse scattering algorithms for designing ultrabroadband fiber bragg gratings*, Opt. Express, Volume 17, Issue 3, pp.1995-2004, 2009.
- [73] A. Rosenthal and M. Horowitz, *Inverse scattering algorithm for reconstructing strongly reflecting fiber bragg gratings*, IEEE J. Quantum Electron., Volume 39, Issue 8, pp.1018-1026, 2003.
- [74] G. Song and S. Y. Shin, *Design of corrugated waveguide filter by the gel'fand-levitan-marchenko inverse-scattering method*, J. Opt. Soc. Am. A, Volume 2, Issue 11, pp.1985-1915, 1985.
- [75] M. I. Yousefi and X. Yangzhang, *Linear and Nonlinear Frequency-Division Multiplexing*, rXiv:1603.04389v2 [cs.IT] (2016).
- [76] S. Burtsev, R. Camassa, and I. Timofeyev, *Numerical Algorithms for the Direct Spectral Transform with Applications to Nonlinear Schrödinger Type Systems*, Journal of Computational Physics, Volume 147, Issue 1, pp.166186, 1998.
- [77] S. Wahls and H. V. Poor, *Introducing the Fast Nonlinear Fourier Transform*, IEEE International Conference on Acoustics, Speech and Signal Processing, pp. 5780 5784, May 2013.
- [78] S. Wahls and H. V. Poor, *Fast Numerical Nonlinear Fourier Transforms*, arXiv:1402.1605v3 [cs.IT] 10 Sep 2015.
- [79] S. Wahls and H. V. Poor, *Inverse Nonlinear Fourier Transforms Via Interpolation: The Ablowitz-Ladik Case*, in 21st Proc. Int. Symp. Math. Theory Networks Systems (MTNS), (Groningen, The Netherlands), pp. 18481855, July 2014.
- [80] S. Wahls and V. Vaibhav, *Fast Inverse Nonlinear Fourier Transforms for Continuous Spectra of Zakharov-Shabat Type* arXiv:1607.01305v2 [cs.IT] 5 Dec 2016.
- [81] S. Wahls, S. T. Le, J. E. Prilepsky, H. V. Poor and S. K. Turitsyn *Digital Backpropagation in the Nonlinear Fourier Domain*, IEEE 16th International Workshop on Signal Processing Advances in Wireless Communications (SPAWC) (2015).

- [82] A. Maruta and Y. Matsuda, *Polarization division multiplexed optical eigenvalue modulation*, in 2015 International Conference on Photonics in Switching (PS), pp. 256-267, Sept. 2015.
- [83] J. W. Goossens, M. I. Yousefi, Y. Jaouën, and H. Hafermann, *Polarization-division multiplexing based on the nonlinear Fourier transform*, Opt. Express 25, 26437-26452, 2017.
- [84] S. Gaiarin, M. Perego, E. P. da Silva, F. Da Ros, and D. Zibar, *Dual-polarization nonlinear Fourier transform-based optical communication system*, Optica, vol. 5, no. 3, pp. 263-270 (2018).
- [85] M. J. Ablowitz, B. Prinari, and A. D. Trubatch, *Integrable nonlinear Schrödinger systems and their soliton dynamics*, Dynamics of PDE, vol. 1, no. 3, pp. 239-299, 2004.
- [86] M. J. Ablowitz, B. Prinari, and A. D. Trubatch, *Discrete and Continuous Nonlinear Schrödinger Systems*, 1st ed., ser. Lond. Math. Soc. Lec. Note Series. Cambridge, UK: Cambridge University Press, 2003, vol. 302.
- [87] E. G. Turitsyna and S. K. Turitsyn, *Digital signal processing based on inverse scattering transform*, Opt. Lett., vol. 38, (2013).
- [88] M. J. Ablowitz, B. Prinari, and A. D. Trubatch, *Integrable nonlinear Schrödinger systems and their soliton dynamics*, Dynamics of PDE, vol. 1, no. 3, pp. 239-299, 2004.
- [89] S. L. Jansen, I. Morita, T. C. W. Schenk, D. van den Borne and H. Tanaka, *Optical OFDM-A Candidate for Future Long-Haul Optical Transmission Systems*, OFC/NFOEC 2008.
- [90] W. Shieh, and C. Athaudage, *Coherent optical orthogonal frequency division multiplexing*, Electron. Lett., Volume 42, Issue 10, pp. 5875-589, 2006.
- [91] J. Karaki, E. Pincemin, Y. Jaouen and R. L. Bidan, *Frequency Offset Estimation in a Polarization-Multiplexed Coherent OFDM system stressed by chromatic dispersion and PMD*, Conference: Lasers and Electro-Optics (CLEO), 2012.
- [92] X. Chen, and W. Shieh, *Closed-form expressions for nonlinear transmission performance of densely spaced coherent optical OFDM systems*, Opt. Express 18, 19039-19054 (2010).
- [93] S. T. Le, J. E. Prilepsky, and S. K. Turitsyn, *Nonlinear inverse synthesis for high spectral efficiency transmission in optical fibers*, Optics Express, Volume 22, Issue 22, pp. 26720-26741, 2014.

-
- [94] S. T. Le, I. D. Philips, J. E. Prilepsky, P. Harper, A. D. Ellis, S. K. Turitsyn, *First Experimental Demonstration of nonlinear inverse synthesis transmission over transoceanic distances*, J. Lighthwave Tech., Volume 34, Issue 10, pp. 2459-2466, May 2016.
- [95] S. T. Le, I. D. Philips, J. E. Prilepsky, M. Kamalian, A. D. Ellis, P. Harper and S. K. Turitsyn, *Achievable Information Rate of Nonlinear Inverse Synthesis Based 16QAM OFDM Transmission*, in Proc. ECOC, Düsseldorf, Germany, Sep. 2016.
- [96] S. T. Le and H. Buelow, *64×0.5 Gbaud Nonlinear Frequency Division Multiplexed Transmissions With High Order Modulation Formats*, J. Lighthwave Tech., Volume 35, Issue 17, pp.3692-3698, Sept. 2017.
- [97] H. Buelow, V. Aref and W. Idler, *Transmission of Waveforms Determined by 7 Eigenvalues with PSK-Modulated Spectral Amplitudes*, in Proc. ECOC, Sept. 2016.
- [98] V. Aref, S. T. Le and H. Bülöw, *Does the Cross-Talk Between Nonlinear Modes Limit the Performance of NFDM Systems*, arXiv:1801.00159v1 [eess.SP] 30 Dec 2017.
- [99] V. Aref, H. Bulow, K. Schuh, and W. Idler, *Experimental demonstration of nonlinear frequency division multiplexed transmission*, in Proc. ECOC, 2015.
- [100] T. Gui, C. Lu, A. P. T. Lau and P. K. A. Wai, *High-order modulation on a single discrete eigenvalue for optical communications based on nonlinear Fourier transform*, Optics Express, Volume 25, Issue 17, pp. 20286-20297, Aug. 2017.
- [101] S. T. Le, V. Aref, and H. Buelow, *Nonlinear signal multiplexing for communication beyond the Kerr nonlinearity limit*, Nat. Photonics, Volume 11, Issue 9, pp. 570576, July 2017.
- [102] W. A. Gemechu, M. Song, Y. Jaouën, S. Wabnitz, and M. I. Yousefi, *Comparison of the Nonlinear Frequency Division Multiplexing and OFDM in Experiment*, in Proc. ECOC, Gothenburg, Sweden, Sept. 2017, Paper W.3.C.4.
- [103] S. K. Turitsyn, J. E. Prilepsky, S. T. LE, S. Wahls, L. L. Frumin, M. Kamalian, and S. A. Derevyanko, *Nonlinear Fourier transform for optical data processing and transmission: advances and perspectives*, Optica, Volume 4, Issue 3, pp. 307322, March 2017.

- [104] V. Aref, H. Bülow, K. Schuh, and W. Idler, *Experimental demonstration of nonlinear frequency division multiplexed transmission*, in Proc. of the European Conference on Optical Communication (ECOC), 2015, paper Tu.1.1.2.
- [105] S. T. Le, V. Aref, and H. Buelow, *125 Gbps Pre-Compensated Nonlinear Frequency-Division Multiplexed Transmission*, in Proc. ECOC, Gothenburg, Sweden, Sept. 2017.
- [106] J. Armstrong, *OFDM for Optical Communications*, J. Lightwave Tech., Volume 27, Issue 3, pp.189-204, 2009.
- [107] W. Shieh and I. Djordjevic, *OFDM for Optical Communications*, Academic Press, October 2009.
- [108] R. J. Essiambre, G. Kramer, P. J. Winzer, G. J. Foschini and B. Goebel, *Capacity Limits of Optical Fiber Networks*, J. of Lightwave Techn., Volume 28, Issue 4, pp.662-701, 2010.
- [109] L. N. Binh, *Digital Optical Communications*, CRC press, 2008.
- [110] M. Seimetz, *High-Order Modulation for Optical Fiber Transmission*, Springer, 1st ed., Berlin, Germany, 2009
- [111] P. M. Becker, A. A. Olsson, and J. R. Simpson, *Erbium-doped fiber amplifiers: fundamentals and technology*, Academic press, 1999.
- [112] R. A. Linke and A. H. Gnauck, *High-capacity coherent lightwave systems*, J. Lightwave Tech., Volume 6, Issue 11, pp.1750-1769, 1988.
- [113] T. J. Schmidt, D. R. Stauffer, and K. Gass, *Implementation agreement for intradyne coherent receivers*, Optical Internetworking Forum Technical Report, April 2010.
- [114] T. M. Schmidl and D. C. Cox, *Robust frequency and timing synchronization for ofdm*, IEEE Transactions on Communications, Volume 45, Issue 12, pp.1613-1621, Dec 1997.
- [115] S. L. Jansen, I. Morita, T. C. Schenk, and H. Tanaka, *Long-haul transmission of 16×52.5 gbits/s polarization-division-multiplexed ofdm enabled by mimo processing*, J. Opt. Netw., Volume 7, Issue 2, pp.173-182, Feb 2008.
- [116] X. Yi, W. Shieh, and Y. Ma, *Phase noise effects on high spectral efficiency coherent optical ofdm transmission*, J. Lightwave Tech., Volume 26, Issue 10, pp.1309-1316, May 2008.

-
- [117] E. Pincemin, M. Song, J. Karaki, O. Zia-Chahabi, T. Guillosoy, D. Grot, G. Thouenon, C. Betoule, R. Clavier, A. Poudoulec, M. Van der Keur, Y. Jaouen, R. Le Bidan, T. Le Gall, P. Gravey, M. Morvan, B. Dumas-Feris, M. L. Moulinard, and G. Froc, *Multi-Band OFDM Transmission at 100 Gbps With Sub-Band Optical Switching*, J. Lightwave tech., Volume 32, Issue 12, JUNE 15, 2014. (Invited Paper).
 - [118] B. Slater, S. Boscolo, V. Mezentsev, and S. Turitsyn, *Comparative Analysis of BER Estimation Methods in Numerical Simulation of 40-Gb/s RZ-DPSK Transmission with In-Line SOAs*, IEEE Photonics Tech. Lett., Volume 19, Issue 8, pp.607-609, April 2007.
 - [119] R. Schmogrow, B. Nebendahl, M. Winter, A. Josten, D. Hillerkuss, S. Koenig, J. Meyer, M. Dreschmann, M. Huebner, C. Koos, J. Becker, W. Freude, and J. Leuthold, *Error vector magnitude as a performance measure for advanced modulation formats*, IEEE Photon. Tech. Lett., Volume 24, Issue 1, pp.61-63, 2012.
 - [120] I. Tavakkolnia and M. Safari, *Capacity Analysis of Signaling on the Continuous Spectrum of Nonlinear Optical Fibers*, J. Lightwave Tech., Volume 35, Issue 11, pp.2086-2097, June 2017.
 - [121] S. A. Derevyanko, J. E. Prilepsy, and S. K. Turitsyna, *Capacity estimates for optical transmission based on the nonlinear Fourier transform*, Nat. Commun., Sep. 2016.
 - [122] A. Hasegawa and Y. Kodama, *Solitons in optical communications*, 7th ed., Oxford University Press, USA, 1995.
 - [123] A. Hasegawa and Y. Kodama, *Guiding-center soliton in optical fibers*, Optics Letters, Volume 15, Issue 24, pp.1443-1445, 1990.
 - [124] S. T. Le, V. Aref, and H. Buelow, *High Speed Precompensated Nonlinear Frequency-Division Multiplexed Transmissions*, J. Lightwave Tech., Volume 36, Issue 6, pp.1296-1303, March 2018.
 - [125] C. Laperle and M. O'Sullivan, *Advances in High-Speed DACs, ADCs, and DSP for Optical Coherent Transceivers*, J. Lightwave Tech., Volume 32, Issue 4, pp. 629-643, Feb 2014.
 - [126] E. V. Sedov, A. A. Redyuk, M. P. Fedoruk, A. A. Gelash, L. L. Frumin, and S. K. Turitsyn, *Soliton content in the standard optical OFDM signal*, Optical Letters, Volume 43, Issue 24, pp. 5985-5988, Dec. 2018.
 - [127] S. Civelli, E. Forestieri, and Marco Secondini, *Why Noise and Dispersion may Seriously Hamper Nonlinear Frequency-Division Multiplexing*, Phot. Tech. Lett., Volume 29, Issue 16, pp. 1332-1335, Aug. 15 2017.

Bibliography

- [128] O. V. Belai, L. L. Frumin, E. V. Podivilov, and D. A. Shapiro, *Reconstruction of high reflectance fiber Bragg grating from noisy data*, Laser Physics, Volume 17, Issue 11, pp.1317-1322, 2007.
- [129] O. V. Belai, E. V. Podivilov, O. Y. Schwarz, D. A. Shapiro, and L. L. Frumin, *Finite Bragg grating synthesis by numerical solution of Hermitian Gel'fand-Levitan-Marchenko equations*, J. Opt. Soc. Am., Volume 24, Issue 7, pp.1451-1457, 2007.
- [130] O. V. Belai, L. L. Frumin, E. V. Podivilov, and D. A. Shapiro, *Efficient numerical method of the fiber Bragg grating synthesis*, J. Opt. Soc. Am., Volume 24, Issue 7, pp.1451-1457, 2007.
- [131] L. L. Frumin, A. A. Gelash, and S. K. Turitsyn, *New approaches to coding information using inverse scattering transform*, arXiv:1703.03153v1 [nlin.SI], 9 Mar 2017.

COMMUNICATIONS OPTIQUES BASEES SUR LA TRANSFORMEE DE FOURIER NON-LINEAIRE

RÉSUMÉ

Les performances des systèmes optiques sont limitées par les effets non-linéaires. La transformée de Fourier nonlinéaire permet d'exploiter les non-linéarités afin de dépasser la limite de Shannon nonlinéaire. La démonstration d'une transmission NFDM multiplexée en polarisation constitue une étape importante dans la mise en œuvre de ce type d'approche.

5.3 INTRODUCTION

La détection cohérente combinée à des techniques de traitement de signal permet la mise en œuvre de formats de modulation conçus dans l'hypothèse d'un canal linéaire (i.e. xQAM, OFDM). La capacité des systèmes de transmission optique approche aujourd'hui la limite de Shannon. L'accroissement des puissances injectées dans les fibres est limité par les effets non-linéaires. Les performances des égaliseurs non-linéaires, du type DBP (pour Digital Back Propagation) ou séries de Volterra sont limitées, en particulier en régime WDM par la non-prise en compte des interactions non-linéaires induites par les canaux adjacents. Une solution alternative consiste à utiliser de manière appropriée les non-linéarités : l'approche NFT (Nonlinear Fourier Transform).

Un signal NFDM (Nonlinear Frequency Division Multiplexing) consiste à multiplexer des signaux dans le domaine NFT. Le signal à transmettre est décomposé sur la base de modes spectraux non-linéaires, incluant les modes solitoniques (solutions discrètes) et les modes radiatifs dispersifs (solutions continues), qui se propagent de manière indépendante. Cette thématique de recherche commence à faire l'objet d'attention dans certains laboratoires académiques (Univ. Toronto (Canada), Univ. d'Aston (UK), DTU (Danemark), Telecom ParisTech,) et laboratoires industriels (Nokia Bell Labs (Allemagne), Huawei Labs (France)). La première partie concerne une présentation des principes de base d'une transmission NFT. Plusieurs démonstrations de transmissions à longue distance de type NFDM ont été présentées récemment. La deuxième partie concerne les premiers résultats obtenus à Télécom ParisTech avec la 1^{ère} démonstration d'une transmission NFDM multiplexée en polarisation exploitant le spectre non-linéaire continu.

5.4 PRINCIPE DUNE TRANSMISSION NFT

La propagation dun signal dans une fibre sans perte peut être modélisée par léquation de propagation non-linéaire qui décrit les interactions entre dispersion et non-linéarité de type Kerr:

$$\frac{\partial Q}{\partial \ell} = -i\frac{\beta_2}{2}\frac{\partial^2 Q}{\partial t^2} + i\gamma|Q|^2Q \quad (5.1)$$

dans laquelle $Q(t, \ell)$ représente lenveloppe du signal, β_2 le coefficient de dispersion chromatique et γ le paramètre non-linéaire. En utilisant les normalisations $q = Q/\sqrt{P_0}$, $\tau = t/T_0$ et $z = \ell/L$ avec $P_0 = 2/(\gamma L)$ et $T_0 = \sqrt{|\beta_2|L/2}$, léquation Eq.5.1 peut se mettre sous une forme normalisée:

$$i\frac{\partial q}{\partial z} = \frac{\partial^2 q}{\partial \tau^2} + 2s|q|^2q \quad (5.2)$$

où $s = \pm 1$, fonction du signe de la dispersion chromatique D (i.e. $s = 1$ pour une fibre à dispersion positive (í focusing régime) et $s = -1$ pour une fibre à dispersion négative (í defocused regime ž).

Zakharov and Shabat ont démontré que Eq.5.2 est un système non-linéaire intégrable. Les solutions peuvent être calculées, par exemple, par la méthode de í diffusion inverse ž. Le signal peut être décomposé en une combinaison de composantes spectrales non-linéaires λ qui évoluent linéairement avec la propagation dans la fibre. Ainsi, de manière similaires aux systèmes de communications classiques (i.e. hypothèse régime linéaire), il est possible détablir une relation linéaire entrée-sortie des composantes spectrales non-linéaires:

$$\text{NFT}(q(L, \tau)) = e^{-4is\lambda^2 L} \text{NFT}(q(0, \tau)) \quad (5.3)$$

Différentes méthodes numériques du calcul des signaux $\widehat{q}(0, \lambda)$ sont décrites dans

5.5 TRANSMISSION DUN SIGNAL NFDM MULTIPLEXE EN POLARISATION

Le dispositif expérimental dune transmission NFDM est présenté sur la Fig.5.1. Un système NFDM présente un certain nombre de similitudes à celles dun système OFDM. Les étapes du traitement de signal sont insérées sur la figure, les blocs en blanc correspondent au cas OFDM, les blocs de couleur aux étapes additionnelles nécessaires au cas NFDM.

5.5. TRANSMISSION DUN SIGNAL NFDM MULTIPLEXE EN POLARISATION

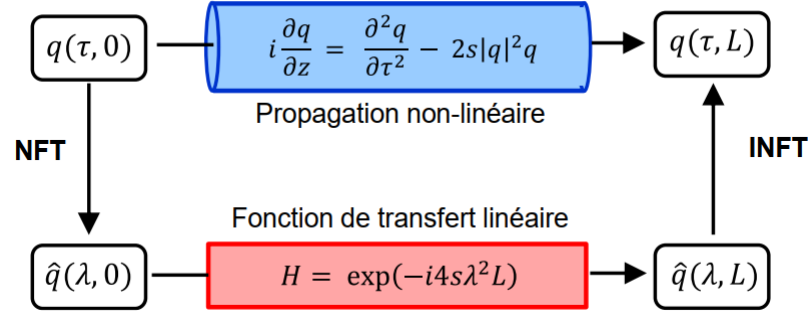


Figure 5.1: Comparaison dune transmission NFDM et linéaire.

Un signal NFDM est constitué dun multiple de sous-porteuses, chacune portant une séquence de symboles c_k de type QAM:

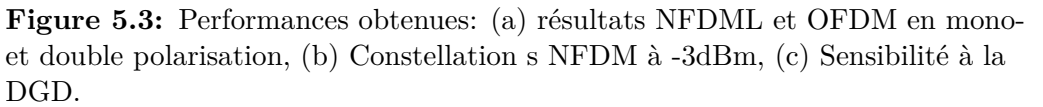
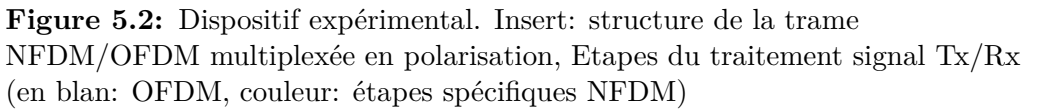
$$U(0, \lambda) = \sum_{k=1}^{N_{sc}} c_k \sigma(\lambda - kW_0) \quad (5.4)$$

où N_{sc} et W_0 représentent le nombre et l'espacement des sous-porteuses, et $\sigma(x)$ est la fonction Dirac. Le signal transmis dans le domaine temporel s'écrit $q(0\tau) = TF^{-1}[U(0, \lambda)]$. Afin de saffranchir des interactions entre symboles successifs, une bande de garde temporelle de $1.5T_0$ est introduite des deux côtés de chaque symbole de durée T_0 , soit le symbole résultant $q(0, \tau)$. En posant $U(0, \lambda) = TF[q(0, \tau)]$, le signal dans le domaine spectral s'écrit finalement:

$$\tilde{q}(0, \lambda) = \sqrt{1 - e^{-|U'(0, \lambda)|^2}} e^{i \arg U'(0, \lambda)} \quad (5.5)$$

Le signal NFDM/OFDM est consisté de matrices de 32 sous-porteuses \times 64 symboles 16QAM. Les 8 premiers symboles sont utilisés en tant que séquence d'apprentissage et 2 sous-porteuses par symbole sont allouées à l'estimation de la phase commune. Les signaux optiques sont générés au moyen dun AWG (64GS/s) couplé à un modulateur I&Q. Le signal NFDM multiplexé en polarisation $\mathbf{q} = (q_1, q_2)^T$ nécessite le calcul des composantes q_1 et q_2 considérant une équation de propagation de type Manakov. Le signal multiplexé est émulé au moyen dun PDME : génération successive des signaux q_1 et q_2 et réaligement via une ligne à retard optique. Le signal transmis correspond à un débit binaire en mode burst de 128 Gb/s (pas de prise en compte des intervalles de garde). Le signal est transmis dans une boucle à recirculation constituée de 2 tronçons de fibres sous-marines de 70 km ($D = -4.66$ ps/nm/km).

Les performances obtenues sont présentées sur la Fig.5.3(a) en mono- et double polarisation. Des performances similaires à l'optimum de puissance sont



CONCLUSION

La transmission d'un signal NFDM multiplexé en polarisation utilisant le spectre non-linéaire continu a été démontrée expérimentalement. Un gain du facteur Q de 0.25 dB du format NFDM par rapport au cas OFDM a été observé. La sensibilité à la DGD est compatible avec les niveaux de PMD des fibres actuellement déployées.



Titre : Comparison of Nonlinear Frequency Division Multiplexing and OFDM for optical fiber transmissions

Mots clés : transformée de Fourier nonlinéaire (NFT), multiplexage non linéaire en fréquence (NFTM), multiplexés par division de polarisation (PMD)

Résumé : La capacité ultime du canal dans les systèmes de transmission optique à longue distance est limitée par les effets non linéaires liés à la propagation dans les fibres optiques. Des techniques de compensation des effets non-linéaires, tel que la DBP (Digital Back Propagation), ont été proposées pour surmonter ces limitations et accroître la capacité. Compte tenu de leur complexité d'implémentation, leur gain en performance reste très limité. Cela a déclenché très récemment la recherche de nouvelles techniques de communication prenant en compte la non-linéarité de la fibre. Une nouvelle méthode de communication en régime non-linéaire, basée sur la théorie de la transformation spectrale inverse (IST pour Inverse Spectral Transform), a été proposée pour surmonter la limitation induite par ces effets. Cette méthode, proposée à l'origine par Hasegawa en 1993, encore appelée communication aux valeurs propres (ou multi-solitons), est basée sur l'observation fondamentale selon laquelle le spectre non linéaire d'un signal optique est invariant (à l'exception d'un déphasage linéaire trivial) lors de la propagation dans la fibre optique, comme décrit par l'équation non linéaire de Schrödinger (NLSE pour Non-Linear Schrödinger Equation). Cela signifie que si la transformée spectrale directe (DST) (également appelée NFT pour Nonlinear Fourier Transform) du signal reçu peut être calculée, le spectre de valeurs propres peut être entièrement récupéré.

La capacité ultime du canal dans les systèmes de transmission optique à longue distance est limitée par les effets non linéaires liés à la propagation dans les fibres optiques. Des techniques de compensation des effets non-linéaires, tel que la DBP (Digital Back Propagation), ont été proposées pour surmonter ces limitations et accroître la capacité. Compte tenu de leur complexité d'implémentation, leur gain en performance reste très limité. Cela a déclenché très récemment la recherche de nouvelles techniques de communication prenant en compte la non-linéarité de la fibre. Une nouvelle méthode de communication en régime non-linéaire, basée sur la théorie de la transformation spectrale inverse (IST pour Inverse Spectral Transform), a été proposée pour surmonter la limitation induite par ces effets. Cette méthode, proposée à l'origine par Hasegawa en 1993, encore appelée communication aux valeurs propres (ou multi-solitons), est basée sur l'observation fondamentale selon laquelle le spectre non linéaire d'un signal optique est invariant (à l'exception d'un déphasage linéaire trivial) lors de la propagation dans la fibre optique, comme décrit par l'équation non linéaire de Schrödinger (NLSE pour Non-Linear Schrödinger Equation). Cela signifie que si la transformée spectrale directe (DST) (également appelée NFT pour Nonlinear Fourier Transform) du signal reçu peut être calculée, le spectre de valeurs propres peut être entièrement récupéré.



Title : Comparison of Nonlinear Frequency Division Multiplexing and OFDM for optical fiber transmissions

Keywords : Nonlinear Fourier transform (NFT), nonlinear frequency division multiplexing (NFDM), polarization division multiplexing (PDM)

Abstract : Nonlinear effects in optical fiber set the ultimate limit to the channel capacity in long-haul optical transmission systems. Advanced nonlinear compensation techniques such as digital back propagation (DBP) have been proposed as a solution to overcome the channel capacity crunch. However, given their computational complexity, in a practical environment their performance gain remains very limited. This triggered a search for a novel communication system design that takes fiber nonlinearity into consideration. A new nonlinear communication method, based on the theory of the inverse spectral transform, has been proposed to overcome the nonlinear capacity crunch. This method, originally proposed by Hasegawa in 1993 and called eigenvalue (or multi-soliton) communication, is based on the fundamental observation that the nonlinear spectrum of an optical signal is invariant (except for a trivial linear phase shift) upon propagation in the fiber channel, as described by the nonlinear Schrödinger equation (NLSE). This means that if the direct spectral transform (DST) (also known as nonlinear Fourier transform (NFT)) of the received signal can be computed, the eigenvalue spectrum can be fully recovered.

Nonlinear effects in optical fiber set the ultimate limit to the channel capacity in long-haul optical transmission systems. Advanced nonlinear compensation techniques such as digital back propagation (DBP) have been proposed as a solution to overcome the channel capacity crunch. However, given their computational complexity, in a practical environment their performance gain remains very limited. This triggered a search for a novel communication system design that takes fiber nonlinearity into consideration. A new nonlinear communication method, based on the theory of the inverse spectral transform, has been proposed to overcome the nonlinear capacity crunch. This method, originally proposed by Hasegawa in 1993 and called eigenvalue (or multi-soliton) communication, is based on the fundamental observation that the nonlinear spectrum of an optical signal is invariant (except for a trivial linear phase shift) upon propagation in the fiber channel, as described by the nonlinear Schrödinger equation (NLSE). This means that if the direct spectral transform (DST) (also known as nonlinear Fourier transform (NFT)) of the received signal can be computed, the eigenvalue spectrum can be fully recovered.

